DEVELOPMENT OF GRAPHENE OXIDE BASED AEROGELS FOR ENVIRONMENTAL APPLICATIONS

A THESIS SUBMITTED TO
THE GRADUATE SCHOOL OF NATURAL AND APPLIED SCIENCES
OF
MIDDLE EAST TECHNICAL UNIVERSITY

BY

DUYGU SEZEN POLAT

IN PARTIAL FULFILLMENT OF THE REQUIREMENTS
FOR
THE DEGREE OF MASTER OF SCIENCE
IN
CHEMICAL ENGINEERING

SEPTEMBER 2020

Approval of the thesis:

DEVELOPMENT OF GRAPHENE OXIDE BASED AEROGELS FOR ENVIRONMENTAL APPLICATIONS

submitted by **DUYGU SEZEN POLAT** in partial fulfillment of the requirements for the degree of **Master of Science** i**n Chemical Engineering, Middle East Technical University** by,

Prof. Dr. Halil Kalıpçılar
Dean, Graduate School of **Natural and Applied Sciences** _____

Prof. Dr. Pınar Çalık
Head of the Department, **Chemical Engineering** _____

Assoc. Prof. Dr. Erhan Bat
Supervisor, **Chemical Engineering, METU** _____

Examining Committee Members:

Prof. Dr. Bora Mavis
Mechanical Engineering, Hacettepe University _____

Assoc. Prof. Dr. Erhan Bat
Chemical Engineering, METU _____

Assoc. Prof. Dr. Zeynep Çulfaz Emecen
Chemical Engineering, METU _____

Assist. Prof. Dr. Emre Büküşoğlu
Chemical Engineering, METU _____

Assist. Prof. Dr. Bahar İpek Torun
Chemical Engineering, METU _____

Date: 23.09.2020

I hereby declare that all information in this document has been obtained and presented in accordance with academic rules and ethical conduct. I also declare that, as required by these rules and conduct, I have fully cited and referenced all material and results that are not original to this work.

Name, Last name : Duygu Sezen Polat

Signature :

ABSTRACT

DEVELOPMENT OF GRAPHENE OXIDE BASED AEROGELS FOR ENVIRONMENTAL APPLICATIONS

Polat, Duygu Sezen
Master of Science, Chemical Engineering
Supervisor: Assoc. Prof. Dr. Erhan Bat

September 2020, 96 pages

In order to cope with increasing water pollution due to crude oils, petroleum products, organic solvents, and dyes, it is urgent to come up with feasible and economical solutions. Due to their large surface area, abundant functional groups and tunable properties, graphene oxide (GO) based aerogels are promising candidates for pollutant removal. In the scope of this thesis study, it was aimed to produce GO-based aerogels with high reusability performance and removal capacity to be used in environmental applications. GO was synthesized by the Tour method and characterized with ATR-FTIR, TGA and UV-vis. GO aerogels, reduced GO-stearic acid-based (rGO/SA) aerogels and GO-(3-Aminopropyl)triethoxysilane aerogels (GO-NH_2) were prepared. Analysis of the porous structures of produced aerogels was conducted by using SEM. ATR-FTIR analysis was performed for the chemical characterization of the aerogels, and TGA was performed to evaluate their thermal properties. The pollutant removal performance of aerogels was compared using chloroform, sunflower, methylene blue (MB) and methyl orange (MO). rGO aerogels exhibited an absorption capacity of 155 g/g for chloroform while rGO/SA aerogels exhibited 87 g/g. However, rGO/SA aerogel maintained its original

absorption capacity even after 15 cycles, unlike rGO aerogels, which exhibited a sharp decrease after the 1st cycle.

Meanwhile, the parameters affecting the adsorption capacity of GO and GO-NH_2 aerogels toward dyes, such as initial concentration and pH, contact time, temperature and dye charge, were investigated. Adsorption kinetics and isotherms were also examined for MB and MO. GO and GO-NH_2 were found to have maximum adsorption capacities of 588 mg/g and 118 mg/g for MB and MO, respectively, as calculated from the Langmuir isotherm. The kinetic study revealed that adsorption of MB on GO aerogels followed the pseudo-first-order model while the adsorption of MO followed the modified Freundlich model. Van't Hoff equation used to calculate thermodynamic parameters indicated that the adsorption process of MB onto GO aerogels was endothermic and spontaneous. Recyclability and reusability studies on GO aerogels for MB adsorption were also conducted. Aerogels could easily be recycled and reused, and they were able to maintain over 90% removal capacity after ten cycles.

Keywords: Graphene oxide, aerogel, adsorption, absorption, separation

ÖZ

ÇEVRE UYGULAMALARI İÇİN GRAFEN OKSİT ESASLI AEROJELLERİN GELİŞTİRİLMESİ

Polat, Duygu Sezen
Yüksek Lisans, Kimya Mühendisliği
Tez Yöneticisi: Doç. Dr. Erhan Bat

Eylül 2020, 96 sayfa

Ham petrol, petrol ürünleri, organik çözücülerden ve boyalardan kaynaklı artan su kirliliği ile baş edebilmek için uygulanabilir ve ekonomik çözümler bulunması gerekmektedir. Geniş yüzey alanları, bol fonksiyonel grupları ve değiştirilebilir özellikleri sayesinde grafen oksit (GO) bazlı aerojeller su kirliliklerini giderme çalışmaları için gelecek vaat etmektedir. Bu tez su arıtımına yönelik yüksek tekrar kullanılabilirlik ve arındırma performansı olan GO-esaslı aerojellerin üretilmesi ve arındırma mekanizmalarının araştırılması amaçlanmıştır. GO, Tour metotu kullanılarak sentezlenmiş ve ATR-FTIR, TGA ve UV-vis ile karakterizasyonları yapılmıştır. GO aerojeller, indirgenmiş GO-stearik asit (rGO/SA) aerojeller ve GO-(3-Aminopropil)trietoksisilan (GO-NH_2) aerojeller üretilmiştir. Üretilen aerojellerin gözenekli yapıları SEM ile analiz edilmiştir. Kimyasal karakterizasyonları ATR-FTIR ve ısıl özellikleri TGA kullanılarak değerlendirilmiştir. Aerojellerin arındırma performansları kloroforom, ayçiçek yağı, metilen mavisi (MB) ve metil turuncusu (MO) kullanılarak ölçülmüştür. rGO aerojel kloroform için 155 g/g soğurma kapasitesi gösterirken, rGO/SA aerojeller maksimum 87 g/g soğurma kapasitesine ulaşabilmiştir. Fakat rGO/SA aerojeller ikinci tekrar kullanımdan sonra soğurma kapasitesinde ani düşüş yaşayan rGO aerojellerinin aksine on tekrar kullanımdan sonra da ilk soğurma kapasitesini koruyabilmiştir. Ayrıca, başlangıç derişimi ve pH

değeri, temas zamanı, sıcaklık ve boya yükü gibi GO and GO-NH_2 aerojellerinin yüzeye tutunma kapasitelerini etkileyen parametreler araştırılmıştır. MB ve MO için kinetik ve izotermler incelenmiştir. GO ve GO-NH_2 aerojellerinin MB ve MO için maksimum yüzeye tutunma kapasiteleri Langmuir izotermi kullanılarak sırasıyla 588 mg/g ve 118 mg/g olarak hesaplanmıştır. Kinetik çalışmaları GO aerojellerin MB için yüzeye tutunmasının yalancı birinci dereceden modeli takip ederken, MO için değiştirilmiş Freundlich modeli takip ettiğini göstermiştir. Termodinamik parametreleri van't Hoff denklemi kullanılarak hesaplanmış ve MB yüzeye tutunma sürecinin endotermik ve kendiliğinden gerçekleştiği anlaşılmıştır. GO aerojellerin MB yüzeye tutunması için geri dönüştürme ve tekrar kullanılma çalışmaları yapılmıştır. Son olarak GO aerojel kolay bir şekilde geri dönüştürebilmiş ve on döngüden sonra da %90'dan fazla ayırma performansını koruyarak tekrar kullanılabilirmiştir.

Anahtar Kelimeler: Grafen oksit, aerojel, yüzeye tutunma, soğurma, ayırma

To my family,

ACKNOWLEDGMENTS

I would like to express my sincere appreciation and gratitude to my supervisor, Dr. Erhan Bat, for his support in all aspects during my graduate career, interest and great supervision. He guided and helped me with his knowledge of my thesis. It has been a great experience for me to be a part of his research group.

I would like to thank Dr. Gülay Ertaş, Dr. Harun Koku and Dr. Yasemin Dilşad Yılmazel Tokel for their understanding and for letting me use their laboratory equipment.

I would like to express my appreciation to İsa Çağlar, Mihrican Açıkgöz and Doğan Akkuş for their help and kindness.

I especially thank my labmate and officemate Öznur Doğan for all her support and friendship in my academic and social life since my undergraduate education. I feel fortunate to have a chance to work with her.

I would like to thank my former lab partners; Ayşe Elif Kıratlı, Zeynep Cansu Özçınar, Barış Can and Beril Üstünkaya for their help and friendship. I would also like to thank my "Yemekhane" companions Begüm Yılmaz, Betül Oflaz, Candan Karaeyvaz, Ezgi Altıntaş, Ezgi Gözde, Fırat Taşkın, Gökhan Gök and Salih Ermiş for their frienship and the cheers that they gave me.

I appreciate the invaluable friendships of Dilay Oruç, Esra Karaşin and Nazlı Okuyucu. I have always felt special with the intimacy and support they provided. I am also grateful to my dearest friends Ayşenur Aksoy and Rabia Turacak, who were always supportive and making me laugh whatever happens in life. Special thanks to Cansu Balku and Merve Çobanoğlu, everything would be much harder without their support and friendship.

Last but not least, I would like to dedicate this work to my parents Ayşe and Erdal, for the most meaningful support. I am always sure that they are my best supporters and

always on my side, whatever my decision is. Many thanks to my sister and best friend Gülsinem, who has always been an inspiration for me and my brother Steffen, who always gave me great pieces of advice. Finally, special thanks to my cat Mıncık for never supporting me nor helping me.

TABLE OF CONTENTS

ABSTRACT v

ÖZ vii

ACKNOWLEDGMENTS x

TABLE OF CONTENTS xii

LIST OF TABLES xv

TABLES xv

LIST OF FIGURES xvi

FIGURES xvi

LIST OF ABBREVIATIONS xx

LIST OF SYMBOLS xxii

CHAPTERS

1 INTRODUCTION 1

2 BACKGROUND AND LITERATURE REVIEW 5

2.1 Graphene Oxide 5

2.1.1 Structure and Properties of Graphene Oxide 6

2.1.2 Synthesis of Graphene Oxide 7

2.2 Aerogels 9

2.3 Graphene Oxide Based Aerogels 11

2.3.1 Synthesis of Graphene Oxide Based Aerogels 12

2.3.2 Graphene Oxide Based Aerogels for Pollutant Removal 16

3 MATERIALS AND METHODS 33
3.1 Materials 33
3.2 Methods 33
3.2.1 Synthesis of Graphene Oxide 33
3.2.2 Production of Reduced Graphene Oxide and Stearic Acid Based Aerogels 34
3.2.3 Production of Graphene Oxide and (3-Aminopropyl) triethoxysilane Based Aerogels 35
3.2.4 Oil Absorption Experiments 36
3.2.5 Dye Adsorption Experiments 36
3.2.6 Aerogel Regeneration 39
3.3 Characterizations 40
3.3.1 Thermogravimetric Analysis (TGA) 40
3.3.2 Scanning Electron Microscopy (SEM) 40
3.3.3 Attenuated Total Reflectance-Fourier Transform Infrared Spectroscopy (ATR-FTIR) 40
3.3.4 Ultraviolet-visible Spectroscopy (UV-Vis) 40
4 RESULTS AND DISCUSSION 41
4.1 Graphene Oxide Synthesis 41
4.2 Reduced Graphene Oxide Based Aerogels 46
4.2.1 Absorption Performance of Reduced Graphene Oxide Based Aerogels 48
4.2.2 Structure Analysis of Reduced Graphene Oxide and Stearic Acid Based Aerogels 50
4.3 Graphene Oxide Based Aerogels 52

4.3.1 Adsorption Performance of Graphene Oxide Based Aerogels toward Dyestuff 53
5 CONCLUSION 69
6 OUTLOOK 71
REFERENCES 73
A. TGA Thermograms 89
B. Dye Adsorption Experiment Results 92
C. Standard Calibration Curve 95
D. Preliminary Absorption Experiments 96

LIST OF TABLES

TABLES

Table 2.1 Summary of the methods used to prepare to GO 8
Table 2.2 Classification of aerogels[57] and examples from the literature on their existing applications..... 11
Table 2.3 The adsorption performance of GO-based aerogels for dyes..... 25
Table 3.1 Physical properties of chemicals used in experiments..... 33
Table 4.1 ATR-FTIR peak positions (in cm^{-1}) of GO from literature and experimental data..... 43
Table 4.2 Intraparticle diffusion parameters for the adsorption of MB and MO ... 58
Table 4.3 Adsorption isotherm parameters for MB by GO Aerogel..... 63
Table 4.4 Thermodynamic parameters of MB adsorption by GO Aerogel..... 63
Table 4.5 Comparison of various aerogels for MB adsorption..... 65
Table 4.6 Adsorption isotherm parameters for MO by GO and GO-NH_2 68
Table B. 1 Kinetic study experimental results for MB adsorption..... 92
Table B. 2 Isotherm study experimental results for MO adsorption..... 92
Table B. 3 Isotherm study experimental results for MB adsorption 93
Table C. 1 Calibration curve fitting parameters for MB and MO..... 95

LIST OF FIGURES

FIGURES

Figure 2.1 Schematic representations of graphene family materials[13] 5
Figure 2.2 Proposed models for GO structure[38] 7
Figure 2.3 General preparation route to prepare aerogels[57] 10
Figure 2.4 Environmental applications and removal mechanisms for different pollutants[71] 12
Figure 2.5 (a) Products after hydrothermal reduction at 180 °C for 12 h (b) Products after hydrothermal reduction of 2 mg/mL GO aqueous dispersion at 180 °C for different durations[80] 13
Figure 2.6 (a) GO dispersion, (b) graphene hydrogel after L-ascorbic acid reduction, (c) graphene aerogels prepared via (left) supercritical CO_2 and (right) freeze-drying, (d) 7.1 mg graphene aerogel supporting more than 14000 times its weight[82] 14
Figure 2.7 (a) GO before (1) and after hydrothermal reduction (2). rGO mixed with Ca^{2+} (3) and rGO cylinders assembled by Ca^{2+} with various Ca to GO weight ratios (4,5,6,7). (b) rGO cylinders assembled by (8) Ni^{2+} and (9) Co^{2+} (c) Ca2+ linked rGO samples dried by (10) natural evaporation and freeze-drying (11) without and (12) with PVA strengthening[83] 15
Figure 2.8 (a) Photographs of MB solution before and after adsorption. (b) The UV spectrum of MB solution at different contact times. (c) Photographs of fast-compressible test for MB-water separation[104] 21
Figure 2.9 (Left) Photographs of MB before and after adsorption (Right) Adsorption-desorption cycles of MB dye adsorbed cl-CS-p(MA/GO-Fe_3O_4) NPs[106] 22
Figure 2.10 Removal performance of mimGO aerogel and adsorption mechanism for DR80[110] 24
Figure 2.11 Photographs of the diesel-water system before and after continuous adsorption[121] 27

Figure 2.12 EDA-ammonia reduction of GO (left) and SEM image of the aerogel (right)[63] 27
Figure 2.13 Photographs of methyl-red dyed chloroform adsorption from the water with DAP/rGO aerogel (top), absorption capacities of aerogels for chloroform (bottom)[69] 28
Figure 2.14 Absorption performance of aerogels towards various organic chemicals[11] 29
Figure 2.15 Photographs of an LGA during the compressive and recovery process (left), Absorption capacities of aerogels for different oils and organic solvents (right)[123] 30
Figure 2.16 Removal performance of the aerogels for organic solvents and oils[125] 31
Figure 3.1 Schematic representation of GO synthesis from graphite 34
Figure 3.2 Schematic representation of GO and SA reaction to produce aerogels and the proposed reaction mechanism 35
Figure 3.3 Chemical Structure Depiction of MB 37
Figure 3.4 Chemical Structure Depiction of MO 37
Figure 4.1 Photographs showing the changes of the reaction mixture during the GO synthesis (initial reaction mixture (a), after 12 h (b), after ice and H_2O_2 addition (c)) 42
Figure 4.2 ATR-FTIR Analysis of Graphite and GO 43
Figure 4.3 TGA Results of Graphite and GO 44
Figure 4.4 UV-vis Analysis Result of GO 45
Figure 4.5 SEM image of GO 46
Figure 4.6 ATR-FTIR Analysis of rGO/SA aerogels 47
Figure 4.7 TGA Results of rGO/SA aerogels and pure SA 48
Figure 4.8 Absorption capacities of rGO and rGO/SA aerogels 49
Figure 4.9 Recyclability of rGO and rGO/SA aerogels for chloroform absorption 50

Figure 4.10 SEM images of rGO/SA aerogels, SG20 (a,b), SG50 (c,d) and SG60 (e,f) 51
Figure 4.11 FTIR spectra of GO and GO-NH_2 aerogels 52
Figure 4.12 Change of adsorbed amount (Q_t, mg/g) of MB and removal efficiency (R%) with increasing adsorption time at 298 K and pH=7.8. Data represent mean ± SD (*n* = 3) 54
Figure 4.13 Change of adsorbed amount (Qt, mg/g) of MO and removal efficiency (R%) with increasing adsorption time at 298 K and pH=7.8. Data represent mean ± SD (*n* = 3) 55
Figure 4.14 The pseudo-first-order model for batch adsorptions of MB and MO at 298 K and pH=7.8 56
Figure 4.15 The pseudo-second-order model for batch adsorptions of MB and MO at 298 K and pH=7.8 56
Figure 4.16 The Modified Freundlich model for batch adsorptions of MB and MO at 298 K and pH=7.8 57
Figure 4.17 The intra-particle model for batch adsorptions of MB and MO at 298 K and pH=7.8 58
Figure 4.18 Effect of initial pH on MB and MO adsorption at 298 K. Data represent mean ± SD (*n* = 3) 59
Figure 4.19 Effect of MB concentration and temperature at pH=7.8. Data represent mean ± SD (*n* = 3) 61
Figure 4.20 Langmuir isothermal adsorption models at pH=7.8 62
Figure 4.21 Freundlich isothermal adsorption models at pH=7.8 62
Figure 4.22 Recyclability of GO aerogel for MB adsorption at 298 K, pH=7.8 and initial dye concentration of 100 ppm. Data represent mean ± SD (*n* = 3) 64
Figure 4.23 Adsorption isotherm of MO at 298 K and pH=7.8 Data represent mean ± SD (*n* = 3) 66
Figure 4.24 Langmuir adsorption isotherm of MO at 298 K and pH=7.8 67
Figure 4.25 Freundlich adsorption isotherm of MO at 298 K and pH=7.8 67

Figure A. 1 TGA thermogram of graphite 89
Figure A. 2 TGA thermogram of GO..... 90
Figure A. 3 TGA thermogram of rGO aerogel 90
Figure A. 4. TGA thermogram of rGO/SA aerogel 91
Figure B. 1 UV-Vis spectra of the MB (a) and MO (b) solutions after being adsorbed by GO aerogel..... 94
Figure C. 1 Calibration curve for MB and MO 95
Figure D. 1 Effect of gel formation temperature and thermal reduction on chloroform absorption capacities of GO-based aerogels 96

LIST OF ABBREVIATIONS

Abbreviation	Definition
1,3-DAP	1,3-diaminopropane
APTES	(3-Aminopropyl) triethoxysilane
CdS	Cadmium sulfide
CdSe	Cadmium selenide
CNT	Carbon nanotube
CS	Chitosan
DMF	N, N-dimethylformamide
EDA	Ethylenediamine
EPA	Environmental Protection Agency
Fe_3O_4	Iron (II, III) oxide
GA-NH_2	Graphene oxide-APTES based aerogel
GO	Graphene oxide
H_2O_2	Hydrogen peroxide
HCl	Hydrochloric acid
H_2SO_4	Sulfuric acid
H_3PO_4	Orthophosphoric acid
HI	Hydriodic acid
HNO_3	Nitric acid
$KClO_3$	Potassium chlorate
K_2FeO_4	Potassium ferrate
$KMnO_4$	Potassium permanganate
LGA	Lignin modified graphene aerogel
$LiAlH_4$	Lithium tetrahydro aluminate
MB	Methylene blue

Abbreviation	Definition
$NaBH_4$	Sodium borohydride
NbC	Niobium carbide
OG	Orange G
PbS	Lead (II) sulfide
PEI	Polyethyleneimine
PVA	Poly (vinyl alcohol)
RD80	Direct Red 80
RF	Resorcinol-formaldehyde
rGO	Reduced graphene oxide
RhB	Rhodamine B
SiO_2	Silicon dioxide
SnO_2	Tin (IV) oxide
TiO_2	Titanium dioxide
WHO	World Health Organization
ZnO	Zinc oxide
ZnS	Zinc sulfide

LIST OF SYMBOLS

Symbol	Definition
ΔG^0	Gibbs free energy change
ΔH^0	Enthalpy change
ΔS^0	Entropy change
C_0	Initial concentration
C_e	Equilibrium concentration
C_t	Concentration at time t
k_1	The rate constant of pseudo-first-order adsorption
k_2	The rate constant of pseudo-second-order adsorption
K_0	Thermodynamic equilibrium constant
K_F	Freundlich adsorption constant
K_L	Langmuir adsorption constant
m	Dry aerogel mass
m_e	Swollen aerogel mass at equilibrium
n	Freundlich constant for adsorption intensity
Q_e	Equilibrium amount of solute adsorbed per gram of adsorbent
Q_m	The theoretical maximum amount of solute adsorbed
Q_t	Amount of solute adsorbed per gram of adsorbent at time t
R	Removal efficiency
R_L	Dimensionless separation factor
V	Solution volume
v_e	The activity coefficient of the adsorbate
v_s	The activity coefficient of the adsorbate in solution

CHAPTER 1

INTRODUCTION

Expeditious growth in industrial activities resulted in an alarming increase in planet exploitation over the past few decades. These industrial activities lead to the release of toxic chemicals into the air, water, and land; hence, contaminate them. Toxic chemical concentrations in water bodies worldwide are much higher than the designated restrictions set by World Health Organization (WHO) and Environmental Protection Agency (EPA)[1]. The release of these chemicals poses fatal risks to living organisms and the aforementioned components of nature. Therefore, water pollution has become a global environmental concern that requires feasible and practical solutions. Among other pollutants, oils, organic compounds and dyes are the significant sources of water pollution[2].

Dyes are widespread water pollutants and are frequently used in various industries, including textile, plastic, food and printing. As a result of their elaborate molecular structures, most of the dyes are stable. They do not biodegrade quickly, and due to their polar functional groups, they are dispersible in water and able to spread into the environment quickly. Synthetic dyes, which are usually carcinogenic and mutagenic, are stable to temperature, light, and even microbial attacks[3]. The majority of the effluents containing dyes are directly discharged into river streams. Dyes significantly affect aquatic life and the food chain even in very low concentrations[4]. Dyes hinder marine flora's photosynthetic activities by decreasing light penetration in rivers and cut down their food resources. Moreover, the accumulation of discharged dyes on the river surfaces reduces the oxygen concentration and harms the aquatic fauna as well[5].

In recent decades several oil spill accidents occurred due to the extraction, storage, or transportation of oil. The majority of oil spill accidents occur during transportation with oil tankers. In 2010, a massive oil spill occurred in the Gulf of Mexico, in which almost 4.9 million barrels of oil spilled. This accident affected marine species and seagrasses irreversibly. Over 15% of 322 species were threatened, and 8% of them were nearly threatened[6]. In 2014, 3000 barrels of oil spilled in the Sundarbans nature reserve, which covered the shoreline, damaged the trees and killed many animals due to the toxic chemicals[6]. Oil spills cause various environmental impacts, including the destruction of flora, fauna, natural habitats and ecological imbalances.

There have been many strategies proposed to adsorb and mitigate pollutants. These methods can be examined in three groups: physical methods such as membrane-filtration and sorption processes; chemical methods such as coagulation, irradiation, and electrochemical processes; and biological methods such as aerobic and anaerobic microbial degradation[5]. Of these proposed technologies, sorption processes and adsorption, in particular, has several advantages, such as simple operation, low cost, efficiency, availability, and flexibility. Hence, the search for efficient yet straightforward, environmentally friendly adsorbents has become the main focus of adsorption studies.

For dye adsorption, activated carbon is regarded as a useful but expensive adsorbent due to its manufacturing and regeneration costs. Therefore, numerous alternatives have been proposed for the adsorption of such as[3,5] alumina, agricultural, industrial, domestic waste by-products, chalcogenides, chitin, and coal (high silica content), silica, and zeolites. Among them, graphene and its derivatives like graphene oxide (GO) play an essential role due to their large surface area (2630 m^2/g) and excellent physical and chemical properties. Different from its graphene counterpart, GO possesses several distinct properties. First of all, it is dispersible and processable in water and various organic solvents[7,8]. Moreover, it can gain versatile features as a result of their functional groups. Finally, it can be synthesized from graphite with a high yield and cost-effective method. GO, as a highly oxidized form of graphene, has epoxy and hydroxyl groups on the basal plane and carboxylic group at the edges[9].

As a result, GO platelets are negatively charged in the aqueous solution, promoting the adsorption of cationic dyes through electrostatic interaction. Moreover, due to GO's carbon atoms, which are present in the sp^2 hybridization state, GO can also exhibit π-π interactions with dyes with aromatic structures. Finally, GO can also display hydrogen bonding interaction with dyes containing amino or hydroxy groups. GO-based materials have shown remarkable performances in oil removal also. While the traditional porous sorbents used for oil spill clean-ups have low absorption capacities (less than ten times of their weight), GO-based sorbents can absorb oil up to 600 times their weight[10,11]. In addition to their high surface area, by partially reducing their oxygen-containing groups, hydrophobic and oleophilic sp^2 domains of GO-based materials can be re-established. GO-based aerogels, in particular, have even more significant potential in water treatment applications due to their loose and porous structure, which can facilitate the diffusion of dye, oil and organic solvent molecules.

This study aims to develop novel and useful methods to produce GO-based aerogels for pollutant removal with enhanced sorption capacity and reusability. The pollutant removal performance of the aerogels was investigated for oil absorption and dye adsorption. For oil absorption, thermal reduction and stearic acid incorporation to the structure were performed to re-establish the GO-based aerogel's hydrophilic and oleophilic sp2 domains. For dye adsorption, bare GO aerogels were prepared to achieve enhanced adsorption capacity for cationic dyes due to its abundant functional groups. (3-Aminopropyl)triethoxysilane (APTES) deposition was employed to increase the adsorption capacity of GO-based aerogel toward anionic dyes.

CHAPTER 2

BACKGROUND AND LITERATURE REVIEW

2.1 Graphene Oxide

Graphene and its derivatives such as graphite, GO, carbon nanotubes, and fullerenes have attracted considerable attention in material science. This attention is mainly attributed to graphene's one-atom thickness, large surface area, superior durability, elasticity, high thermal and electrical conductivities since Geim and Novoselov[12] isolated it for the first time in 2004. Graphene family materials are shown in **Figure 2.1**[13].

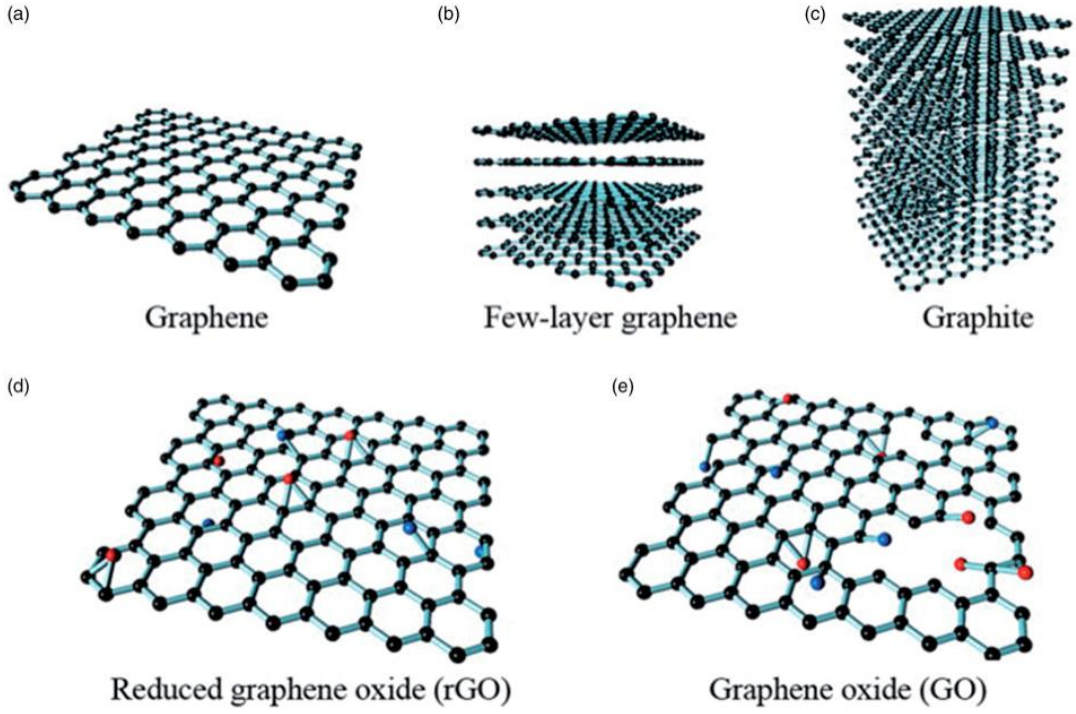

Figure 2.1 Schematic representations of graphene family materials[13]

Graphene and its derivatives are used in a wide range of applications, including sensors[14], super capacitors[15,16], fuel cells[17,18], nanocomposites[19–21], and membranes[22–24] due to their aforementioned superior physical and chemical properties. Over the past decade, various synthesis approaches have been advanced for high-quality graphene. The most common strategies employed for graphene synthesis are chemical vapor deposition (CVD)[25,26], epitaxial growth[27,28], and micro-mechanical exfoliation of highly ordered pyrolytic graphite[29]. Although these strategies can yield graphene with nearly perfect structure and superior properties, graphene oxide reduction allows for a cost-effective and efficient graphene production[30]. In addition to its ability to be converted into graphene easily, having low cost and easy access, graphene oxide can be dispersed in water and polar solvents without aggregation due to its functional groups.

2.1.1 Structure and Properties of Graphene Oxide

GO is obtained by exfoliating graphite oxide via sonication or mechanically stirring to layered sheets[31]. Its graphene-based network and abundant oxygen-containing groups enable GO to immobilize active species and have tunable electronic properties. For example, while GO is insulating due to the sp^3 hybridized carbon atoms in its structure[32], reduced GO (rGO) is a semiconductor, unlike graphene, which is a semimetal[33]. Moreover, GO exhibits exceptional optical and mechanical properties that can be employed in a wide range of applications. By tuning its film thickness and reduction degree, the optical transmittance of GO films can be altered[34]. While the color of its suspension in water varies from dark brown to light yellow, thin films of rGO are semitransparent[35] depending on the oxidation degree and sample thickness. Young's modulus and intrinsic strength of GO changes between 6-42 GPa and 76-293 MPa, respectively[36].

Although a vast amount of research has been done on the subject since its first successful synthesis in 1859 by Brodie[37], the exact structure and composition of GO is still under debate due to its nonstoichiometric composition, strong hygroscopicity, and dependence on synthesis conditions[33]. Therefore, various clashing models have been proposed to understand its structure, as shown in **Figure 2.2**[38].

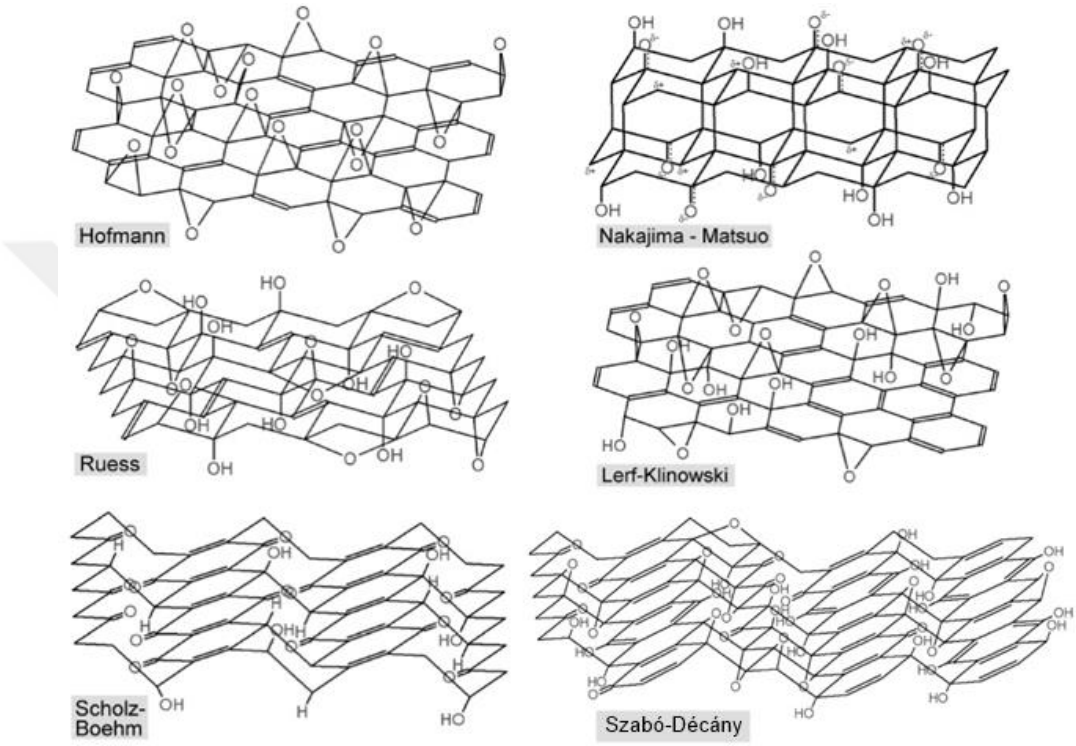

Figure 2.2 Proposed models for GO structure[38]

2.1.2 Synthesis of Graphene Oxide

The synthesis method of GO has evolved and modified various times. These methods use different chemicals and graphite sources and therefore yield GO with different chemical compositions. Brodie[37] synthesized the first batch of GO by adding $KClO_3$ into a mixture of graphite in fuming HNO_3. After washing away the salts, he dried the reaction mixture at 100 °C and repeated this procedure three times until a bright yellow color that does not change with further oxidation was observed. The first improvement in Brodie's method was introduced by Staudenmaier[39], who added

concentrated sulfuric acid to enhance the reaction mixture's acidity and several aliquots of potassium chloride throughout the reaction. This method yielded a much simpler process to synthesize GO; however, the time-consuming addition of potassium chloride and chlorine dioxide emission called for further improvements. In 1958, Hummers and Offeman[40] proposed a new method, including concentrated sulfuric acid, potassium permanganate, and sodium nitrate, to achieve a higher degree of oxidation than the Staudenmaier method within 2 hours. However, it was founded that this final product had GO shells covering incompletely oxidized graphite cores[9]. Several improvements have been made to Hummer's method to increase carbon to oxygen ratio in the final product[41–43]. However, these methods include the generation of toxic NO_x gases. A study conducted by Tour's group did not use sodium nitrite, increased the amount of potassium permanganate, and final product with a higher oxidation degree than the previous methods was achieved while eliminating the emission of toxic gases[44]. The summary of synthesis methods of GO is reported in **Table 2.1**.

Table 2.1 Summary of the methods used to prepare to GO

Method	**Year Developed**	**Oxidant**	**Reaction Media**
Brodie[37]	1859	$KClO_3$	H_2SO_4-HNO_3
Staudenmaier[39]	1898	$KClO_3$	Fuming HNO_3
Hofmann[45]	1937	$KClO_3$	Non-fuming HNO_3
Hummers[40]	1958	$KMnO_4$	H_2SO_4
Tour[44]	2010	$KMnO_4$	H_2SO_4-H_3PO_4
Sun[46]	2013	$KMnO_4$	H_2SO_4
Peng[47]	2015	K_2FeO_4	H_2SO_4

2.2 Aerogels

Aerogel is an extremely light and porous material that exhibits highly attractive physical properties, including large surface area, extremely low thermal conductivity, and adjustable density ranges. Although invented by Samuel Stephens Kistler[48] in 1931, it did not gain widespread attention since the 1980s. Kistler defined aerogel as a gel prepared by replacing the liquid component with air without damage to the solid network[48]. As a result of their excellent properties, aerogels have become the focus of interest in many research fields such as drug delivery[49], tissue engineering[50], cosmetics[51], biocatalysts[52], energy/hydrogen storage[53], construction[54], and thermal insulation[55,56]. Aerogels are usually prepared by supercritical drying or freeze-drying of their hydrogel precursors.

Figure 2.3 shows the most common production method for aerogels[57]. In the first step, sol particles form a continuous network and forms into a gel. In the second step, the network ages and the structure advances. Finally, the gel is dried without disrupting its structure, and the water in the pores is replaced with air[58]. At the final stage, supercritical, atmospheric, or freeze-drying methods are commonly employed[59]. Atmospheric drying is frequently preferred due to its simplicity and low cost. While employing this method, the temperature should be selected carefully considering the solvent used in the gel production. Gel production can occur at high temperatures under inert environment or low temperatures for more extended periods.

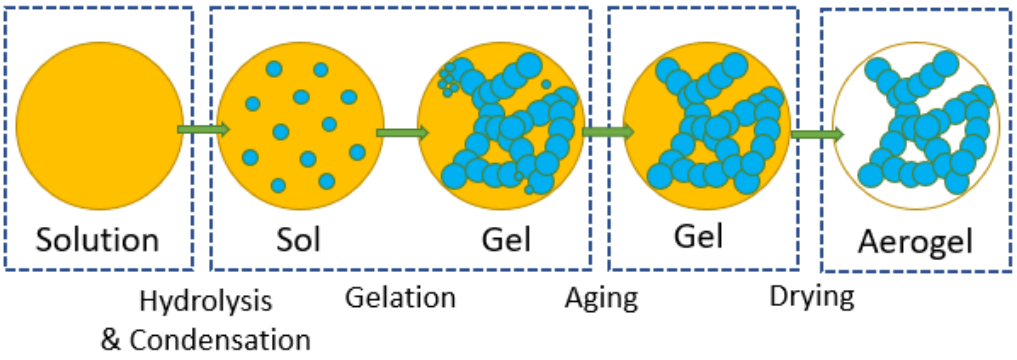

Figure 2.3 General preparation route to prepare aerogels[57]

For the years following its invention, aerogel studies were limited with silica, non-silica, and resorcinol formaldehyde. During its development, aerogel studies experienced several vital innovations. Before the 1980s, the aerogel preparation method was time-consuming, and its washing process was regarded as unpractical. Studies conducted by Russo's group in 1986, which replaced the water systems with an organic solvent to prepare aerogels that yielded in a faster process, are of the crucial innovations in the topic. The topic has undergone another change in the 1990s after the development of surface-modified ambient drying. These developments led to extensive research in the field and production of many different types of aerogels. Some of the existing applications of different types of aerogels are given in **Table 2.2**.

Table 2.2 Classification of aerogels[57] and examples from the literature on their existing applications

Aerogels		Application
Single Component		
Oxide	TiO_2[60], SiO_2[61]	Catalysts
Organic	RF[62], Cellulose[50]	Biosensors, tissue engineering
Carbon	CNT[53], Graphene[63]	Hydrogen storage, oil absorbent
Chalcogenide	PbS, CdSe, CdS, and ZnS[64]	Semiconductors
Others	NbC[65]	Electrocatalysts
Composite		
Multi-composition	ZnO-SnO_2[66],	Photocatalysts,
Gradient	Density[67], composition[68]	Various
Micro-/Nanocomposites	GO-based[69], silica-based[70]	Oil absorbent, space applications

2.3 Graphene Oxide Based Aerogels

GO is the most appropriate precursor for 3D graphene materials due to its dispersibility in polar and organic solvents and functionality. Moreover, GO is a very beneficial precursor thanks to oxygen-containing functional groups on its basal planes and edges, which are reactive to various compounds and can produce novel materials with tunable properties. As a result, GO-based aerogels exhibit excellent properties and have great potential in environmental applications. The main environmental applications and removal mechanism of GO-based aerogels are given in **Figure 2.4**[71].

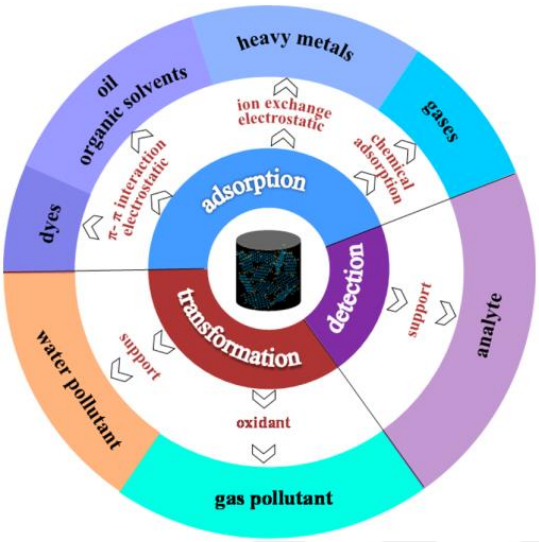

Figure 2.4 Environmental applications and removal mechanisms for different pollutants[71]

2.3.1 Synthesis of Graphene Oxide Based Aerogels

Several strategies have been employed for GO-based aerogel synthesis. These strategies can be classified as template-free self-assembly methods, template-assisted methods, and other methods, including CVD[72], 3D printing[73,74], and spark plasma sintering[75].

Template-free self-assembly methods are commonly employed for GO-based aerogel synthesis since many factors can facilitate GO gelation such as cross-linker, reducing agent additions, or pH alterations[76]. Since the dimensions of GO sheets are much higher than most of the polymers, they can interact with each other, even in diluted concentrations[77]. In addition to their hydrophilic oxygen-containing functional groups, as a result of the electrostatic repulsion between carbonyl groups, which prevents aggregation, GO sheets can form stable dispersions in water[78]. When the pH of GO dispersion decreases, the electrostatic repulsion between carbonyl groups weakens, resulting in flocculent formation. However, if the GO concentration is sufficiently high, gelation occurs instead of amorphous precipitation[78]. Moreover, gelation of GO can also be promoted via hydrothermal and direct freeze-drying

techniques[76]. In the literature, there exist mainly three routes for the template-free self-assembly of GO-based aerogels: i) hydrothermal synthesis, ii) chemical reduction, iii) cross-linking synthesis[76].

Hydrothermal synthesis, when compared with other methods, is a much more accessible, environmentally friendly, and efficient method. However, this method usually needs long reaction times, high temperatures, or high pressures[79]. Shi and coworkers[80] following the GO's colloidal chemistry employed hydrothermal treatment at 180 °C for durations between 1-12 h for initial GO concentration 0.5. 1 and 2 mg/mL to produce graphene hydrogels. Photographs of products are given in **Figure 2.5**. After freeze-drying the hydrogels, Shi and coworkers achieved mechanically strong and thermally stable monoliths with macroporous cellular-type structure.

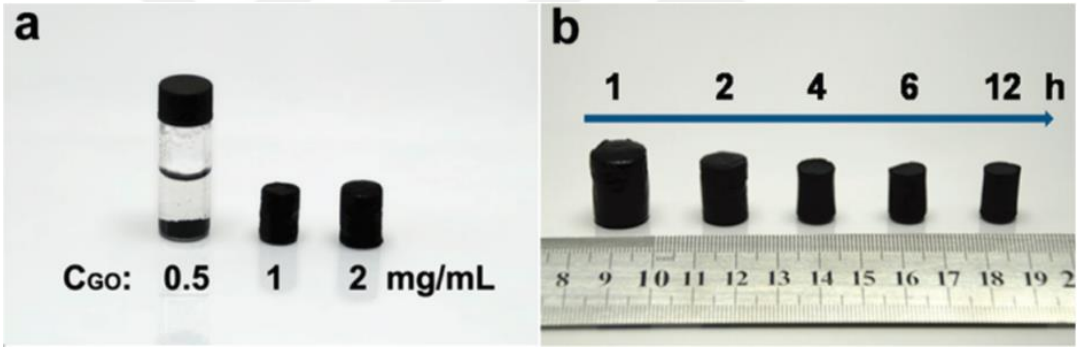

Figure 2.5 (a) Products after hydrothermal reduction at 180 °C for 12 h (b) Products after hydrothermal reduction of 2 mg/mL GO aqueous dispersion at 180 °C for different durations[80]

In the chemical reduction method, reducing agents are employed to restore the sp^2 network. This method can result in a small surface area aerogel since graphene layers restack through a π-π interaction during the synthesis[79]. Within the chemical reduction methods, hydrazine and hydriodic acid (HI) are the most commonly used reducing agents. Aradilla *et al.*[81] employed a single step process to produce graphene hydrogels using hydrazine, ethylenediamine, and 1,4 diamino butane as reducing agents at 80 °C for 24 h. Hydrogels prepared with hydrazine exhibited high electrical conductivity and excellent supercapacitor properties.

Furthermore, in their study Zhang *et al.*[82] produced graphene aerogels reduced with L-ascorbic acid. Aerogels showed high electrical conductivity, large surface area, and hierarchically porous structure. The authors also stated that, contrary to other reducing agents, including hydrazine, NaBH4, and LiAlH4, L-ascorbic acid reduction resulted in no gaseous by-products. Photographs of the final products, graphene hydrogel and graphene aerogels, can be seen in **Figure 2.6**.

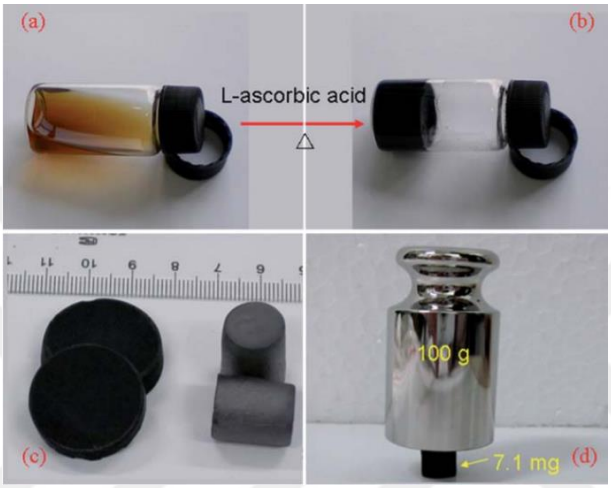

Figure 2.6 (a) GO dispersion, (b) graphene hydrogel after L-ascorbic acid reduction, (c) graphene aerogels prepared via (left) supercritical CO_2 and (right) freeze-drying, (d) 7.1 mg graphene aerogel supporting more than 14000 times its weight[82]

Finally, cross-linking methods can be employed for template-free GO-based aerogel production. These methods can include cross-linking agents strengthening the hydrogen bonds between the GO sheets or divalent and trivalent ions. For instance, Jiang *et al.*[83] produced gel-like products by employing both hydrothermal treatments at 120 °C for 10 hours and divalent atoms Ca^{+2}, $Co^{+2,}$ and Ni^{+2}. Photographs of the final products can be seen in **Figure 2.7**.

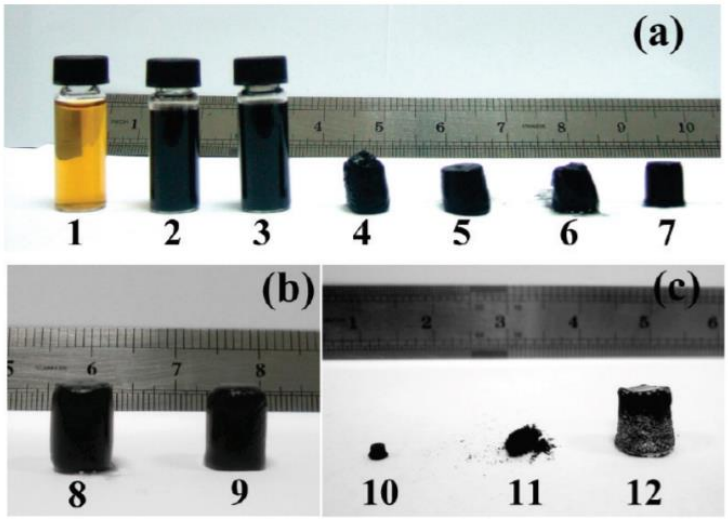

Figure 2.7 (a) GO before (1) and after hydrothermal reduction (2). rGO mixed with Ca^{2+} (3) and rGO cylinders assembled by Ca^{2+} with various Ca to GO weight ratios (4,5,6,7). (b) rGO cylinders assembled by (8) Ni^{2+} and (9) Co^{2+} (c) Ca2+ linked rGO samples dried by (10) natural evaporation and freeze-drying (11) without and (12) with PVA strengthening[83]

From **Figure 2.7**, it can be seen that aerogel formation was only observed after the addition of polyvinyl alcohol (PVA) as an additional cross-linker.

Common cross-linking agents employed to promote gelation are hydroxyl, oxygen-containing, and nitrogen functional groups. For example, in the study of Doğan[69] 1,3-diamino propane (1,3-DAP) was employed to promote gelation. Although gelation was not observed for pure GO dispersion at 95 °C for 6 h, hydrogel formation was observed after the addition of 1,3-DAP.

Template assisted methods are usually preferred due to their simplicity and ability to produce uniform macropores and tailorable microstructure[79]. These methods typically include freezing of homogeneous GO dispersions and later freeze-drying of the cryogels[84]. Unidirectional freezing can create larger pores and a more ordered structure than non-directional freezing. Additionally, while the pore diameter is independent of GO concentration for unidirectional freezing, it increases with decreasing GO concentration in non-directional freezing[85]. Since with small GO

concentrations (<10 mg/mL) resulting in aerogel tends to be fragile, the addition of polymers or curing treatments is generally employed[86].

It should also be noted that hydrothermal and chemical reduction after template-free or template-assisted methods are also commonly applied to increase final structures' strength. For example, Giannelis *et al.*[87] produced hydrogels with GO, Nafion, and chloroplatinic acid. After unidirectional freeze-drying, aerogels were reduced with hydrazine and monosodium citrate to secure the structure. Produced aerogels are found to be promising candidates for fuel cell and biosensor applications.

Shi and Zhang[88] have also researched reducing treatments after aerogel production. They fabricated graphene hydrogels reduced via hydrothermal treatment followed by hydrazine and HI reduction, aiming to increase the final products' conductivity. Hydrogels were found to have great potential in supercapacitor applications and have shown improvements in their retention capacity compared to hydrogels that are not reduced. In their study, Lin *et al.*[89] further reduced GO aerogels under Argon atmosphere at 1050 °C. Hydrophobicity of the resulted aerogels has increased remarkably.

2.3.2 Graphene Oxide Based Aerogels for Pollutant Removal

Understanding of the removal process and mechanism of different pollutants is vital to produce GO-based aerogels with enhanced adsorption and absorption capacities. Nevertheless, due to GO-based aerogels' particular characteristics, investigation of oil and dye removal mechanisms is a complex issue that requires a detailed analysis of adsorption parameters. Determined by the different functional groups of GO-based aerogels, contaminant chemistry, and adsorption parameters such as solution pH, contaminant concentration, and temperature, electrostatic interactions, hydrophobic interactions, and π-π interactions take place[90]. The removal mechanism of GO-based aerogels can generally be described as combining these interactions that occur simultaneously[91].

2.3.2.1 Mechanisms of Pollutant Removal by GO Aerogels

Their nature determines the removal process of contaminants by GO aerogels. While dyes and heavy metals are separated via adsorption on the exterior of GO aerogels, oil and organic solvents are separated via absorption in the pores of GO aerogels[92]. As a result of their large pore volumes, GO aerogels have much higher removal capacities toward oil and organic solvents than dyes and heavy metals.

Adsorption is a physicochemical process commonly applied for water and wastewater treatment. During adsorption, a molecule or an ion in a gaseous or liquid bulk attaches onto a solid's surface. Adsorption is a surface process where only the adsorbent surface is concerned. In absorption, on the other hand, adsorbate diffuses into the adsorbent structure[93]. Sorption, in general, occurs in four steps[5]:

- Bulk diffusion from fluid to the boundary layer of the adsorbent,
- External film diffusion from the boundary layer to surface sites of adsorbent,
- Internal mass transfer within the particle pores, and
- Physical attachment to the adsorbent surface

Adsorption occurs when the adsorbate's potential energy is below the potential energy of the adsorbate at the bulk liquid phase. Therefore, adsorption can be classified as physical adsorption or chemisorption based on the adsorbent's surface forces. In physical adsorption, electrostatic forces, together with Van der Waals forces, are present at the adsorbent surface. These are weak interactions that ease the desorption process. On the other hand, the forces governing chemisorption are much stronger and involve electron transfer or sharing interactions. Therefore, chemisorption usually requires greater adsorption energy than physical adsorption[94].

2.3.2.1.1 Adsorption Isotherms

The adsorption isotherm is required to understand the interaction between the adsorbate and the adsorbent. It can also provide insights about the distribution of

adsorbate molecules between the liquid and solid phases at the equilibrium[95]. It is also crucial to optimize the use of adsorbent. Isotherm models, including Langmuir, Freundlich, Temkin, and Dubinin-Radushkevic, can be employed to understand the adsorption mechanism. The two most common models among these are Langmuir and Freundlich, isotherm models.

Langmuir adsorption model assumes monolayer adsorption at or before reaching a relative pressure unity. Even though isotherm was initially proposed by Langmuir to describe the chemisorption process, the model can also describe systems with moderately low coverage[96]. The non-linear form of the Langmuir isotherm model is given in Equation 1.

$$Q_e = \frac{Q_m K_L C_e}{1 + K_L C_e} \quad (1)$$

Where Q_e is adsorption capacity at equilibrium (mg/g), C_e is the solute concentration at equilibrium (mg/L), K_L is Langmuir adsorption constant (L/mg), and Q_m is the theoretical maximum adsorption capacity (mg/g).

Freundlich adsorption model assumes that the adsorbent surface is heterogeneous, and multilayer adsorption occurs on the surface. Freundlich's model also assumes that adsorption capacity changes proportional to adsorbate concentration. The non-linear form of the Freundlich isotherm model is given in Equation 2.

$$Q_e = K_F C_e^{\frac{1}{n}} \quad (2)$$

K_F is Freundlich adsorption constant (L/mg), and 1/n is constant for adsorption intensity.

The accuracy of the isotherm model to express the adsorption process is often decided by comparing the correlation coefficients, R^2, of the respective linear fits. The linear form of the Langmuir isotherm model is given in Equation 3.

$$\frac{C_e}{Q_e} = \frac{1}{K_L Q_m} - \frac{C_e}{Q_m} \quad (3)$$

The values of Q_m and K_L can be found from the slope and intercept of the plot for C_e/Q_e vs. C_e. To detail the characteristics of Langmuir isotherm, dimensionless separation factor R_L can be calculated. The value of R_L explains if the adsorption is favorable or unfavorable and linear or irreversible. R_L is represented as:

$$R_L = \frac{1}{1 + K_L C_0} \tag{4}$$

Where C_0 is the initial adsorbate concentration in solution.

For the Freundlich isotherm model, the linear form is given in Equation 5.

$$\ln Q_e = \ln K_F - \frac{1}{n} \ln C_e \tag{5}$$

The intercept and slope of ln (Q_e) vs. ln (C_e) give K_F and 1/n. The values of 1/n explain the surface heterogeneity. While values below 0 indicate heterogeneous adsorption, the values between 1 and 0 indicate Langmuir isotherm. The values above 1, on the other hand, hints at cooperative adsorption[97].

2.3.2.1.2 Adsorption Kinetics

The study of adsorption kinetics is necessary to determine the adsorption rate. To describe adsorption kinetics, several models have been developed. The most common kinetic models used for adsorption processes are pseudo-first and pseudo-second-order models.

The pseudo-first-order model can be presented as:

$$\log(Q_e - Q_t) = \log(Q_e) - \frac{k_1}{2.303} t \tag{6}$$

Where Q_t is the adsorption capacity at time t, and k_1 is the rate constant of pseudo-first-order. The values of k_1 and Q_e can be calculated from the slope and intercept of linear fittings of log (Q_e – Q_t) versus t. Meanwhile, the pseudo-second-order model is given by:

$$\frac{t}{Q_t} = \frac{1}{k_2 {Q_e}^2} - \frac{t}{Q_e} \quad (7)$$

Where k_2 is the rate constant of pseudo-second-order. Similarly, k_2 and Q_e values can be determined from the slope and intercept of linear fittings of t/Q_t versus t. In addition to these models, modified Freundlich and intra-particle diffusion models can be used for kinetic studies. The linear form of the modified Freundlich equation is given as[98]:

$$\ln(Q_t) = \ln(kC_0) + \frac{1}{m}\ln(t) \quad (8)$$

Where C_0 is the initial concentration of the dye, m is the Kuo–Lotse constant and k is the apparent adsorption rate constant. The rate parameter for intraparticle diffusion is determined using the following equation[99]:

$$Q_t = k_i t^{\frac{1}{2}} + C \quad (9)$$

Where C is the intercept and k_i is the intraparticle diffusion rate constant. The plot of the intra-particle diffusion model may exhibit multilinearity. Generally, it can show three steps: a sharp increase due to the diffusion of adsorbate through the solution, intra-particle diffusion where gradual adsorption occurs and finally, the equilibrium stage[99].

2.3.2.2 Graphene Oxide Based Aerogels for Dye Adsorption

Dye adsorption on GO aerogels is governed by a mix of electrostatic forces and π–π interactions. Due to the deprotonation of oxygen-containing functional groups of GO, it has been extensively documented that GO-based aerogels have high negative surface charge density at environmentally relevant pH[100–103]. As a result, GO-based aerogels have proven to have the potential for cationic dyes' adsorption and positively charged contaminants.

In their study, Du *et al*[104] prepared graphene melamine aerogels for methylene blue (MB) and orange G (OG) removal from water with maximum adsorption capacities of 286.5 mg/g and 80.51 mg/g, respectively. Aerogels showed excellent recyclability potential for MB maintaining their removal efficiency by 98% after the 5th cycle and 95% after the 10th cycle and potential applications for fast MB removal, which can be seen from **Figure 2.8**.

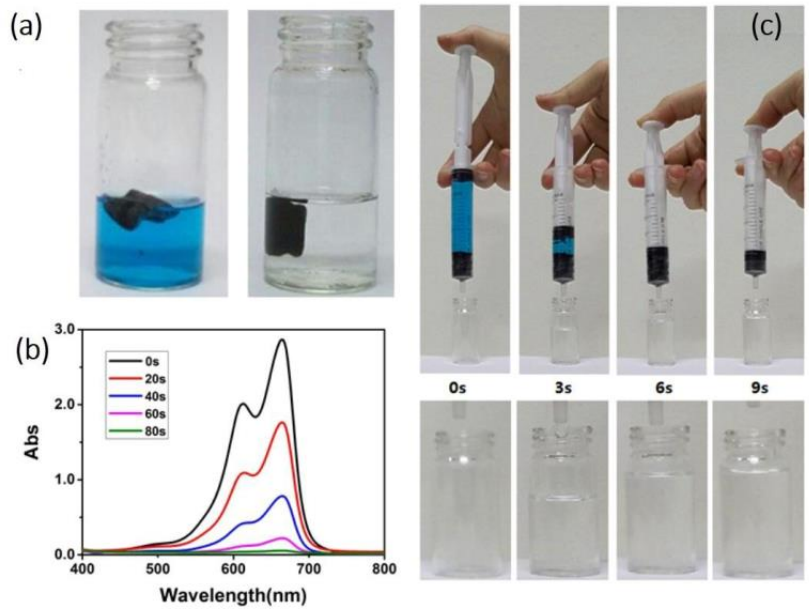

Figure 2.8 (a) Photographs of MB solution before and after adsorption. (b) The UV spectrum of MB solution at different contact times. (c) Photographs of fast-compressible test for MB-water separation[104]

Moreover, in the study of Zhao *et al*[105] carboxylated GO aerogels were prepared for MB removal with maximum adsorption capacities of 780 mg/g. They concluded that the reason for the increase in adsorption capacity is the strong electrostatic interaction between carboxyl groups and MB molecules, which was the governing adsorption force. However, aerogels showed poor recyclability losing 80% of their original adsorption capacity after the first cycle. While the strong interaction increased the removal performance, it also hindered the recyclability performance since after the first cycle MB covered most adsorptive sites of the aerogels and could not be washed away with acidic water a pH of 3, which made recycling difficult[105].

In their study, Sarkar *et al*[106] produced sponge-like materials with GO functionalized with chitosan(CS)/poly(methacrylic acid) and in situ-developed Fe_3O_4 nanoparticles. Materials achieved a maximum adsorption capacity of 2478 mg/g, and their adsorption and recyclability performance can be seen in **Figure 2.9**. The use of Fe_3O_4 nanoparticles eased the separation of sponges from the solution.

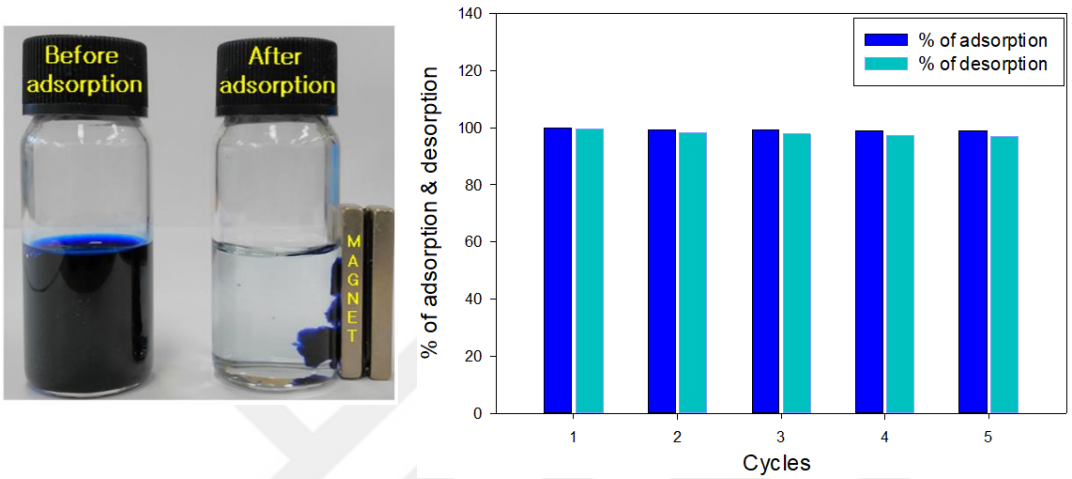

Figure 2.9 (Left) Photographs of MB before and after adsorption (Right) Adsorption-desorption cycles of MB dye adsorbed cl-CS-p(MA/GO-Fe_3O_4) NPs[106]

However, aerogels showed inadequate adsorption capacity for OG due to electrostatic repulsion. While the high negative surface area provides GO-based aerogels with adequate adsorption capacity for cationic dyes, it also hinders their adsorption capacity for anionic dyes due to the electrostatic repulsion between the anionic dyes and GO[107]. Their adsorption capacity toward anionic dyes can be enhanced by grafting positively charged functional groups or incorporating positively charged polymers into their structure.

In their study, Li *et al.*[108] produced GO-CS hydrogels via the self-assembly method. They used CS to overcome the electrostatic repulsion between GO and Eosin Y, an anionic dye. Since both GO and CS have multiple charges, some of their charges canceled each other. Nevertheless, as the results showed, there were still sufficient free charged sites to promote adsorption. Hydrogels were proved to be broad-

spectrum adsorbents achieving maximum adsorption capacities of 320 mg/g and 300 mg/g for Eosin Y and MB.

Moreover, in their study, Han e*t al.*[109] fabricated GO and polyethyleneimine (PEI) aerogel for Amaranth, Orange G (OG), and Rhodamine B (RhB) adsorption. Aerogels achieved maximum adsorption capacities of 800 mg/g and 300 mg/g for Amaranth and OG, both anionic dyes. However, they were unable to adsorb cationic dye RhB. It was also observed that with increasing PEI, adsorption capacities of aerogels toward the anionic dyes also increased.

Other than electrostatic interactions, as a result of its sp^2 hybridized structure, GO can form π–π bonding with the aromatic rings of dyes. Therefore, bare GO aerogels can adsorb anionic dyes via π–π interactions, and their capacity can be further enhanced after functionalization with positively charged groups. For instance, in their study Duan *et al.*[84] produced polydopamine functionalized graphene hydrogels for heavy metal and dye adsorption. Hydrogels achieved a maximum adsorption capacity of 325 mg/g for *p*-nitrophenol at low pH values since, in its neutral form, adsorption occurred via π–π interactions and hydrogen bonding. However, increasing pH caused the formation of phenolate anions, which significantly reduced the adsorption capacity of hydrogels due to electrostatic repulsion. Efficient adsorption of neutral dyes proves that π–π interactions also play a role in the dye removal mechanism.

Finally, hydrogen bonding can also help the adsorption of dyes containing carboxyl and hydroxyl groups such as Eosin Y, RhB, and Direct Red 80 (DR80). In their study Nemade *et al.*[110] fabricated methylimidazolium ionic-liquid-functionalized GO (mimGO) aerogels. At pH values between neutral to low, mimGO aerogel exhibited positive charge due to protonation of imidazolium ionic liquid, amide linkages, and carboxyl groups, which formed intense electrostatic interactions with sulfonic acid groups of anionic dye DR80. Additionally, hydrogen bonding and π−π interactions between mimGO and DR80 also contribute toward adsorption. A combination of these three mechanisms significantly increased the adsorption rate compared to

unfunctionalized GO. Removal performance and mechanism of mimGO aerogel toward DR80 can be seen in **Figure 2.10**.

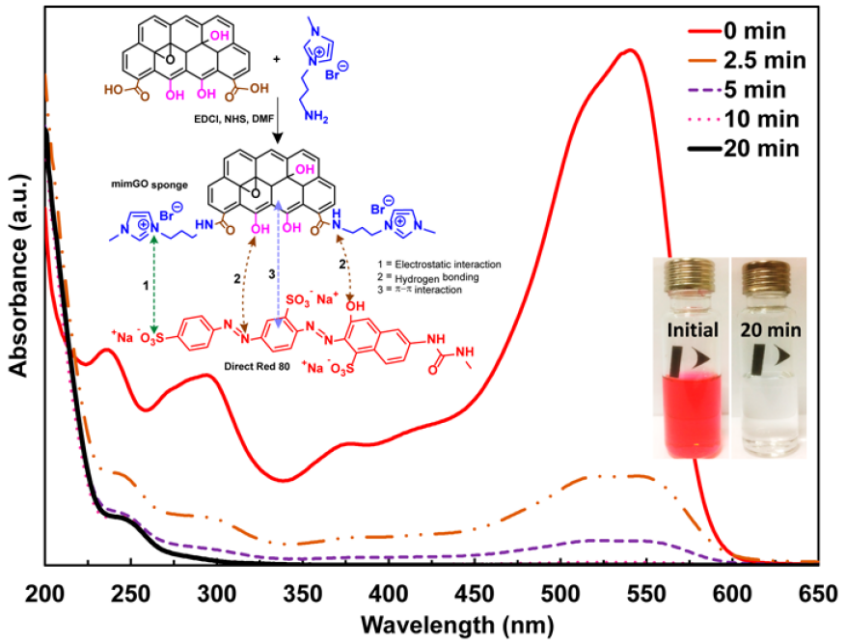

Figure 2.10 Removal performance of mimGO aerogel and adsorption mechanism for DR80[110]

Table 2.3 gives a systematic comparison of the adsorption properties of GO-based aerogels for dyes. As shown from the table, adsorption of GO-based aerogels toward dyes often followed the Langmuir Isotherm model, which indicates that active sites were evenly distributed, and monolayer adsorption took place. Moreover, pseudo-second-order kinetic was the most common model proposed.

Table 2.3 The adsorption performance of GO-based aerogels for dyes

Adsorbent	Dye	Kinetic	Isotherm	Ref.
GO/Melamine Aerogel	MB OG	Pseudo second order Pseudo second order	Langmuir Langmuir	[104]
CS/GO/Carboxymethyl Cellulose Aerogel Globules	MB	Pseudo second order	Langmuir	[111]
Sodium Alginate/GO Aerogel	MB	Pseudo second order	Langmuir	[112]
CS/p(MA)/GO Aerogel	MB	Pseudo first order	Sips	[106]
CS/GO Aerogel	MB	Pseudo second order	Langmuir	[113]
Polyacrylamide/GO Aerogel	MB Rh6G	Pseudo second order Pseudo second order	Langmuir Langmuir	[114]
CS/GO Microspheres	MB	Pseudo second order	Langmuir	[115]
Polyacrylamide/GO Aerogel	MB	Pseudo second order	Langmuir	[116]
Proanthocyanidin/GO Aerogel	MB	Pseudo second order	Langmuir	[117]
Carboxylated GO Aerogel	MB	Intra-particle model	Freundlich	[105]
Silk Fibroin/GO Aerogel	MB	Pseudo second order	Langmuir	[118]
MimGO Aerogel	DR80	Pseudo second order	Langmuir	[110]
MgO/GO Microspheres	Congo Red	Pseudo second order	Langmuir	[119]
Polyaniline/Fe_3O_4/GO Nanocomposite	Congo Red	Pseudo second order	Langmuir	[103]
Polyethersulfone/GO Core/Shell Particles	MB	Pseudo first order	Langmuir	[120]

2.3.2.3 Graphene Oxide Based Aerogels for Oil and Organic Solvent Absorption

Oil spills, as well as organic solvent spills, are detrimental to the environment. To achieve efficient clean-up of spills, lightweight oleophilic sorbents with high surface areas are needed. However, most of the conventional sorbents used in these applications suffer from compact pores that hinder the diffusion of high-viscosity fluids, including crude oil[92]. Therefore, GO-based aerogels with their high surface area, tunable pore formation, and versatile surface chemistry have gained attention. Several properties of GO can be altered to enhance its pollutant removal performance. After partial reduction of oxygen-containing functional groups, hydrophobic and oleophilic sp^2 domains of GO can be re-established[92]. Moreover, GO-based aerogels can be chemically or hydrothermally reduced to obtain more sp^2 domains, enhancing their interaction with oil and organic solvents. Many researchers have reported an increase in contact angle for water and oil removal capacity after partial reduction of GO-based aerogels.

For example, in their study, Jiang *et al.*[121] fabricated polyurethane/GO aerogels via hydrothermal self-assembly method at 95 °C for 6 hours, which exhibited high capability (99.5% efficiency) for removal of oils from water even after 50 cycles because of the robust interconnected network and stable porous structure. Hydrophobic π–π interactions were crucial for the adsorption process. Photographs depicting continuous diesel–water separation can be seen in **Figure 2.11**.

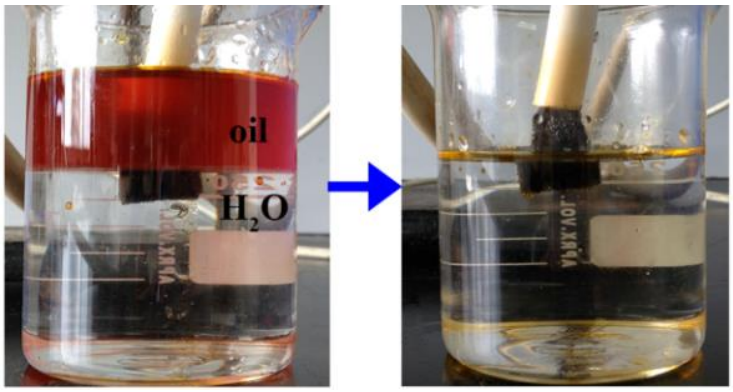

Figure 2.11 Photographs of the diesel-water system before and after continuous adsorption[121]

In their study, Liu *et al*[63] prepared an aqueous dispersion of GO, which was chemically reduced with ethylenediamine (EDA). They reduced the mixture at 90 °C for 5 h, and produced hydrogel was further reduced with ammonia. Aerogels achieved adsorption capacities towards oil up to 130 g/g. The mechanism of EDA-ammonia reduction of GO and SEM images of the aerogel is given in **Figure 2.12**.

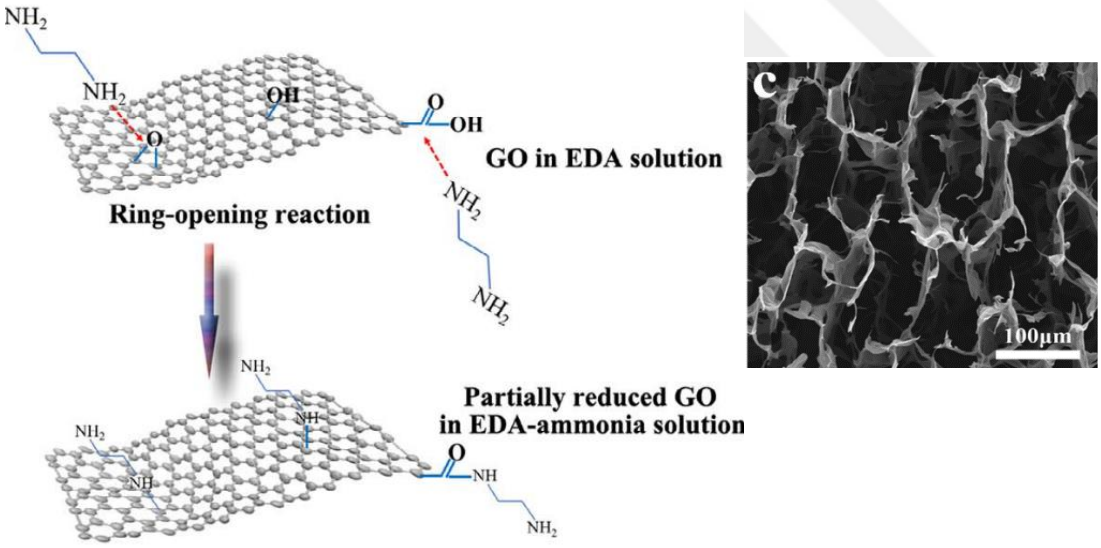

Figure 2.12 EDA-ammonia reduction of GO (left) and SEM image of the aerogel (right)[63]

In the study of Doğan[69], aerogels were prepared using 1,3-DAP and GO. 1,3-DAP successfully reacted with GO's functional groups and led to hydrogel formation at 95 °C after 6 hours. As can be seen from **Figure 2.13**, aerogels were able to absorb

chloroform from the water quickly. In batch absorption experiments, they achieved the maximum absorption capacity of 550 g/g for chloroform.

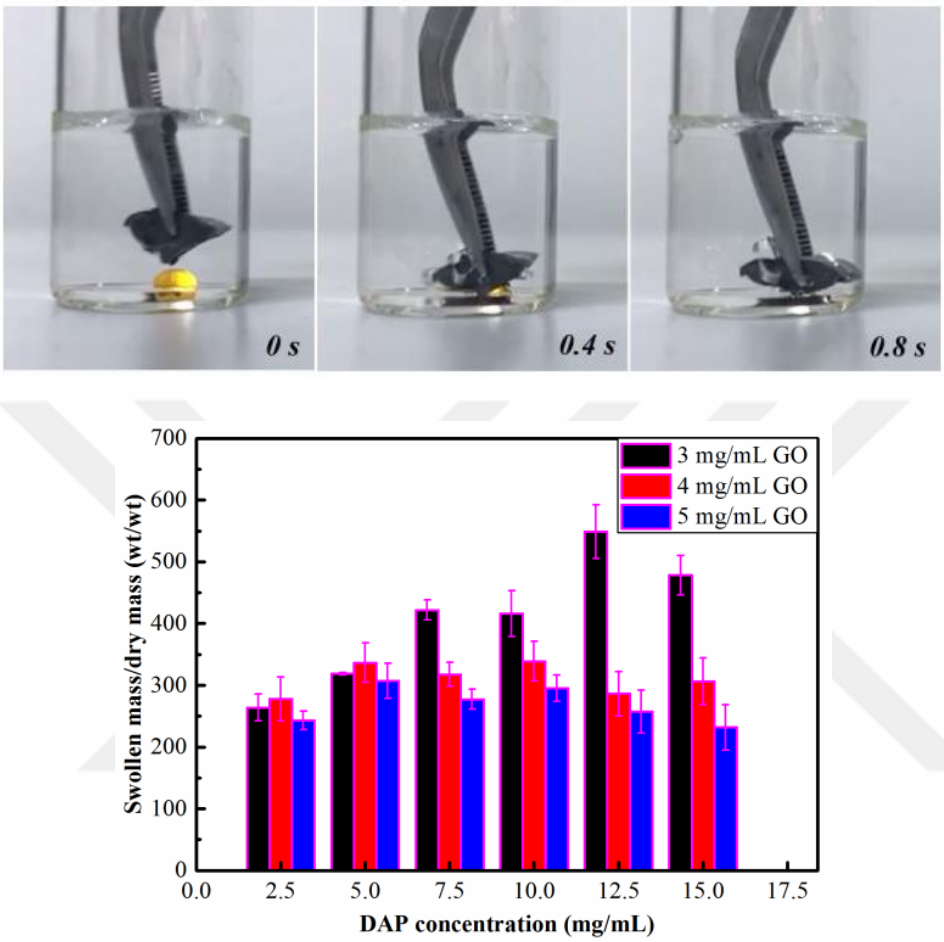

Figure 2.13 Photographs of methyl-red dyed chloroform adsorption from the water with DAP/rGO aerogel (top), absorption capacities of aerogels for chloroform (bottom)[69]

In their study, Sun and coworkers[11] fabricated GO aerogel via freeze-casting method followed by hydrothermal reduction at 1000 °C for 20 minutes. Aerogels exhibited a significant increase in their absorption capacities with respect to previously reported GO aerogels produced by the same team via liquid-phase reduction followed by freeze casting[122]. A comparison of the absorption capacities of the aerogels is given in **Figure 2.14**.

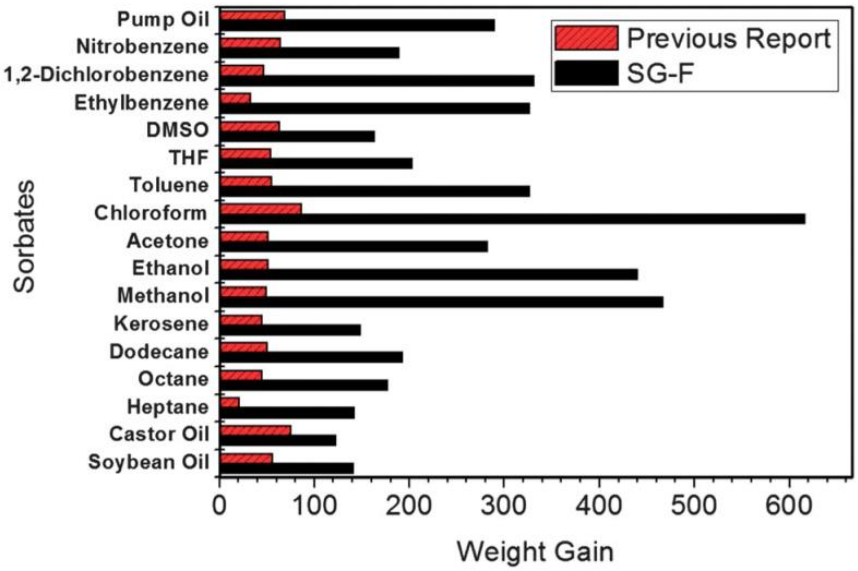

Figure 2.14 Absorption performance of aerogels towards various organic chemicals[11]

Another commonly employed method is the incorporation of oleophilic components. For example, Chen *et al*[123] produced ultralight and fire-resistant lignin-modified graphene aerogels (LGA), a potential candidate for oil and toxic organic solvent clean-ups with high efficiency and recyclability while at the same time utilizing biomass waste. After hydrothermal reduction at 180 °C for 12 h, produced aerogel maintained its shape after the compressive-recovery process and exhibited excellent oil and organic solvent absorption capacity[123], shown in **Figure 2.15**.

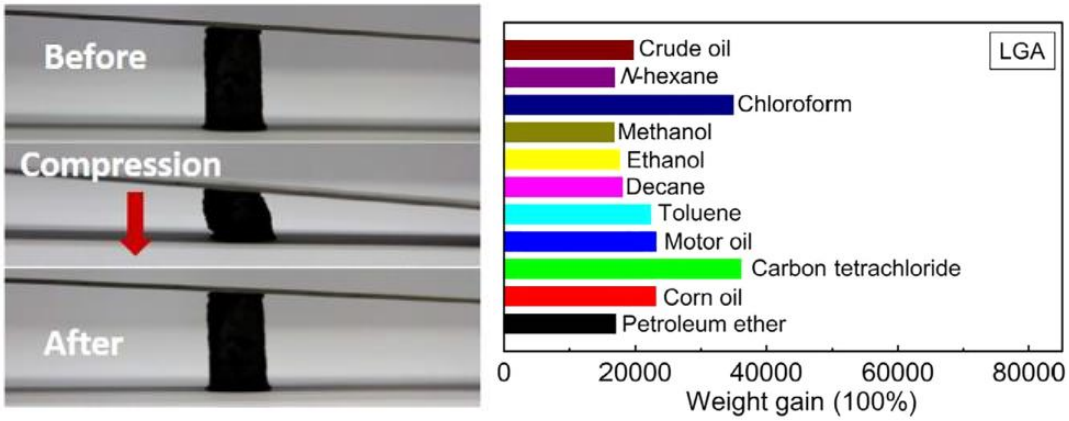

Figure 2.15 Photographs of an LGA during the compressive and recovery process (left), Absorption capacities of aerogels for different oils and organic solvents (right)[123]

In the study of Li e*t al.*[124], aerogels were covalently assembled by pyrrole and via hydrothermal reduction. As a result of the π-π interactions, aerogels could absorb aromatic compounds such as toluene and benzene. Additionally, the absorption of hydrocarbons like kerosene and diesel on polypyrrole/GO aerogel van der Waals forces played an important role. Yang *et al.*[125] produced monolithic graphene aerogels modified with 1H,1H,2H,2H-perfluorooctyltriethoxysilane. Aerogels displayed superhydrophobic and super oleophilic properties. Absorption capacities of aerogels varied between 109 g/g and 236 g/g, as shown in **Figure 2.16**.

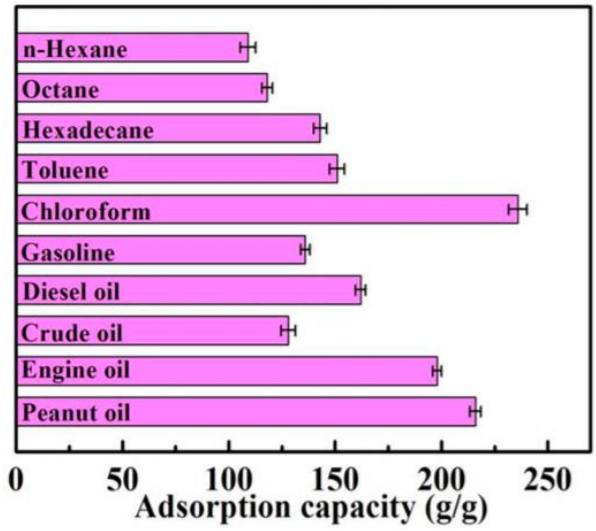

Figure 2.16 Removal performance of the aerogels for organic solvents and oils[125]

Chemistry of oils and organic solvents is also involved in the absorption process. Properties such as density, volatility, and viscosity can also influence absorption. GO-based aerogels can exhibit higher absorption capacities for high-density oils since more oil can be absorbed into the pores. Moreover, absorption capacities for volatile oils, including gasoline and diesel oil, are usually lower since they can quickly vaporize. Finally, if the viscosity of oil or organic solvent is high, diffusion can decelerate, decreasing the absorption capacity of the aerogel[71].

Although numerous research has been conducted for the production of GO-based aerogels for pollutant removal, the production of GO-based adsorbents with high structural stability while preserving its high adsorption/absorption capacity remains a challenge. Therefore, there is still a need to develop new GO-based aerogel production methods, which can offer good recyclability and good pollutant removal performance.

CHAPTER 3

MATERIALS AND METHODS

3.1 Materials

Physical properties of the chemicals used in experimentations are given in **Table 3.1**, along with information about the compound's source.

Table 3.1 Physical properties of chemicals used in experiments

Material	**ρ (g/mL)**	**Mw (g/mol)**	**Purchased from**
Graphite	-	12.01	Asbury Carbons*
$KMnO_4$	-	158.03	Yenilab
H_2SO_4	1.84	98.08	Honeywell
H_3PO_4	1.74	98.00	VWR
H_2O_2	1.11	34.02	Merck
HCl	1.20	36.46	Sigma-Aldrich
APTES	1.02	179.29	Alfa Aesar
Acetone	0.791	58.08	Sigma-Aldrich
Chloroform	1.492	119.38	Sigma-Aldrich
DMF	0.944	73.09	Sigma-Aldrich
Toluene	0.87	92.14	Merck

* Graphite flakes with an average size of 300 μm were kindly supplied from Asbury Carbons.

3.2 Methods

3.2.1 Synthesis of Graphene Oxide

Graphene oxide was synthesized from graphite flakes by Tour method[44]. Graphite (1.05 g) was mixed with potassium permanganate ($KMnO_4$) (6.3 g) to prepare a 6:1 graphite/$KMnO_4$ mixture. 9:1 mixture of concentrated sulfuric acid/orthophosphoric acid (H_2SO_4/H_3PO_4) (126:14 mL) solution was added to the mixture while stirring in a water bath to prevent sudden temperature increase. The reaction mixture was

successfully transferred to a 50 °C oil bath for 12 h, forming a thick paste. After the reaction was cooled to room temperature, 140 g ice was added. In order to remove the excess MnO_4^- ions[44], 30% hydrogen peroxide (H_2O_2) was added, turning the color of the solution to bright yellow. The reaction is illustrated in the scheme provided in **Figure 3.1**.

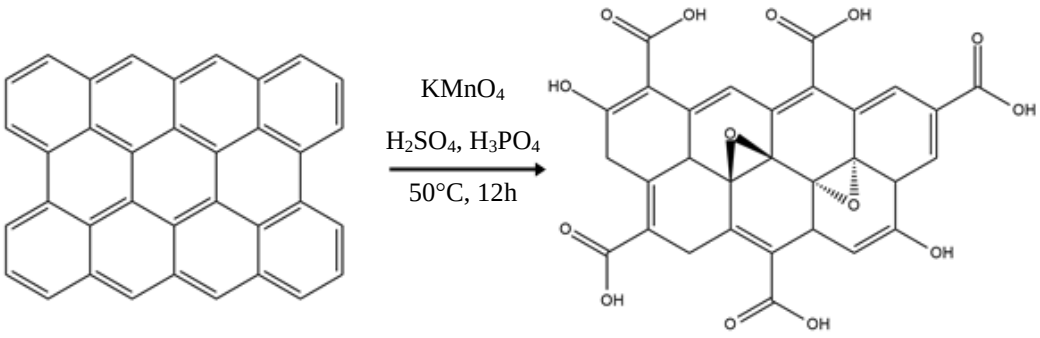

Figure 3.1 Schematic representation of GO synthesis from graphite

Then, the reaction mixture is centrifuged, and the highly acidic supernatant of the product was decanted away. The reaction mixture was then washed with 3.4 wt % hydrochloric acid (HCl) three times[126] and acetone-ethanol mix 4 times. The final product was dried under vacuum and stored at -20 °C to minimize the environmental effects.

3.2.2 Production of Reduced Graphene Oxide and Stearic Acid Based Aerogels

Before aerogel production, experiments were performed to find the optimum GO concentration and gel formation temperature for oil and organic solvent absorption. Optimization results can be seen in Figure D. 1. GO concentration of 5 mg/mL was selected instead of 3 mg/mL since higher GO concentration yielded aerogels with higher shape stability. The reaction temperature of 145 °C was selected, and further thermal reduction at 150 °C was employed since they yielded aerogels with higher absorption capacity. GO dispersions of 5 mg/mL and stearic acid (SA) solutions were

prepared in DMF. These were then mixed in desired SA weight ratios (0%, 20%, 50%, 60%) and transferred into vials. Samples were then sonicated in an ice bath to achieve homogenization and remove bubbles in the solutions. After sonication, bottles were then placed into an oven at 145 °C for 5 h. After being removed from the oven, organogels were washed with ethanol, ethanol-water mixtures, and water to remove unreacted components. Obtained hydrogels were freeze-dried at -53 °C. Subsequently, aerogels were thermally reduced at 150 °C for 4 h after being subjected to argon flow for 15 minutes. Aerogels were denoted as rGO, SG20, SG50, and SG60 based on the weight ratios. The reaction between GO and SA is illustrated in **Figure 3.2**.

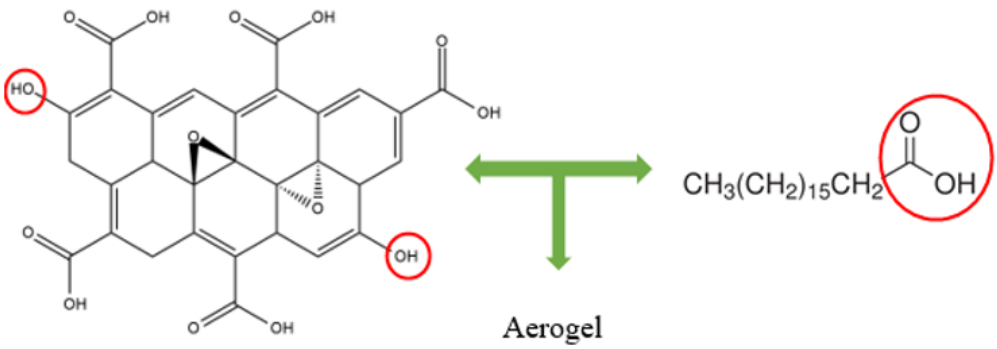

$$GO\text{-}OH + CH_3(CH_2)_{16}COOH \Rightarrow GO\text{-}O\text{-}\overset{\overset{O}{\|}}{C}(CH_2)_{16}CH_3 + H_2O$$

Figure 3.2 Schematic representation of GO and SA reaction to produce aerogels and the proposed reaction mechanism

3.2.3 Production of Graphene Oxide and (3-Aminopropyl) triethoxysilane Based Aerogels

Bare GO aerogels were prepared with the method mentioned earlier at 130 °C. The higher reaction temperature and further thermal reduction were avoided to preserve the hydrophilic character of the aerogels. After freeze-drying, resulting aerogels were

treated with APTES via vapor-phase deposition. Vapor-phase deposition of APTES was conducted inside a vacuum desiccator. Bare GO aerogels were placed in Petri dishes, and 100 μL APTES was injected in a small bottle cap. The desiccator was connected to a vacuum pump and evacuated for 30 min. Aerogels were left in vacuum overnight to provide enough time for APTES deposition and removed after 24 h. Aerogels were used for dye adsorption application after at least one day left at room temperature. Aerogels were denoted as GO-NH_2.

3.2.4 Oil Absorption Experiments

Aerogels were weighed before absorption and adsorption experiments. Then they were placed into bottles containing 15 mL chloroform and sunflower oil. After reaching equilibrium, gels were removed, and absorbate on the surface was removed by using paper towels. Gels were then weighed. The experiments were repeated two times, and the mean of 3 experimental data was reported. The absorption capacity of the aerogel was calculated using Equation 7.

$$Q_e = \frac{m_e - m}{m} \tag{7}$$

3.2.5 Dye Adsorption Experiments

Methylene blue (MB) and methyl orange (MO) were chosen as the model compounds for cationic and anionic dyes to investigate the produced aerogels' adsorption performance. Their structures are given in **Figure 3.3** and **Figure 3.4**.

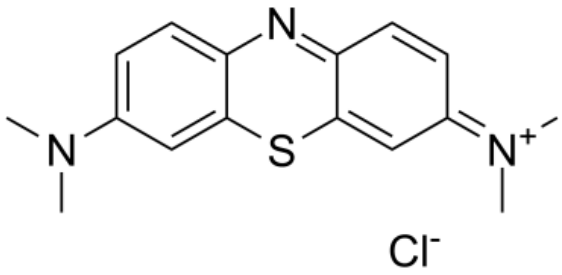

Figure 3.3 Chemical Structure Depiction of MB

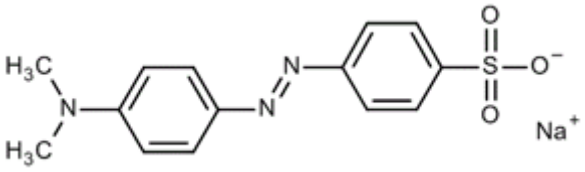

Figure 3.4 Chemical Structure Depiction of MO

For the accuracy of experimental data, a specific concentration of MB and MO stock solutions were prepared. The desired MB and MO concentration solutions were obtained from the diluted stock solutions. The standard calibration curves presented in **Figure C. 1** were plotted between absorbance and dye solutions concentration. The unknown dye concentration was calculated using the standard calibration curve and the measured absorbance value. For MB and MO solutions, the concentrations were calculated by the absorbance at 664 nm and 464 nm, respectively, in the UV-vis spectrum. Necessary dilution was performed in order to guarantee that the dye concentration was within the calibration curve range.

The kinetic experiments were performed with 10 mL MB (or MO) solution of concentration 100 ppm and pH of 7.8 ± 0.1 in the presence of GO-based aerogel (5.3 ± 0.1 mg) as the adsorbent in 50 mL bottles while varying contact time from 1 h to 108 h (or one h to 96 h). The bottles were placed in a water bath thermostatic oscillator shaker at 25.0 ± 1.0 °C and 120 rpm. To determine the adsorption kinetics, pseudo-first-order, pseudo-second-order, modified Freundlich, and intra-particle diffusion models were employed, given in Equation 6, 7, 8, and 9, respectively. For pseudo-first-order, k_1 and Q_e were determined from linear fittings of log ($Q_e - Q_t$) versus t where, $k_1 = -2.303 \cdot slope$ and $Q_e = 10^{intercept}$. For pseudo-second-order,

k_2 and Q_e were determined from the plot of t/Q_t versus t where, $k_2 = slope^2/intercept$ and $Q_e = 1/slope$. For modified Freundlich model, from the log (Q_t) versus log (t) plot, $m = 1/slope$ and $k = e^{intercept}/\ C_0$ were obtained. Finally, for the intra-particle diffusion model, Q_t versus $t^{1/2}$ was plotted, and k_i and C were obtained from the fitting as slope and intercept, respectively.

A range of MB (or MO) concentrations between 100 – 400 mg/L (or 10 – 100 mg/L) for isotherm study were examined at pH 7.8 ± 0.1. To investigate the adsorption mechanisms, Langmuir and Freundlich's models were employed to fit the adsorption isotherms. Linear expressions for the Langmuir and Freundlich equations are given in Equation 3 and 5, respectively. For Langmuir isotherm, K_L and Q_m are determined from the plot of C_e/Q_e versus C_e where $Q_m = -1/slope$ and $K_L = 1/(intercept * Q_m)$.

The initial pH effect was examined by varying the pH of 100 ppm MB and MO solutions between 2 and 12 using 1 M NaOH and HCl at 25.0 ± 1.0 °C. The adsorption kinetic curves determined the time required to achieve the equilibrium adsorption state.

The effect of temperature on the MB adsorption was examined for a range of MB concentrations between 40 – 400 mg/L at constant pH of 7.8 ± 0.1 and temperatures 25, 37.5, and 50 °C. The thermodynamic behavior was examined using Equation 10.

$$ln(K_0) = \frac{\Delta S^0}{R} - \frac{\Delta H^0}{RT} \quad (10)$$

Where ΔS^0 and ΔH^0 are the enthalpy change (kJ/mol) and entropy change (J/mol K), respectively, R and T are the universal gas constant (8.314 J/mol K) and absolute temperature (K). K_0 is the thermodynamic equilibrium constant which is defined as:

$$K_0 = \frac{Q_e}{C_e}\frac{v_s}{v_e} \quad (11)$$

Where v_s is defined as the adsorbate's activity coefficient and v_e is the activity coefficient of adsorbate in solution. Their ratio (vs/ve) can be assumed to be constant

in the dilute solutions[127]. As the dye concentration in the solution reaches 0, the activity coefficient ratio is nearly constant, and the limit of Q_e/C_e approaches to K_0. Therefore K_0 values were obtained from the plot of ln(Qe/Ce) versus Qe where $K_0 = intercept.$

The experiments were repeated two times, and the mean of 3 experimental data was reported. Adsorption capacities of the aerogels were calculated using Equation 12.

$$Q_t = \frac{(C_0 - C_t)}{m} V \tag{12}$$

Where C_t is the dye concentration at time t. Blank adsorption experiments were conducted without adsorbent addition to secure the accuracy of experiments. MB and MO removal efficiency (R) was also calculated at the same time, according to Equation 13.

$$R = \frac{C_0 - C_e}{C_0} 100\% \tag{13}$$

3.2.6 Aerogel Regeneration

To evaluate the recycling ability of the produced aerogels, after chloroform absorption experiments, aerogels were left in room conditions to evaporate chloroform. After 3 hours, when the dry weights of aerogels stabilized, the absorption experiment was repeated. For the dye adsorption experiments, desorption was performed for adsorbate-loaded aerogel using ethanol. Then the aerogel was washed with ethanol-water mixtures, and finally, water and then freeze-dried, and the adsorption process was repeated.

3.3 Characterizations

3.3.1 Thermogravimetric Analysis (TGA)

Solid samples were prepared, and analyses were conducted from room temperature to 600 °C with a heating rate of 10 °C/min in a nitrogen environment. Shimadzu DTG-60H was used for analyses.

3.3.2 Scanning Electron Microscopy (SEM)

Aerogels were analyzed with TESCAN VEGA3 SEM using an acceleration voltage of 30 kV. Samples were placed onto holders and coated with gold-palladium using LEICA EM ACE200 sputter coater before imaging.

3.3.3 Attenuated Total Reflectance-Fourier Transform Infrared Spectroscopy (ATR-FTIR)

All of the analyses were performed using Shimadzu IRPrestige-21 spectrophotometer in the wavenumber range of 500-4000 cm^{-1} with 64 scans. Solid samples were used for the analysis.

3.3.4 Ultraviolet-visible Spectroscopy (UV-Vis)

The analysis was conducted for graphene oxide using Shimadzu UV-2550 in a wavelength range of 200-800 nm for GO characterizations. GO was dispersed in water with a concentration of 1 mg/mL Wavelength range of 300-700 nm was employed for MB and MO adsorption experiments.

CHAPTER 4

RESULTS AND DISCUSSION

Two paths were proposed in order to develop GO-based aerogels for pollutant removal. For the first path, thermal reduction and stearic acid addition to the structure were employed to decrease the hydrophilicity and increase the oleophilicity of the aerogels, respectively. GO and stearic acid were mixed in desired amounts and incubated for five hours at 145 °C to form organogels. After washing and freeze-drying, aerogels were thermally treated for four hours at 150 °C to obtain reduced GO-based aerogels. Chloroform and sunflower oil were used to evaluate the oil absorption capacity of the prepared aerogels. For the second path, bare GO aerogels and (3-Aminopropyl) triethoxysilane (APTES) deposited GO aerogels were produced. APTES deposition was performed, aiming to increase the adsorption capacity of the aerogel for anionic dyes. For the bare GO aerogels, GO dispersions were incubated for five hours at 130 °C to form organogels. After washing and freeze-drying, aerogels were obtained, and they were used in dye adsorption experiments as prepared. For APTES deposited GO aerogels, the previously mentioned method for bare GO aerogel production was employed and followed with APTES deposition at room temperature overnight. Aerogels were left it room temperature at least one day before dye adsorption experiments. The prepared aerogels' dye removal performance was investigated for methylene blue (MB) and methyl orange (MO) as the model compounds.

4.1 Graphene Oxide Synthesis

Intercalation and oxidation are crucial while converting graphite to GO. In GO synthesis acid mixture of H_2SO_4 and H_3PO_4 is employed to increase the graphene layer spacing so that the oxidizing agent $KMnO_4$ can oxidize graphite. H_3PO_4, as the

second acid, is essential to secure the structure of carboxylic acid rings[128] and prevent excessive oxidation[129]. As can be seen from **Figure 4.1**, the reaction mixture experiences several color changes throughout the reaction. Firstly, after the addition of acid mixture, Mn_2O_7 is formed, and a dark-green color is observed. After 12 h of reaction at 50 °C, the reaction mixture's color becomes brownish-purple due to excess $KMnO_4$ in the reaction mixture. The addition of H_2O_2 removes the excess $KMnO_4$, and the reaction mixture turns into a bright yellow color. After H_2O_2 addition, the reaction mixture must be washed thoroughly to remove the risk of graphene oxide contamination due to excess permanganate ions[130].

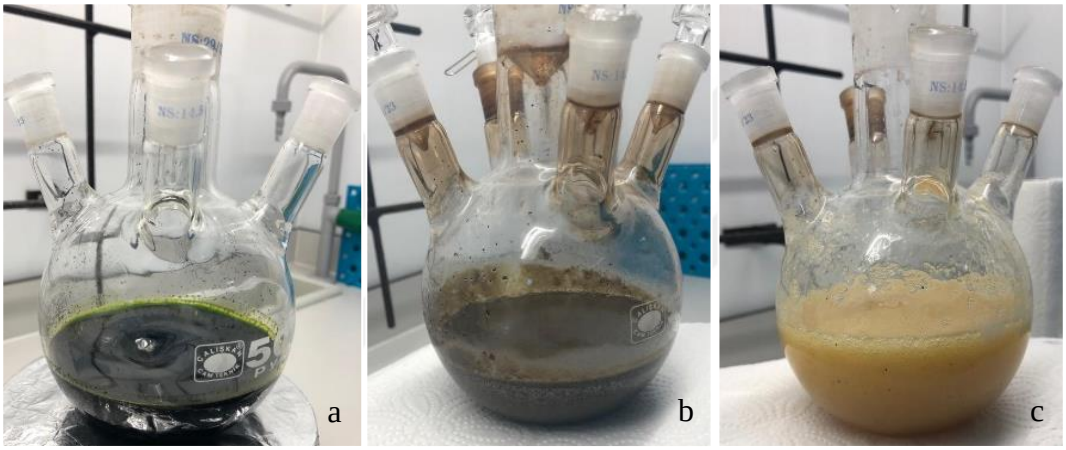

Figure 4.1 Photographs showing the changes of the reaction mixture during the GO synthesis (initial reaction mixture (a), after 12 h (b), after ice and H_2O_2 addition (c))

ATR-FTIR analysis is a potent tool to investigate the functional groups in a molecule by differentiating the bonds based on their different absorption frequencies. For this reason, it was employed to confirm the oxidation of graphite. In **Figure 4.2,** FTIR analysis results of graphite and GO are given. This figure demonstrates the oxygen-containing functional groups of GO. As a result of oxidation of graphite, –OH stretch peak at 3159.21 cm^{-1}, C=O peak at 1693.66 cm^{-1}, C-O-C peak at 1225.09 $cm^{-1,}$ and finally, C-OH stretch peak at 991.75 cm^{-1} was observed.

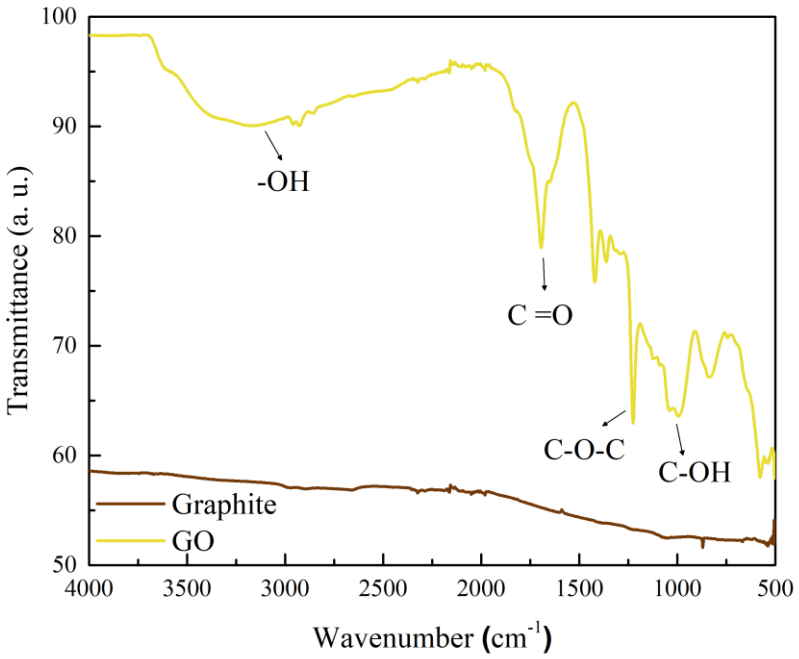

Figure 4.2 ATR-FTIR Analysis of Graphite and GO

A comparison of the experimental data with previously reported literature values can be seen in **Table 4.1**.

Table 4.1 ATR-FTIR peak positions (in cm^{-1}) of GO from literature and experimental data

Functional Group	Wavenumber (Literature values[7])	Wavenumber (Experimental values)
O-H streching vibrations	2500-3600	3159
C=O streching vibrations	1720-1750	1694
C=C from unoxidized sp^2 carbon to carbon bonds	1400-1680	1419
C-O vibrations	1050-1250	1225

Thermal gravimetric analysis is a useful method to analyze the thermal stability of a material. In general, TGA is used to determine the weight loss due to decomposition or oxidation. TGA results of graphite and GO were interpreted to observe weight loss as a function of increasing temperature. The resulting graphs are given in **Figure 4.3**. For GO, significant weight loss was observed between 100 and 200 ºC due to CO, CO_2, and steam release from unstable functional groups. The weight loss observed before 100 °C was due to the humidity present in the sample. For temperatures below 600 ºC, total weight loss for GO was about 60%. In contrast, graphite showed very high thermal stability, losing only 0.40% of its total weight for temperatures below 600 ºC.

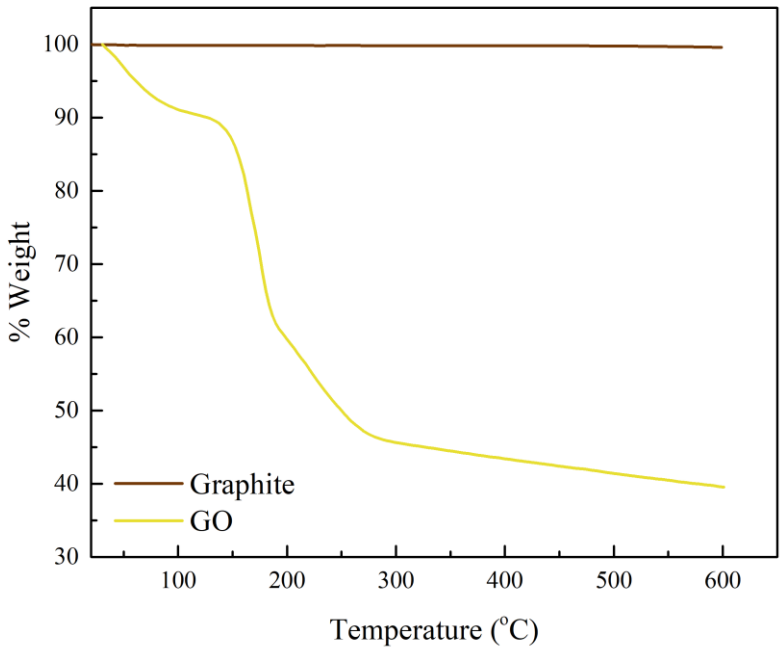

Figure 4.3 TGA Results of Graphite and GO

Ultraviolet spectrophotometry can be used to determine the concentration of molecules in solution or identify a component by using the absorption of light in the visible or ultraviolet region. UV/vis analysis results of graphene oxide are given in **Figure 4.4**. Around 210 nm graphene oxide has the maximum absorbance due to $\pi \rightarrow \pi^*$ transitions, consistent with previously reported results[44]. Moreover, around

300 nm graphene oxide exhibited shoulder due to n→π* transitions of the carbonyl groups[44].

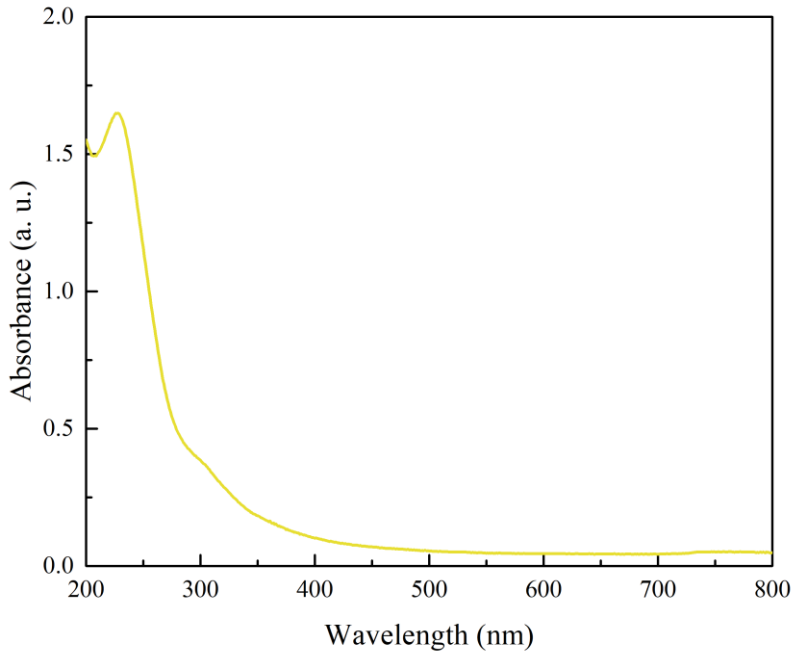

Figure 4.4 UV-vis Analysis Result of GO

Morphology of synthesized GO was examined via SEM images given in **Figure 4.5**. From the SEM image, it can be seen that GO sheets have a broad size range.

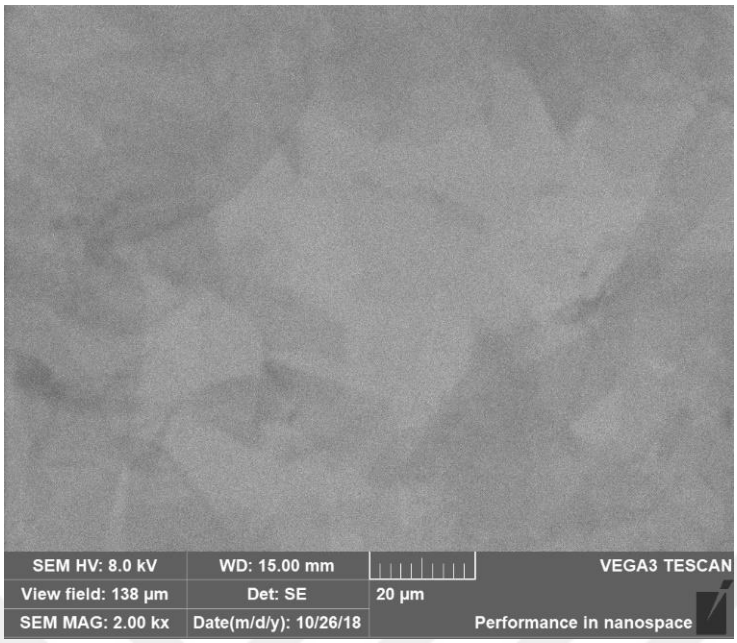

Figure 4.5 SEM image of GO

4.2 Reduced Graphene Oxide Based Aerogels

The ATR-FTIR spectra of rGO/SA aerogels shown in **Figure 4.6** exhibits both the characteristic peaks of stearic acid and GO. The O-H stretching vibration can be observed in the broad bands around 3000 cm^{-1}. The peaks around 2910 cm^{-1} and 2860 cm^{-1} are due to the stretching vibrations of $-CH_3$ and $-CH_2$. At the same time, the peak around 1240 cm^{-1} may be due to C-O vibrations[131]. C=O stretching vibration observed around 1740 cm^{-1} for SGAs was much less intense than pure stearic acid (1660 cm^{-1}). Frequency shifts of the main groups of rGO/SA are likely due to interface interactions between the carboxylic acid group of SA and the GO's hydroxyl groups.

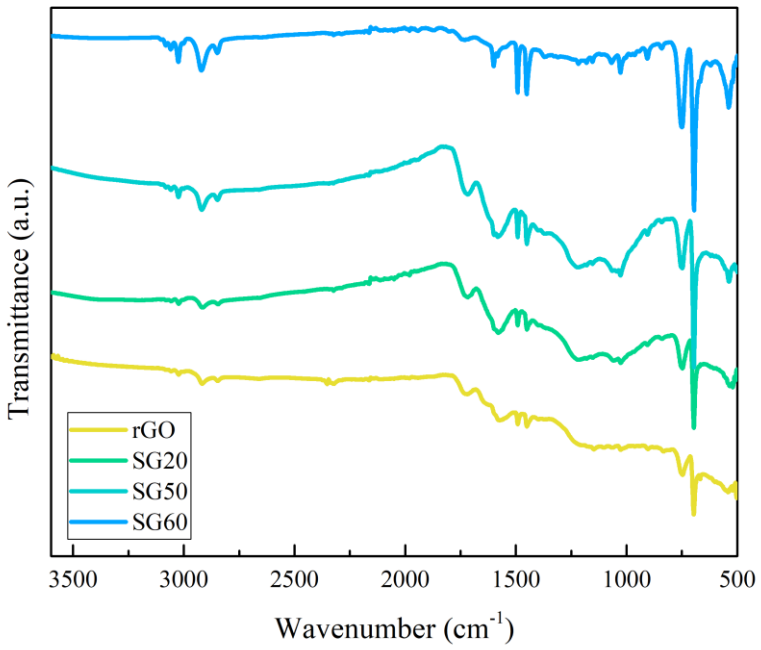

Figure 4.6 ATR-FTIR Analysis of rGO/SA aerogels

TGA curves for GO based aerogels and stearic is given in **Figure 4.7**. For rGO aerogel, three stages can be observed for weight loss. The first stage is the 15% weight loss below 100 °C, due to the sample's moisture content. The second stage is approximately 30% weight loss between 200 °C and 300 °C and due to the reduction of oxygen-containing functional groups. On the other hand, weight loss for SA starts at about 200 °C, and at 450 °C SA is wholly decomposed. The TGA curve of the rGO/SA aerogel follows a similar weight loss trend. Under 100 °C, weight loss occurs due to the evaporation of moisture. Majority of the weight loss at temperatures of 100–250 °C is due to the removal of SA in rGO/SA aerogel. After incorporating stearic acid, aerogel's decomposition temperature shifted to the right, which implies better thermal properties[132].

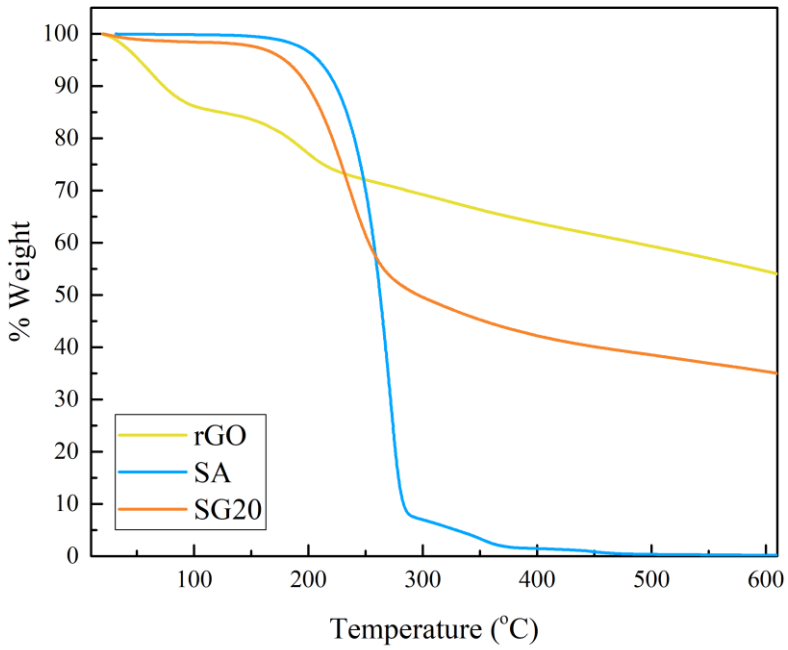

Figure 4.7 TGA Results of rGO/SA aerogels and pure SA

4.2.1 Absorption Performance of Reduced Graphene Oxide Based Aerogels

Comparisons of chloroform and sunflower oil absorption capacities of the produced aerogels can be seen in **Figure 4.8.** After observing the swollen mass change of the aerogels, 2.5 hours was selected as the absorption time. As can be seen from the figure, with increasing SA content, the aerogels' oil absorption capacities decreased. SA was incorporated into the aerogel structure, aiming to increase its oleophilic property; however, the opposite was observed. This might due to that stearic acid bonded to sites where oil molecules are absorbed. SA might have formed strong interactions with GO, which lowered the porosity of the aerogels.

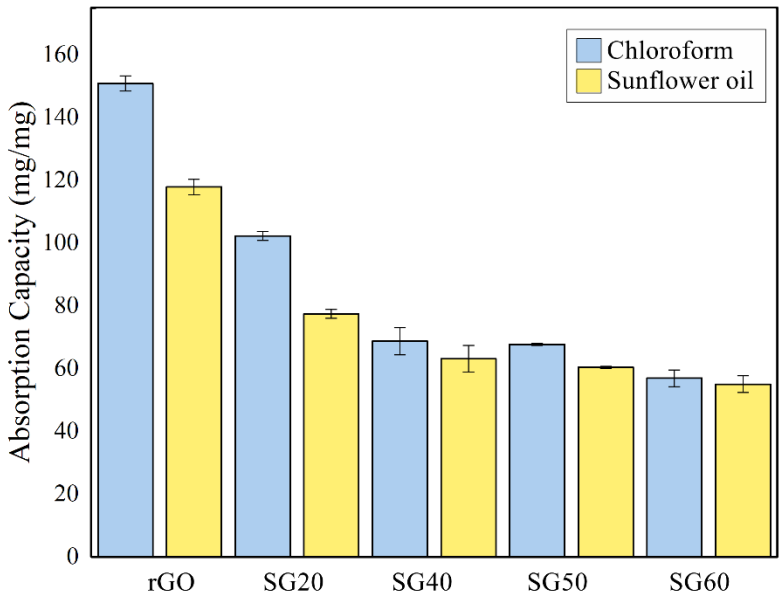

Figure 4.8 Absorption capacities of rGO and rGO/SA aerogels

The absorbent regeneration is an important issue that can reduce the operating costs and hence should be evaluated. After the absorption tests, aerogels were removed from chloroform, and after the chloroform in the aerogel structure completely evaporated, absorption tests were repeated. During the regeneration studies, rGO aerogels were very brittle, while rGO/SA aerogels exhibited no shape change even after the 15th cycle. As shown in **Figure 4.9**, rGO/SA aerogels could be recycled and reused at least 15 times without losing much of their absorption capacity. The sharp decrease of the absorption capacity of rGO aerogel is likely due to a collapse in its structure after chloroform evaporates.

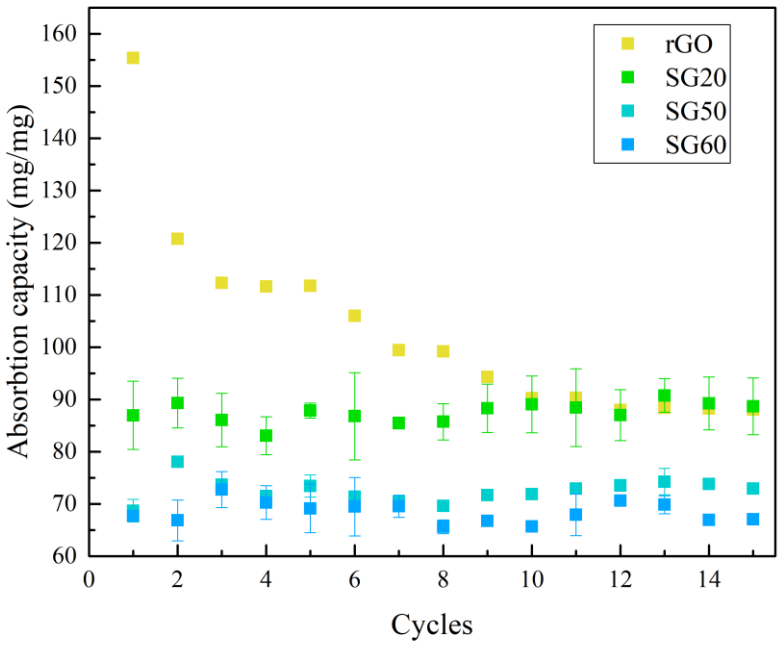

Figure 4.9 Recyclability of rGO and rGO/SA aerogels for chloroform absorption

4.2.2 Structure Analysis of Reduced Graphene Oxide and Stearic Acid Based Aerogels

In **Figure 4.10**, SEM images for rGO/SA aerogels with weight ratios 20%, 50% and 60% are provided. While SG20 showed an open pore structure with interconnections, in SG50, aerogel closed pores were observed. While the addition of SA increased the aerogels' mechanical performance, further increasing the SA inhibited the pore formation and led to a dense and compact structure, as can be seen from the SEM image of SG60. The open-pore structure is crucial for oil absorption[77]. As a result, SG20 exhibited better chloroform and sunflower absorption capacity than SG50 and SG60.

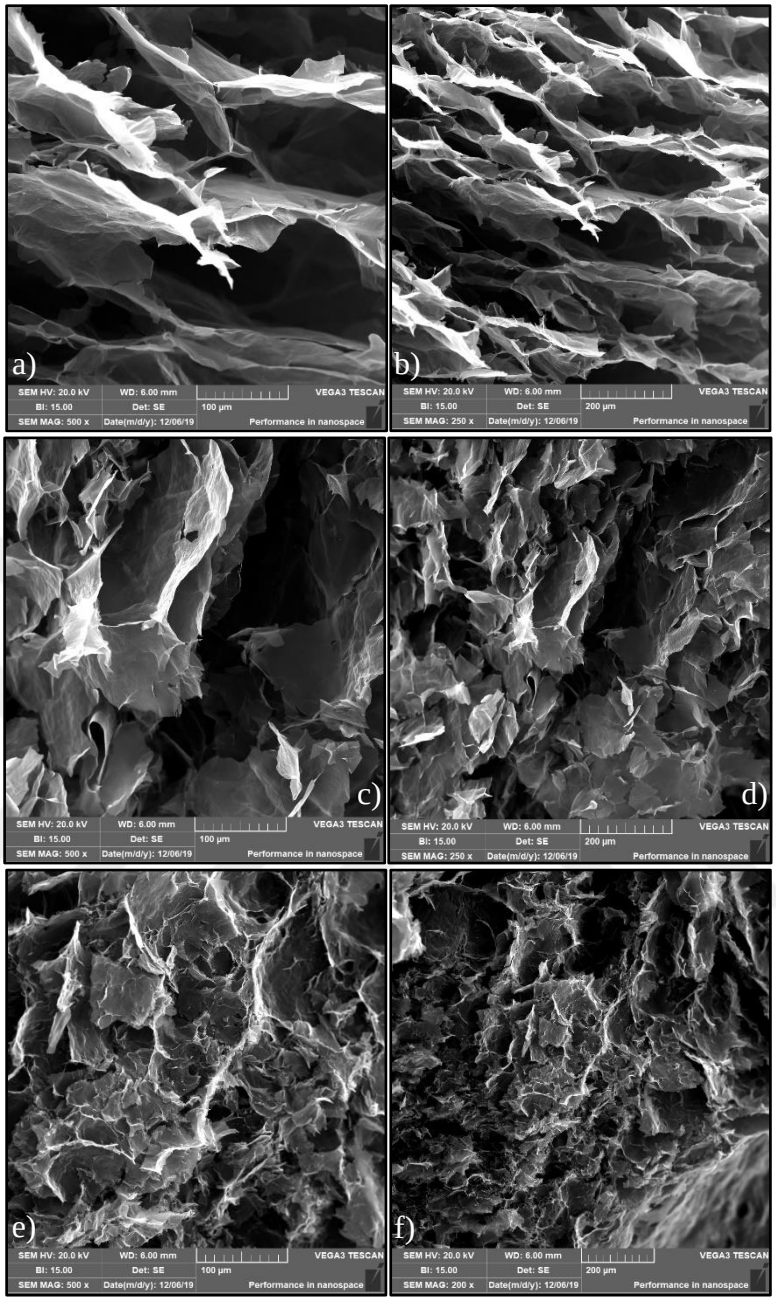

Figure 4.10 SEM images of rGO/SA aerogels, SG20 (a,b), SG50 (c,d) and SG60 (e,f)

4.3 Graphene Oxide Based Aerogels

ATR-FTIR spectra for the produced GO and APTES functionalized GO aerogels are given in **Figure 4.11**. New bands were observed at 1024 and 676 cm^{-1} after the functionalization of GO with APTES. These new bands are due to the Si–O–C bands between GO and APTES[133]. Moreover, the existence and overlap of Si–H and NH_2 vibrations bands at 810 cm^{-1} validate the chemical functionalization of GO with APTES[134]. Moreover, the location of vibration bands of GO, including C–OH (at 3420 cm^{-1}), C=C (at 1590 cm^{-1}), and C–O (at 1257 cm^{-1}), shifted slightly, and the intensity of these peaks became sharper as a result of the overlapping of the C–OH, C=C, and C–O bands with N–H, NH_2, and C–N vibration bands, respectively[133].

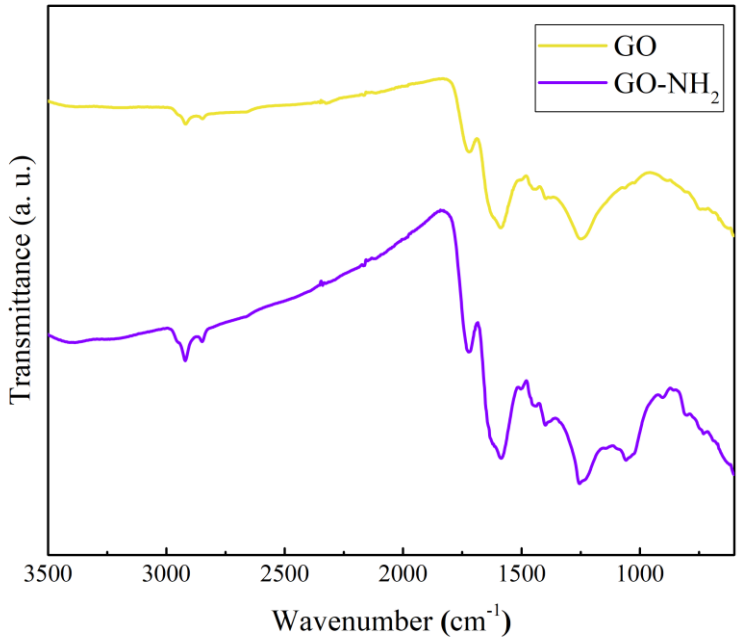

Figure 4.11 FTIR spectra of GO and GO-NH_2 aerogels

4.3.1 Adsorption Performance of Graphene Oxide Based Aerogels toward Dyestuff

The batch adsorption studies were conducted to evaluate GO and GO-NH_2 aerogels' performance for dyestuff removal from aqueous solutions. For GO aerogel, adsorption kinetics and isotherms for MB and MO were investigated. Moreover, the effect of initial solution pH and temperature on the adsorption of MB were investigated. For GO-NH_2 aerogel, adsorption isotherm for MO was investigated.

4.3.1.1 Adsorption of Dyestuff onto Bare Graphene Oxide Aerogels

4.3.1.1.1 Effect of Contacting Time on Adsorption of Dyestuff

Adsorption of MB and MO onto GO-based aerogels is governed by a mix of electrostatic forces and π–π interactions. Adsorption kinetic tests were performed to determine the adsorption rates of MB and MO on the GO aerogels. The relationship between the contact time and adsorbed amount of MB and MO on aerogels are portrayed in **Figure 4.12** and **Figure 4.13**, respectively. For both MB and MO, adsorption capacity increased moderately with increasing contact time.

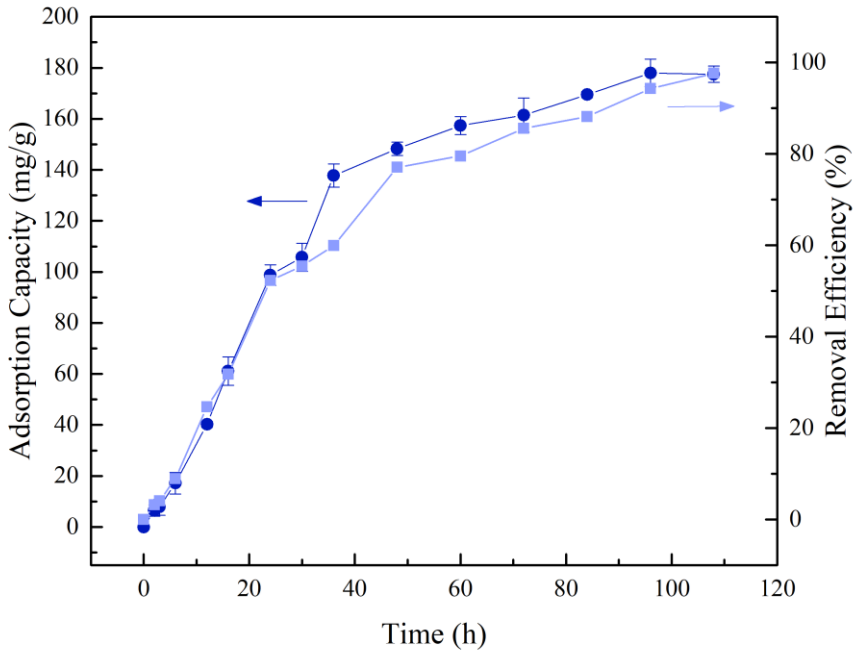

Figure 4.12 Change of adsorbed amount (Q_t, mg/g) of MB and removal efficiency (R%) with increasing adsorption time at 298 K and pH=7.8. Data represent mean ± SD (n = 3)

MB adsorption on GO aerogels reached equilibrium after 96 h since by applying Duncan multiple comparisons method, it was concluded that there was no statistically significant change between 96 h and 108 h. On the other hand, for MO time needed to reach the adsorption equilibrium was observed as 48 h. This is reasonable since the adsorption capacity at equilibrium for MB (178.0 mg/g) is more significant than that of MO (85.1 mg/g). As reflected by the more significant initial slope of MB adsorption kinetic, MB's adsorption rate on GO aerogels is faster than that of MO. However, aerogels showed slower kinetics for both of the dyes than other adsorbents[104–106,111] due to the low diffusion of adsorbate molecules into the aerogels. Vigorous mixing of the solution or reducing the size of aerogels could accelerate the diffusion.

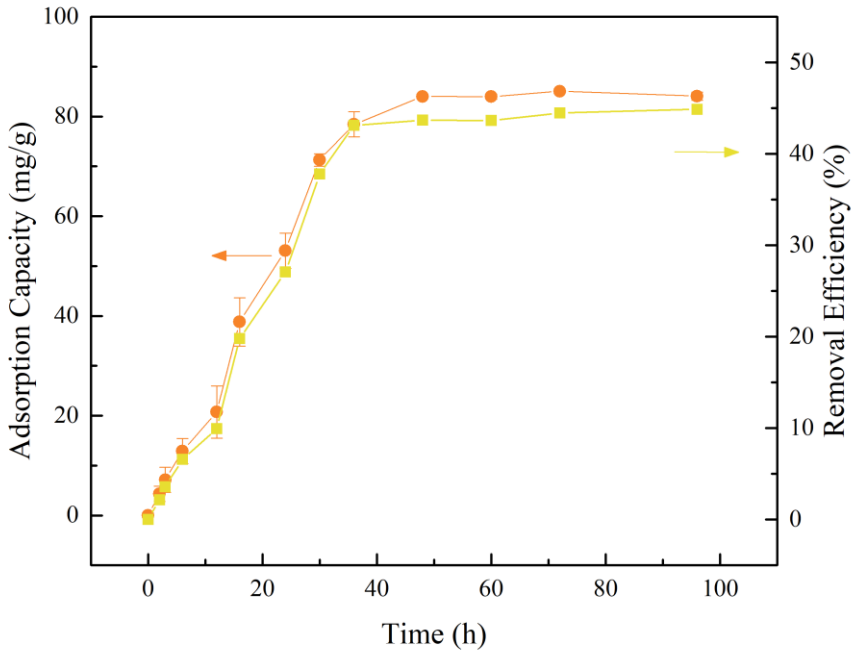

Figure 4.13 Change of adsorbed amount (Qt, mg/g) of MO and removal efficiency (R%) with increasing adsorption time at 298 K and pH=7.8. Data represent mean ± SD (n = 3)

MB's adsorption process on GO aerogels could be well described by the pseudo-first-order model (R^2=0.987) with a k_1 value of 1.159×10^{-4} min^{-1}. For MO, the adsorption process can be described by the modified Freundlich model with a K value of 4.288×10^{-4} $L \cdot g^{-1} \cdot min^{-1}$ and R^2 of 0.988. For the pseudo-first-order model, the calculated Q_e values were 191 mg/g and 143 mg/g for MB and MO, which were higher than the experimental Q_e values (178.0 mg/g and 85.1 mg/g). For the pseudo-second-order model, both dyes showed poor fits. The R^2 values were calculated as 0.693 and 0.799, and the calculated Q_e values were 382 mg/g and 234 mg/g for MB and MO, respectively. The corresponding k_2 were 4.422×10^{-7} mg/(g·min) and 7.675×10^{-7} mg/(g·min). Corresponding fits are given in **Figure 4.14**, **Figure 4.15**, and **Figure 4.16**.

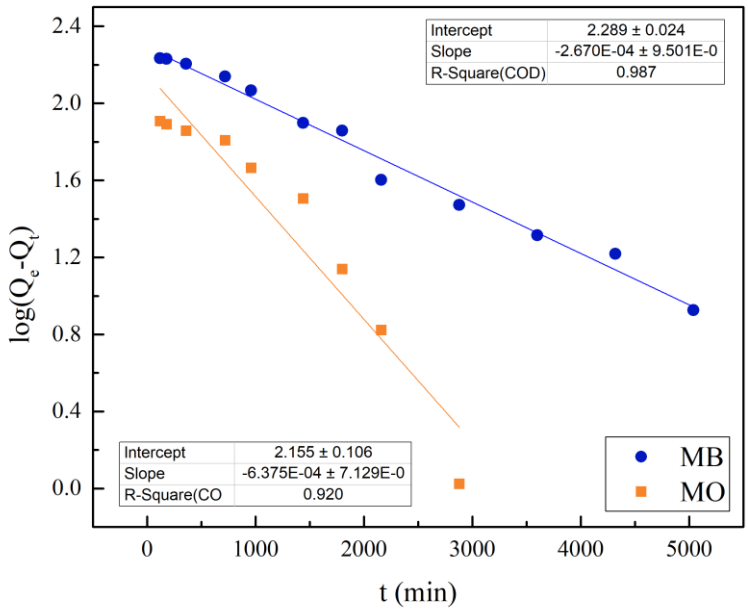

Figure 4.14 The pseudo-first-order model for batch adsorptions of MB and MO at 298 K and pH=7.8

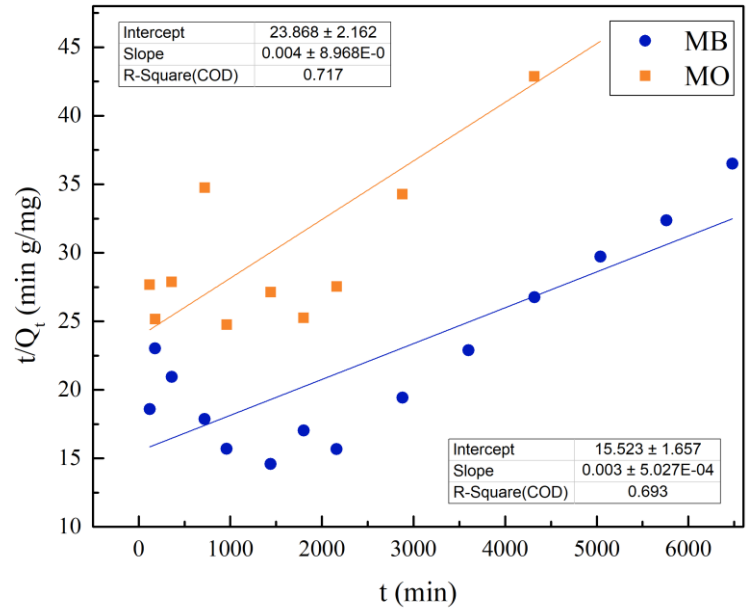

Figure 4.15 The pseudo-second-order model for batch adsorptions of MB and MO at 298 K and pH=7.8

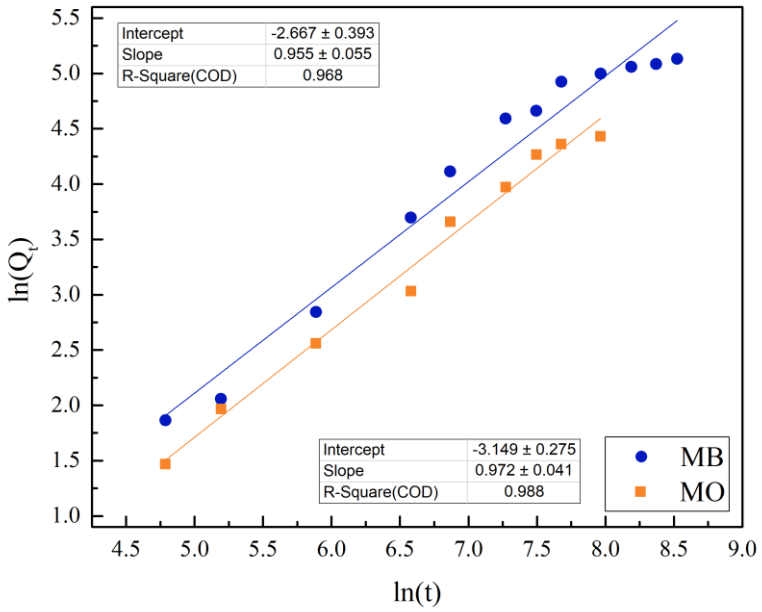

Figure 4.16 The Modified Freundlich model for batch adsorptions of MB and MO at 298 K and pH=7.8

Pseudo-first-order, pseudo-second-order and modified Freundlich models were employed to understand the adsorption process. At the same time, the intraparticle diffusion model was utilized for the investigation of the diffusion mechanism. As shown in **Figure 4.17**, MB and MO's adsorption process can be separated into three stages. The fitted lines in stage I and stage II corresponds to boundary layer diffusion and intra-particle diffusion influence on the adsorption mechanism respectively[118]. The final stages correspond to near equilibrium[99]. For both MB and MO, the majority of the adsorption capacity was achieved within the first 36 hours, in stage II.

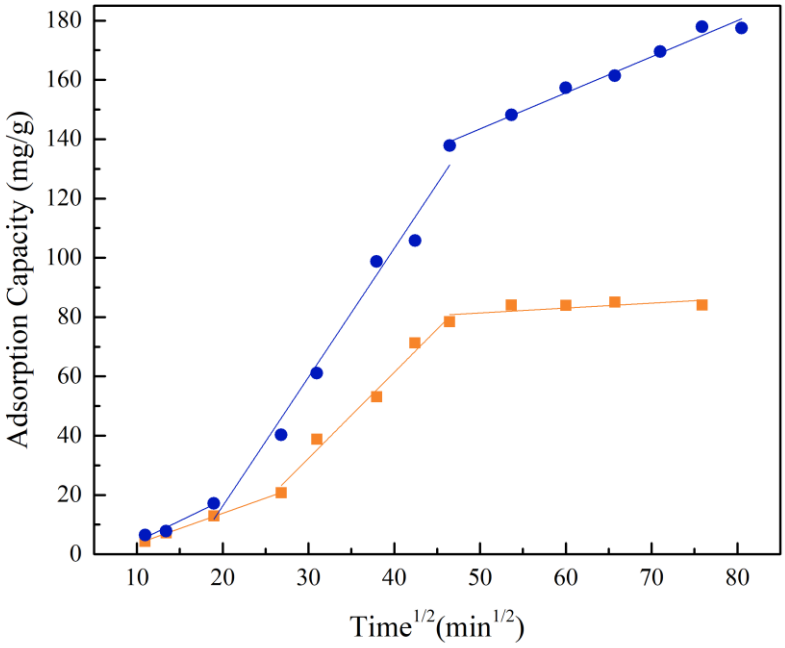

Figure 4.17 The intra-particle model for batch adsorptions of MB and MO at 298 K and pH=7.8

Examination of the slopes of steps can reveal the rate of adsorption. From **Table 4.2**, it can be seen that MB molecules can diffuse faster into the external surface than MO, which can be explained by the electrostatic repulsion between MO molecules and carboxylic acid and hydroxyl groups on the aerogel surface. Moreover, intra-particle diffusion is the fastest stage for both dyes.

Table 4.2 Intraparticle diffusion parameters for the adsorption of MB and MO

Dye	Stage I		Stage II	
	k_1	R_1^2	k_2	R_2^2
MB	1.398	0.9663	4.346	0.9808
MO	1.027	0.9995	2.902	0.9653

4.3.1.1.2 Effect of Initial Solution pH on Adsorption of Dyestuff

Solution pH is a crucial factor affecting cationic or anionic dyes since it can remarkably influence the surface charge of adsorbents and dissociation of surface functional groups[71]. An appropriate adsorbent should be able to perform in severe environmental conditions. At lower solution pH, H^+ ions compete with cationic dyes for adsorption sites, and protonation of hydroxyl and carboxyl groups causes electrostatic repulsion between cationic dyes and aerogel surface, which creates a decrease in adsorption capacity[71]. As pH increases, carboxyl and hydroxy groups on GO aerogel's surface become more deprotonated to generate negative charges, increasing MB adsorption. The effect of initial solution pH on MB and MO can be seen in **Figure 4.18**.

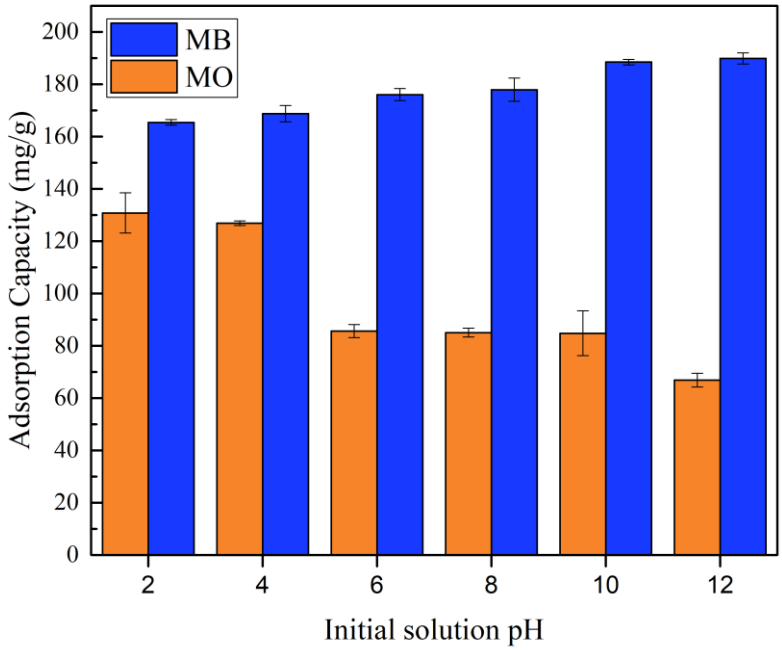

Figure 4.18 Effect of initial pH on MB and MO adsorption at 298 K. Data represent mean ± SD (n = 3)

As shown in **Figure 4.18**, MB adsorption by GOA increased with increasing pH as expected. However, the increase in adsorption capacity was not significant. For

example, when the solution pH varied from 2.0 to 12.0, adsorption capacity only increased by 15%. The slight change in GO aerogel's adsorption capacity for MB in a wide range of pH can hint that π-π interaction between MB molecules and GO aerogel is the interaction controlling the MB adsorption. As a result, MB removal could be performed successfully at a wide pH range. On the other hand, pH difference significantly affected MO adsorption. From pH of 12.0 to 2.0 adsorption capacity of GO aerogel almost doubled (66.8 mg/g at pH=12.0 and 130.9 mg/g at pH=2.0). Unlike MB adsorption, the effect of electrostatic interactions on MO adsorption was observed much prominently. UV-vis spectra for MB and MO solutions after adsorption by GO aerogels at different pH values are given in **Figure B. 1**.

4.3.1.1.3 Effect of Temperature on Adsorption of Methylene Blue

Temperature is an essential parameter in the adsorption process since it can change the adsorbent's adsorption capacity. **Figure 4.19** represents the adsorption isotherms for MB at 298, 311 and 323 K. The plot shows the effect of concentration and temperature on GO aerogel's adsorption behavior. As expected, Q_e increases with increasing MB concentration. Moreover, higher temperatures facilities the MB adsorption on GO aerogel, which hints that MB adsorption is an endothermic process. The adsorption capacity of GO aerogel increased from 539 mg/g to 803 mg/g when temperature increased by 25 K for an initial MB concentration of 400 ppm. This may be due to an increase in the number of active sites for the adsorption with increasing temperature[135] or a possible swelling effect, which might have enlarged the pores.

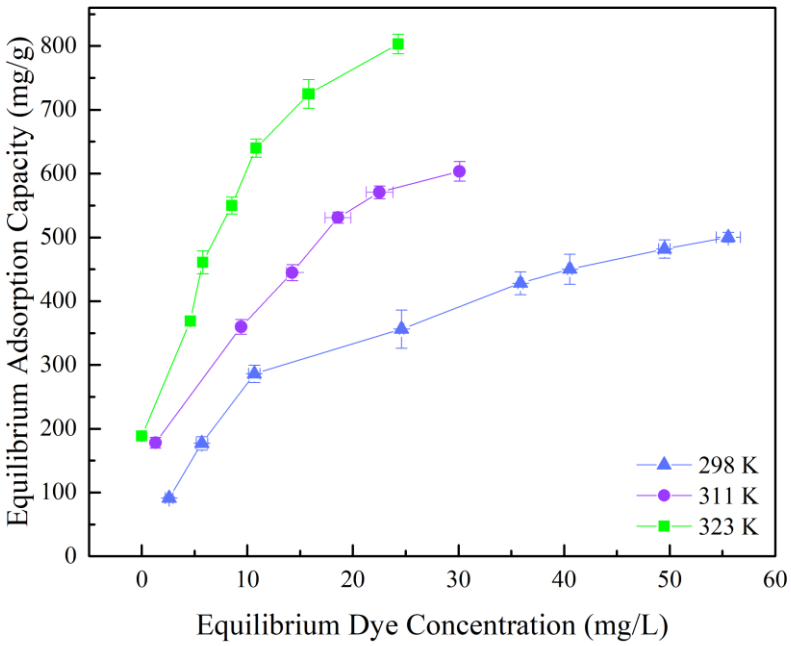

Figure 4.19 Effect of MB concentration and temperature at pH=7.8. Data represent mean ± SD (n = 3)

Corresponding Langmuir and Freundlich simulation plots are shown in **Figure 4.20** and **Figure 4.21**. For all of the solution temperatures, the Langmuir adsorption model gives higher R^2 than the Freundlich adsorption model. This is expected since, at higher oxidation degrees, GO aerogel exhibits monolayer adsorption via electrostatic interactions with MB[100]. Moreover, as seen from **Table 4.3**, with increasing temperature, K_L values for MB adsorption also increased, which indicates that the interaction between MB and the surface of GO aerogels was stronger at higher temperature[93].

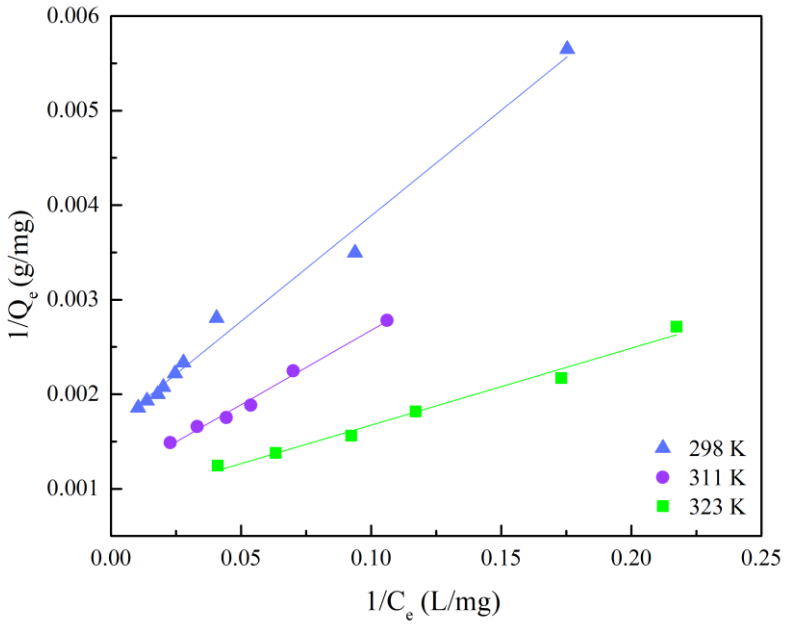

Figure 4.20 Langmuir isothermal adsorption models at pH=7.8

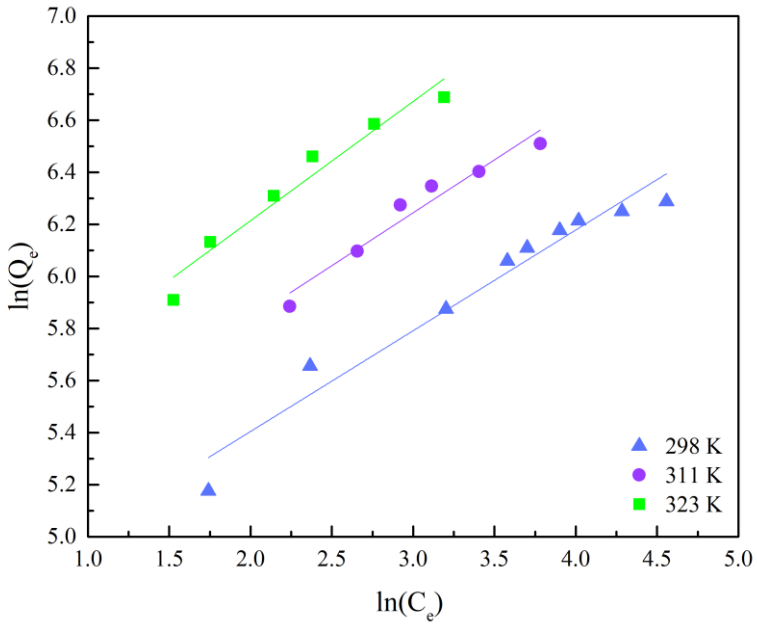

Figure 4.21 Freundlich isothermal adsorption models at pH=7.8

Table 4.3 Adsorption isotherm parameters for MB by GO Aerogel

Temperature (K)	Langmuir Adsorption Model			Freundlich Adsorption Model		
	Q_m (mg/g)	K_L (L/mg)	R^2	K_F (L/mg)	n	R^2
298	588.2	0.076	0.988	102.6	2.584	0.955
311	909.1	0.070	0.991	152.2	2.461	0.952
323	1111.0	0.111	0.986	200.1	2.184	0.952

The thermodynamic study can provide insight into inherent energy changes regarding the adsorption process. Moreover, information about the feasibility of the adsorption process can be obtained. Therefore, the thermodynamic behavior was observed, and the calculated thermodynamic parameters are provided in **Table 4.4**.

Table 4.4 Thermodynamic parameters of MB adsorption by GO Aerogel

Temperature (K)	ΔG^0 (kJ/mol)	ΔH^0 (kJ/mol)	ΔS^0 (J/mol K)
298	-3.520	7.65	37.5
311	-3.988	7.65	37.5
323	-4.456	7.65	37.5

From the table, it can be seen that for all temperatures, ΔG^0 is negative, which indicates that MB adsorption by GO aerogel is a spontaneous process. Furthermore, the adsorption is more available at higher solution temperatures. Positive ΔH^0 and ΔS^0 values indicate that the adsorption process is slightly endothermic and randomness on the solid/solution surface[136].

4.3.1.1.4 Reusability Study

Recycling and regeneration experiments were conducted since the reusability of adsorbents is very crucial for practical applications. For this purpose, desorption experiments were carried out in ethanol. Ten consecutive adsorption cycles were performed under the same conditions. As shown in **Figure 4.22**, GO aerogels could

be reused at least ten times for MB removal, with a more than 90.2% removal rate. This result indicates that GO aerogel is a promising adsorbent with excellent regeneration for MB adsorption from aqueous solutions.

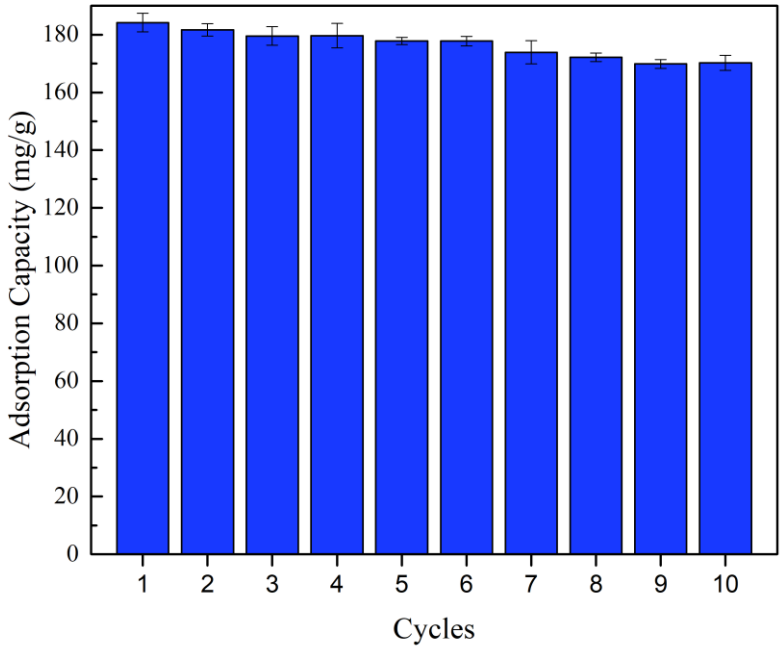

Figure 4.22 Recyclability of GO aerogel for MB adsorption at 298 K, pH=7.8 and initial dye concentration of 100 ppm. Data represent mean ± SD (*n* = 3)

Compared with the literature values of various aerogels presented in **Table 4.5**, produced bare GO aerogels are better alternatives than most of them in terms of adsorption capacity, availability and reusability performance.

Table 4.5 Comparison of various aerogels for MB adsorption

Adsorbent	Maximum Adsorption Capacity	Reusability Performance	Ref.
GO/Melamine Aerogel	286.5 mg/g	2% loss in removal efficiency after 10 cycles	[104]
CS/GO/Carboxymethyl Cellulose Aerogel Globules	3824 mg/g	50% loss in adsorption capacity after 5 cycles	[111]
Sodium Alginate/GO Aerogel	833.3 mg/g	N/A	[112]
CS/p(MA)/GO Aerogel	2478 mg/g	N/A	[106]
CS/GO Aerogel	275.5 mg/g	25% loss in removal efficiency after 4 cycles	[113]
Polyacrylamide/GO Aerogel	292.8 mg/g	N/A	[114]
CS/GO Microspheres	584.6 mg/g	15% loss in adsorption capacity after 6 cycles	[115]
Proanthocyanidin/GO Aerogel	460.8 mg/g	N/A	[117]
Silk Fibroin/GO Aerogel	1322.7 mg/g	N/A	[118]

4.3.1.2 Adsorption of Methyl Orange onto Graphene Oxide Based Aerogels

The effect of initial dye concentration for MO adsorption on GO and GO-NH_2 aerogels was observed for initial MO concentration ranging from 10 to 100 ppm. **Figure 4.23** represents the adsorption isotherms for MO at 298 K and pH=7.8. The plot describes the relationship between aerogels' adsorption capacities and the equilibrium concentration of dye in the solution. For both GO and GO-NH_2 aerogels, adsorption capacity increased dramatically in the first stage due to the improved driving force deriving from the concentration gradient[2]. The adsorption capacity of

GO and GO-NH_2 for MO increased from 14.3 mg/g to 85.1 mg/g and from 18.9 mg/g to 110.3 mg/g, respectively, as the initial concentration increased from 10 to 100 ppm. For 100 ppm initial MO concentration, GO-NH_2 exhibited approximately 30% higher adsorption capacity than GO aerogel.

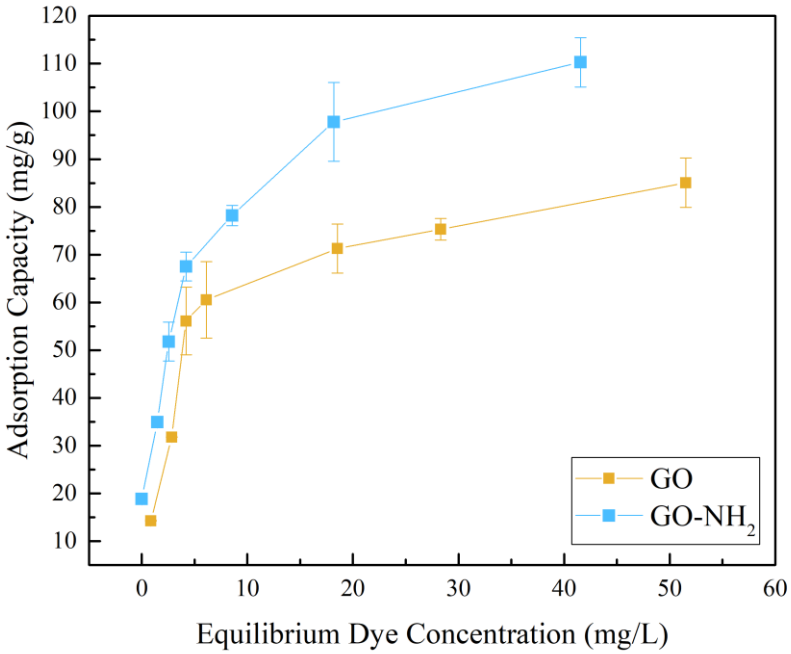

Figure 4.23 Adsorption isotherm of MO at 298 K and pH=7.8 Data represent mean ± SD (n = 3)

Langmuir and Freundlich isotherm models were applied to investigate the adsorption data. Respective plots can be seen in **Figure 4.24** and **Figure 4.25**.

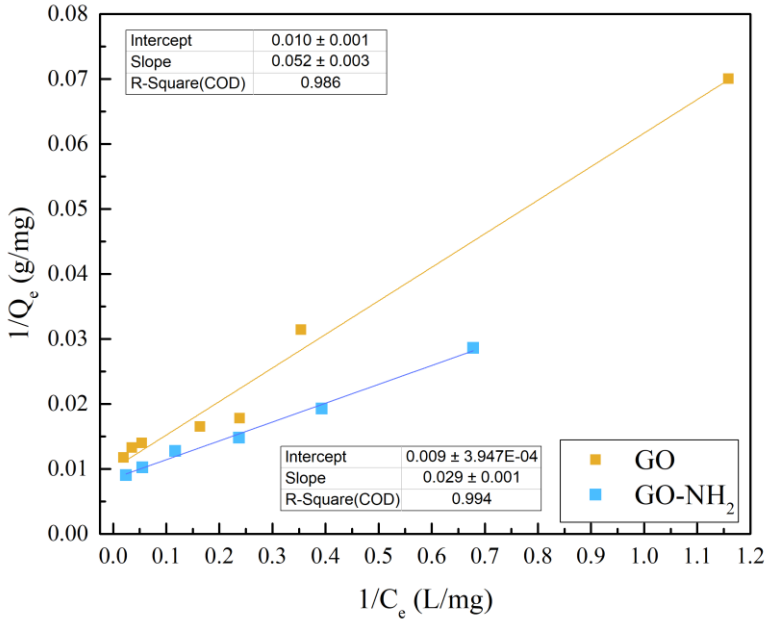

Figure 4.24 Langmuir adsorption isotherm of MO at 298 K and pH=7.8

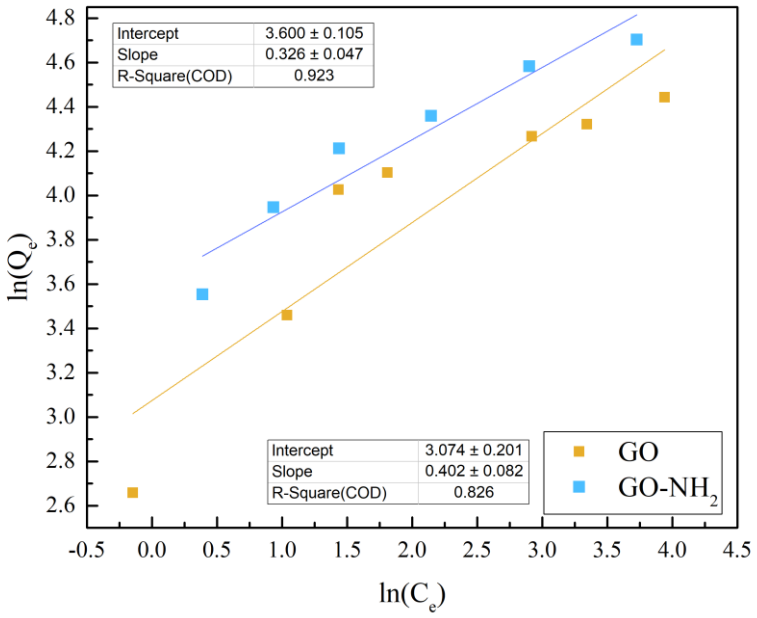

Figure 4.25 Freundlich adsorption isotherm of MO at 298 K and pH=7.8

Parameters for Langmuir and Freundlich isotherms are tabulated in **Table 4.6**. Based on the comparison of the two correlation coefficients (R^2), it can be said that the obtained isotherm data fit the Langmuir model better than the Freundlich model, which indicates that the adsorption of MO on GO and GO-NH_2 aerogel is monolayer adsorption. For GO-NH_2, R^2 was observed to be higher, which might be because the aerogel and MO's electrostatic forces were much more prominent. The maximum adsorption capacities of GO and GO-NH_2 for MO were obtained as 99.01 mg/g and 117.65 mg/g, respectively, which approach the experimental data of 85.10 mg/g and 110.27 mg/g.

Table 4.6 Adsorption isotherm parameters for MO by GO and GO-NH_2

Aerogel	Langmuir			Freundlich		
	Q_{max} (mg/g)	K_L (L/mg)	R^2	n	K_F (L/mg)	R^2
GO-NH_2	117.7	0.293	0.994	3.066	36.6	0.923
GO	99.0	0.196	0.986	3.777	32.0	0.766

CHAPTER 5

CONCLUSION

In this study, graphene oxide (GO)-based aerogels were prepared for water treatment applications.

The oil absorption performance of the prepared aerogels was examined for chloroform and sunflower oil. In order to improve the oleophilic character of GO aerogel, stearic acid (SA) was employed.

- The incorporation of stearic acid into the aerogel structure lowered the absorption capacity of the aerogels. rGO aerogels exhibited absorption capacities of 155 g/g and 118 g/g for chloroform and sunflower oil, respectively. While, rGO/SA aerogels exhibited maximum absorption capacities of 102 g/g and 77 g/g for chloroform and sunflower oil, respectively.
- However, rGO/SA aerogels exhibited high potential in reusability studies, exhibiting no apparent change in chloroform absorption capacities even after 15 cycles.
- Although it increased the shape stability of the aerogels, SA addition into GO aerogel structure inhibited the open pore formation; hence, it decreased its oil absorption performance.

The aerogels' dye adsorption performance was examined for methylene blue (MB) and methyl orange (MO). The effects of adsorption time, temperature, pH, dye charge and dye concentration on dye removal from aqueous solutions by GO-based aerogels have been studied systematically.

- Adsorption behavior results collectively suggested that GO aerogels were promising in treating MB, a cationic dye. They exhibited a maximum adsorption capacity of 588 mg/g at 298 K and environmentally relevant pH.
- Adsorption of GO aerogels toward MB was found to be slightly endothermic, pH-independent and spontaneous. GO aerogels showed excellent reusability performance for MB, maintaining its original capacity after ten adsorption cycles.
- However, GO aerogels showed less performance toward MO adsorption, exhibiting a maximum adsorption capacity of 99 mg/g.

APTES modification was employed to improve its adsorption performance toward MO, an anionic dye.

- GO-NH_2 aerogels showed a 30% higher adsorption capacity toward MO than GO aerogels, exhibiting a maximum adsorption capacity of 118 mg/g.

CHAPTER 6

OUTLOOK

Considering this study, several recommendations can be made for future work;

- rGO/SA aerogels can be tested for their mechanical and thermal stability, and their potential as phase change materials can be explored.
- Oleophilic ingredients with smaller chain size than stearic acid can be used for aerogel production.
- To increase the rate of adsorption onto GO-based aerogels, routes that can produce GO-based aerogels with smaller sizes can be explored.
- Microwave reduction can be used for the reduction of GO aerogels.
- Different amine sources can be used to increase the adsorption capacity of GO-based aerogels toward anionic dyes.

REFERENCES

1. Lingamdinne, L. P., Koduru, J. R. & Karri, R. R. A comprehensive review of applications of magnetic graphene oxide based nanocomposites for sustainable water purification. *J. Environ. Manage.* **231**, 622–634 (2019).

2. Zhang, Y. Q., Yang, X. Bin, Wang, Z. X., Long, J. & Shao, L. Designing multifunctional 3D magnetic foam for effective insoluble oil separation and rapid selective dye removal for use in wastewater remediation. *J. Mater. Chem. A* **5**, 7316–7325 (2017).

3. Barka, N., Abdennouri, M. & Makhfouk, M. E. L. Removal of Methylene Blue and Eriochrome Black T from aqueous solutions by biosorption on Scolymus hispanicus L.: Kinetics, equilibrium and thermodynamics. *J. Taiwan Inst. Chem. Eng.* **42**, 320–326 (2011).

4. Mohanty, K., Naidu, J. T., Meikap, B. C. & Biswas, M. N. Removal of crystal violet from wastewater by activated carbons prepared from rice husk. *Ind. Eng. Chem. Res.* **45**, 5165–5171 (2006).

5. Pereira, Luciana Alves, M. Environmental Impact and Remediation. in *Environmental Protection Strategies for Sustainable Development* 111–161 (2012). doi:10.1007/978-94-007-1591-2

6. Gupta, S. & Tai, N. H. Carbon materials as oil sorbents: A review on the synthesis and performance. *J. Mater. Chem. A* **4**, 1550–1565 (2016).

7. Titelman, G. I. *et al.* Characteristics and microstructure of aqueous colloidal dispersions of graphite oxide. *Carbon N. Y.* **43**, 641–649 (2005).

8. Paredes, J. I., Villar-Rodil, S., Martínez-Alonso, A. & Tascón, J. M. D. Graphene oxide dispersions in organic solvents. *Langmuir* **24**, 10560–10564 (2008).

9. Gao, W. The chemistry of graphene oxide. in *Graphene Oxide: Reduction Recipes, Spectroscopy, and Applications* (2015). doi:10.1007/978-3-319-

15500-5_3

10. Wan, S., Bi, H. & Sun, L. Graphene and carbon-based nanomaterials as highly efficient adsorbents for oils and organic solvents. *Nanotechnol. Rev.* **5**, 3–22 (2016).

11. Bi, Hengchang, Xie, Xiao, Yin, Kuibo, Zhou, Yilong, Wan, Shu, Ruoff, Rodney S., Sun, L. Highly enhanced performance of spongy graphene as an oil sorbent. *J. Mater. Chem. A* **2**, 1652–1656 (2014).

12. Geim, A. K. & Novoselov, K. S. The rise of graphene. *Nat. Mater.* (2007). doi:10.1038/nmat1849

13. Crisan, L. *et al.* Carbon-based nanomaterials as scaffolds in bone regeneration. *Part. Sci. Technol.* **0**, 1–10 (2019).

14. Meng, F.-L., Guo, Z. & Huang, X.-J. Graphene-based hybrids for chemiresistive gas sensors. *TrAC Trends Anal. Chem.* **68**, 37–47 (2015).

15. Li, C. *et al.* Three dimensional graphene networks for supercapacitor electrode materials. *New Carbon Mater.* **30**, 193–206 (2015).

16. Pedrós, J. *et al.* Polyaniline nanofiber sponge filled graphene foam as high gravimetric and volumetric capacitance electrode. *J. Power Sources* **317**, 35–42 (2016).

17. Iwan, A., Malinowski, M. & Pasciak, G. Polymer fuel cell components modified by graphene: Electrodes, electrolytes and bipolar plates. *Renew. Sustain. Energy Rev.* **49**, 954–967 (2015).

18. Seselj, N., Engelbrekt, C. & Zhang, J. Graphene-supported platinum catalysts for fuel cells. *Sci. Bull.* **60**, 864–876 (2015).

19. Sharma, V. K., McDonald, T. J., Kim, H. & Garg, V. K. Magnetic graphene–carbon nanotube iron nanocomposites as adsorbents and antibacterial agents for water purification. *Adv. Colloid Interface Sci.* **225**,

229–240 (2015).

20. Naeem, H. *et al.* Facile synthesis of graphene oxide–silver nanocomposite for decontamination of water from multiple pollutants by adsorption, catalysis and antibacterial activity. *J. Environ. Manage.* **230**, 199–211 (2019).

21. Guo, R. *et al.* Sandwiched Fe3O4/Carboxylate Graphene Oxide Nanostructures Constructed by Layer-by-Layer Assembly for Highly Efficient and Magnetically Recyclable Dye Removal. *ACS Sustain. Chem. Eng.* **6**, 1279–1288 (2018).

22. Thebo, K. H. *et al.* Highly stable graphene-oxide-based membranes with superior permeability. *Nat. Commun.* **9**, 1–8 (2018).

23. Cheng, M. meng *et al.* Synthesis of graphene oxide/polyacrylamide composite membranes for organic dyes/water separation in water purification. *J. Mater. Sci.* **54**, 252–264 (2019).

24. Sun, C., Wen, B. & Bai, B. Recent advances in nanoporous graphene membrane for gas separation and water purification. *Sci. Bull.* **60**, 1807–1823 (2015).

25. Kim, K. S. *et al.* Large-scale pattern growth of graphene films for stretchable transparent electrodes. *Nature* **457**, 706–710 (2009).

26. Eizenberg, M. & Blakely, J. M. Carbon Monolayer Phase Condensation of Ni(111). *Surf. Sci.* **82**, 228–236 (1979).

27. Mayou, D. *et al.* Electronic Confinement and. *Science (80-.).* **312**, 1191–1196 (2006).

28. Wintterlin, J. & Bocquet, M. L. Graphene on metal surfaces. *Surf. Sci.* **603**, 1841–1852 (2009).

29. Novoselov, K. S. *et al.* Electric field in atomically thin carbon films. *Science*

(80-.). **306**, 666–669 (2004).

30. Singh, R. K., Kumar, R. & Singh, D. P. Graphene oxide: Strategies for synthesis, reduction and frontier applications. *RSC Adv.* **6**, 64993–65011 (2016).

31. Dimiev, A. M. & Eigler, S. *Graphene Oxide: Fundamentals and Applications*. *Graphene Oxide: Fundamentals and Applications* (2016). doi:10.1002/9781119069447

32. Becerril, H. A. *et al.* Evaluation of solution-processed reduced graphene oxide films as transparent conductors. *ACS Nano* **2**, 463–470 (2008).

33. Chen, D., Feng, H. & Li, J. Graphene oxide: Preparation, functionalization, and electrochemical applications. *Chem. Rev.* **112**, 6027–6053 (2012).

34. Eda, G., Fanchini, G. & Chhowalla, M. Large-area ultrathin films of reduced graphene oxide as a transparent and flexible electronic material. *Nat. Nanotechnol.* (2008). doi:10.1038/nnano.2008.83

35. Loh, K. P., Bao, Q., Eda, G. & Chhowalla, M. Graphene oxide as a chemically tunable platform for optical applications. *Nat. Chem.* (2010). doi:10.1038/nchem.907

36. Liu, L., Zhang, J., Zhao, J. & Liu, F. Mechanical properties of graphene oxides. *Nanoscale* (2012). doi:10.1039/c2nr31164j

37. Brodie, B. C. XIII. On the atomic weight of graphite. *Philos. Trans. R. Soc. London* **149**, 249–259 (1859).

38. Szabó, T. *et al.* Evolution of surface functional groups in a series of progressively oxidized graphite oxides. *Chem. Mater.* **18**, 2740–2749 (2006).

39. Staudenmaier, L. Verfahren zur Darstellung der Graphitsäure. *Berichte der Dtsch. Chem. Gesellschaft* **31**, 1481–1487 (1898).

40. Hummers, W. S. & Offeman, R. E. Preparation of Graphitic Oxide. *J. Am. Chem. Soc.* **80**, 1339 (1958).

41. Kovtyukhova, N. I. Layer-by-layer assembly of ultrathin composite films from micron-sized graphite oxide sheets and polycations. *Chem. Mater.* **11**, 771–778 (1999).

42. Chen, J., Yao, B., Li, C. & Shi, G. An improved Hummers method for eco-friendly synthesis of graphene oxide. *Carbon N. Y.* **64**, 225–229 (2013).

43. Gilje, S., Han, S., Wang, M., Wang, K. L. & Kaner, R. B. A chemical route to graphene for device applications. *Nano Lett.* (2007). doi:10.1021/nl0717715

44. Marcano, D. C. *et al.* Improved synthesis of graphene oxide. *ACS Nano* **4**, 4806–4814 (2010).

45. Hofmann, U. & König, E. Untersuchungen über Graphitoxyd. *Zeitschrift für Anorg. und Allg. Chemie* **234**, 311–336 (1937).

46. Sun, L. & Fugetsu, B. Mass production of graphene oxide from expanded graphite. *Mater. Lett.* **109**, 207–210 (2013).

47. Peng, L. *et al.* An iron-based green approach to 1-h production of single-layer graphene oxide. *Nat. Commun.* **6**, (2015).

48. Kistler, S. S., Fischer, E. A. & Freeman, I. R. Sorption and Surface Area in Silica Aerogel. *J. Am. Chem. Soc.* **65**, 1909–1919 (1943).

49. Ulker, Z. & Erkey, C. An emerging platform for drug delivery: Aerogel based systems. *Journal of Controlled Release* (2014). doi:10.1016/j.jconrel.2013.12.033

50. Pircher, N. *et al.* Preparation and Reinforcement of Dual-Porous Biocompatible Cellulose Scaffolds for Tissue Engineering. *Macromol. Mater. Eng.* **300**, 911–924 (2015).

51. Lorant, R. Cosmetic composition comprising silica aerogel particles, a gemini surfactant and a solid fatty substance. **1**, 1–19 (2014).

52. Karout, A., Buisson, P., Perrard, A. & Pierre, A. C. Shaping and mechanical reinforcement of silica aerogel biocatalysts with ceramic fiber felts. *J. Sol-Gel Sci. Technol.* (2005). doi:10.1007/s10971-005-5288-z

53. Gong, J. *et al.* Sustainable conversion of mixed plastics into porous carbon nanosheets with high performances in uptake of carbon dioxide and storage of hydrogen. *ACS Sustain. Chem. Eng.* (2014). doi:10.1021/sc500603h

54. Fickler, S., Milow, B., Ratke, L., Schnellenbach-Held, M. & Welsch, T. Development of high performance aerogel concrete. in *Energy Procedia* (2015). doi:10.1016/j.egypro.2015.11.684

55. Shi, J., Lu, L., Guo, W., Sun, Y. & Cao, Y. An environment-friendly thermal insulation material from cellulose and plasma modification. *J. Appl. Polym. Sci.* (2013). doi:10.1002/app.39615

56. Shi, J., Lu, L., Guo, W., Zhang, J. & Cao, Y. Heat insulation performance, mechanics and hydrophobic modification of cellulose-SiO2 composite aerogels. *Carbohydr. Polym.* (2013). doi:10.1016/j.carbpol.2013.05.082

57. Du, A., Zhou, B., Zhang, Z. & Shen, J. A special material or a new state of matter: A review and reconsideration of the aerogel. *Materials (Basel).* **6**, 941–968 (2013).

58. Zuo, L. *et al.* Polymer/Carbon-Based Hybrid Aerogels: Preparation, Properties and Applications. *Materials* **8**, 6806–6848 (2015).

59. Maleki, H. Recent advances in aerogels for environmental remediation applications: A review. *Chem. Eng. J.* **300**, 98–118 (2016).

60. Baumann, T. F., Kucheyev, S. O., Gash, A. E. & Satcher, J. H. Facile synthesis of a crystalline, high-surface-area SnO2 aerogel. *Adv. Mater.* (2005). doi:10.1002/adma.200500074

61. Smirnova, I. & Gurikov, P. Aerogels in Chemical Engineering: Strategies Toward Tailor-Made Aerogels. *Annu. Rev. Chem. Biomol. Eng.* **8**, 307–334 (2017).

62. Tamon, H., Ishizaka, H., Mikami, M. & Okazaki, M. Porous structure of organic and carbon aerogels synthesized by sol-gel polycondensation of resorcinol with formaldehyde. *Carbon N. Y.* (1997). doi:10.1016/S0008-6223(97)00024-9

63. Huang, J., Liu, H., Chen, S. & Ding, C. Graphene aerogel prepared through double hydrothermal reduction as high-performance oil adsorbent. *Mater. Sci. Eng. B Solid-State Mater. Adv. Technol.* **226**, 141–150 (2017).

64. Mohanan, J. L., Arachchige, I. U. & Brock, S. L. Porous semiconductor chalcogenide aerogels. *Science* (2005). doi:10.1126/science.1106525

65. Chen, K. *et al.* Low temperature pseudomorphic synthesis of nanocrystalline carbide aerogels for electrocatalysis. *J. Mater. Chem. A* **3**, 11745–11749 (2015).

66. Davis, M., Hikal, W. M., Gümeci, C. & Hope-Weeks, L. J. Aerogel nanocomposites of ZnO-SnO 2 as efficient photocatalysts for the degradation of rhodamine B. *Catal. Sci. Technol.* (2012). doi:10.1039/c2cy20020a

67. Jones, S. M. A method for producing gradient density aerogel. *J. Sol-Gel Sci. Technol.* (2007). doi:10.1007/s10971-007-1618-7

68. Tang, J. *et al.* Fabrication and characterization of composition-gradient CuO/SiO 2 composite aerogel. *J. Sol-Gel Sci. Technol.* (2013). doi:10.1007/s10971-013-3140-4

69. Doğan, Ö. Development of Graphene Oxide Based Aerogels. (Middle East Technical University, 2017).

70. Aegerter, Michel A., Leventis, Nicholas, Koebel, M. M. *Aerogels*

Handbook. *Aerogels Handbook* (2011). doi:10.1007/978-1-4419-7589-8

71. Shen, Y., Fang, Q. & Chen, B. Environmental applications of three-dimensional graphene-based macrostructures: Adsorption, transformation, and detection. *Environ. Sci. Technol.* **49**, 67–84 (2015).

72. Sha, J. *et al.* Preparation of three-dimensional graphene foams using powder metallurgy templates. *ACS Nano* **10**, 1411–1416 (2016).

73. Choi, B. G. *et al.* 3D heterostructured architectures of Co3O4 nanoparticles deposited on porous graphene surfaces for high performance of lithium ion batteries. *Nanoscale* **4**, 5924–5930 (2012).

74. Zhang, Q. *et al.* 3D Printing of Graphene Aerogels. *Small* **12**, 1702–1708 (2016).

75. Chakravarty, D. *et al.* 3D Porous Graphene by Low-Temperature Plasma Welding for Bone Implants. *Adv. Mater.* **28**, 8959–8967 (2016).

76. Rethinasabapathy, M., Kang, S. M., Jang, S. C. & Huh, Y. S. Three-dimensional porous graphene materials for environmental applications. *Carbon Lett.* **22**, 1–13 (2017).

77. Nardecchia, S., Carriazo, D., Ferrer, M. L., Gutiérrez, M. C. & Monte, F. Del. Three dimensional macroporous architectures and aerogels built of carbon nanotubes and/or graphene: Synthesis and applications. *Chem. Soc. Rev.* **42**, 794–830 (2013).

78. Bai, H., Li, C., Wang, X. & Shi, G. On the gelation of graphene oxide. *J. Phys. Chem. C* (2011). doi:10.1021/jp1120299

79. Gorgolis, G. & Galiotis, C. Graphene aerogels: A review. *2D Mater.* **4**, (2017).

80. Xu, Y., Sheng, K., Li, C. & Shi, G. Self-Assembled Graphene Hydrogel via a One-Step Hydrothermal Process. *ACS Nano* **4**, 4324–4330 (2010).

81. Banda, H. *et al.* One-step synthesis of highly reduced graphene hydrogels for high power supercapacitor applications. *J. Power Sources* (2017). doi:10.1016/j.jpowsour.2017.06.033

82. Zhang, X. *et al.* Mechanically strong and highly conductive graphene aerogel and its use as electrodes for electrochemical power sources. *J. Mater. Chem.* (2011). doi:10.1039/c1jm10239g

83. Jiang, X., Ma, Y., Li, J., Fan, Q. & Huang, W. Self-Assembly of Reduced Graphene Oxide into Three-Dimensional Architecture by Divalent Ion Linkage. *J. Phys. Chem. C* (2010). doi:10.1021/jp108081g

84. Gao, H., Sun, Y., Zhou, J., Xu, R. & Duan, H. Mussel-inspired synthesis of polydopamine-functionalized graphene hydrogel as reusable adsorbents for water purification. *ACS Appl. Mater. Interfaces* (2013). doi:10.1021/am302500v

85. Fang, Q., Shen, Y. & Chen, B. Synthesis, decoration and properties of three-dimensional graphene-based macrostructures: A review. *Chem. Eng. J.* **264**, 753–771 (2015).

86. Ye, S., Feng, J. & Wu, P. Highly elastic graphene oxide-epoxy composite aerogels via simple freeze-drying and subsequent routine curing. *J. Mater. Chem. A* (2013). doi:10.1039/c2ta01142e

87. Estevez, L., Kelarakis, A., Gong, Q., Daas, E. H. & Giannelis, E. P. Multifunctional graphene/platinum/nafion hybrids via ice templating. *J. Am. Chem. Soc.* (2011). doi:10.1021/ja200244s

88. Zhang, L. & Shi, G. Preparation of highly conductive graphene hydrogels for fabricating supercapacitors with high rate capability. *J. Phys. Chem. C* (2011). doi:10.1021/jp204036a

89. Lin, Y., Ehlert, G. J., Bukowsky, C. & Sodano, H. A. Superhydrophobic functionalized graphene aerogels. *ACS Appl. Mater. Interfaces* (2011).

doi:10.1021/am200527j

90. Khan, M. & Lo, I. M. C. Removal of ionizable aromatic pollutants from contaminated water using nano γ-Fe 2 O 3 based magnetic cationic hydrogel: Sorptive performance, magnetic separation and reusability. *J. Hazard. Mater.* (2017). doi:10.1016/j.jhazmat.2016.01.051

91. Sinha, V. & Chakma, S. Advances in the preparation of hydrogel for wastewater treatment: A concise review. *J. Environ. Chem. Eng.* **7**, 103295 (2019).

92. Yousefi, N., Lu, X., Elimelech, M. & Tufenkji, N. Environmental performance of graphene-based 3D macrostructures. *Nat. Nanotechnol.* **14**, 107–119 (2019).

93. Artioli, Y. Adsorption. in *Encyclopedia of Ecology, Five-Volume Set* 60 (2008). doi:10.1016/B978-008045405-4.00252-4

94. Ruthven, D. M. Fundamentals of adsorption equilibrium and kinetics in microporous solids. *Molecular Sieves - Science and Technology* 4 (2008). doi:10.1007/3829_007

95. Limousin, G. *et al.* Sorption isotherms: A review on physical bases, modeling and measurement. *Applied Geochemistry* (2007). doi:10.1016/j.apgeochem.2006.09.010

96. Liu, L., Luo, X. B., Ding, L. & Luo, S. L. Application of Nanotechnology in the Removal of Heavy Metal From Water. in *Nanomaterials for the Removal of Pollutants and Resource Reutilization* 89 (2018). doi:10.1016/B978-0-12-814837-2.00004-4

97. Khurana, I., Saxena, A., Bharti, Khurana, J. M. & Rai, P. K. Removal of Dyes Using Graphene-Based Composites: a Review. *Water. Air. Soil Pollut.* **228**, (2017).

98. Kuo, S. & Lotse, E. G. Kinetics of phosphate adsorption and desorption by

hematite and gibbsite. *Soil Sci.* (1973). doi:10.1097/00010694-197312000-00002

99. Weber, W. Kinetics of Adsorption on Carbon from Solution. *J. Sanit. Eng. Div.* (1963).

100. Yan, H. *et al.* Effects of the oxidation degree of graphene oxide on the adsorption of methylene blue. *J. Hazard. Mater.* **268**, 191–198 (2014).

101. Xiao, J. *et al.* Environmentally friendly reduced graphene oxide as a broad-spectrum adsorbent for anionic and cationic dyes: Via π-π Interactions. *J. Mater. Chem. A* **4**, 12126–12135 (2016).

102. Hu, L. *et al.* Fabrication of magnetic water-soluble hyperbranched polyol functionalized graphene oxide for high-efficiency water remediation. *Sci. Rep.* **6**, 1–13 (2016).

103. Mu, B., Tang, J., Zhang, L. & Wang, A. Facile fabrication of superparamagnetic graphene/polyaniline/Fe3O4 nanocomposites for fast magnetic separation and efficient removal of dye. *Sci. Rep.* **7**, 1–12 (2017).

104. Du, Q. *et al.* A graphene-melamine-sponge for efficient and recyclable dye adsorption. *RSC Adv.* **6**, 54589–54596 (2016).

105. Zhao, L. *et al.* Preparation and application of carboxylated graphene oxide sponge in dye removal. *Int. J. Environ. Res. Public Health* **14**, (2017).

106. Sarkar, A. K., Bediako, J. K., Choi, J. W. & Yun, Y. S. Functionalized magnetic biopolymeric graphene oxide with outstanding performance in water purification. *NPG Asia Mater.* **11**, (2019).

107. Dai, H., Huang, Y. & Huang, H. Eco-friendly polyvinyl alcohol/carboxymethyl cellulose hydrogels reinforced with graphene oxide and bentonite for enhanced adsorption of methylene blue. *Carbohydr. Polym.* (2018). doi:10.1016/j.carbpol.2017.12.073

108. Chen, Y., Chen, L., Bai, H. & Li, L. Graphene oxide-chitosan composite hydrogels as broad-spectrum adsorbents for water purification. *J. Mater. Chem. A* **1**, 1992–2001 (2013).

109. Sui, Z. Y., Cui, Y., Zhu, J. H. & Han, B. H. Preparation of Three-dimensional graphene oxide-polyethylenimine porous materials as dye and gas adsorbents. *ACS Appl. Mater. Interfaces* (2013). doi:10.1021/am402661t

110. Zambare, R., Song, X., Bhuvana, S., Antony Prince, J. S. & Nemade, P. Ultrafast Dye Removal Using Ionic Liquid-Graphene Oxide Sponge. *ACS Sustain. Chem. Eng.* **5**, 6026–6035 (2017).

111. Huang, T. *et al.* Chitosan-Cross-Linked Graphene Oxide/Carboxymethyl Cellulose Aerogel Globules with High Structure Stability in Liquid and Extremely High Adsorption Ability. *ACS Sustain. Chem. Eng.* **7**, 8775–8788 (2019).

112. Ma, T., Chang, P. R., Zheng, P., Zhao, F. & Ma, X. Fabrication of ultra-light graphene-based gels and their adsorption of methylene blue. *Chem. Eng. J.* **240**, 595–600 (2014).

113. Chongyang Qi, Lianqin Zhao, Yan Lin, D. W. Graphene oxide chitosan sponge as a novel filtering material for theremoval of dye from water. *J. Colloid Interface Sci.* **517**, 18–27 (2018).

114. Yang, Y., Song, S. & Zhao, Z. Graphene oxide (GO)/polyacrylamide (PAM) composite hydrogels as efficient cationic dye adsorbents. *Colloids Surfaces A Physicochem. Eng. Asp.* **513**, 315–324 (2017).

115. Yu, R. *et al.* Graphene Oxide/Chitosan Aerogel Microspheres with Honeycomb-Cobweb and Radially Oriented Microchannel Structures for Broad-Spectrum and Rapid Adsorption of Water Contaminants. *ACS Appl. Mater. Interfaces* **9**, 21809–21819 (2017).

116. Peng, S., Zhang, D., Huang, H., Jin, Z. & Peng, X. Ionic polyacrylamide

hydrogel improved by graphene oxide for efficient adsorption of methylene blue. *Res. Chem. Intermed.* **45**, 1545–1563 (2019).

117. Liu, C. *et al.* Partly reduced graphene oxide aerogels induced by proanthocyanidins for efficient dye removal. *Bioresour. Technol.* **282**, 148–155 (2019).

118. Wang, S. *et al.* Preparation and characterization of graphene oxide/silk fibroin hybrid aerogel for dye and heavy metal adsorption. *Compos. Part B Eng.* **163**, 716–722 (2019).

119. Xu, J., Xu, D., Zhu, B., Cheng, B. & Jiang, C. Adsorptive removal of an anionic dye Congo red by flower-like hierarchical magnesium oxide (MgO)-graphene oxide composite microspheres. *Appl. Surf. Sci.* **435**, 1136–1142 (2018).

120. Zhou, J. *et al.* Graphene oxide-based polyethersulfone core-shell particles for dye uptake. *RSC Adv.* **6**, 102389–102397 (2016).

121. Zhou, S. *et al.* One-pot synthesis of robust superhydrophobic, functionalized graphene/polyurethane sponge for effective continuous oil-water separation. *Chem. Eng. J.* **302**, 155–162 (2016).

122. Bi, H. *et al.* Spongy graphene as a highly efficient and recyclable sorbent for oils and organic solvents. *Adv. Funct. Mater.* (2012). doi:10.1002/adfm.201200888

123. Chen, C. *et al.* Compressive, ultralight and fire-resistant lignin-modified graphene aerogels as recyclable absorbents for oil and organic solvents. *Chem. Eng. J.* **350**, 173–180 (2018).

124. Li, H., Liu, L. & Yang, F. Covalent assembly of 3D graphene/polypyrrole foams for oil spill cleanup. *J. Mater. Chem. A* (2013). doi:10.1039/c3ta00166k

125. Yang, S. *et al.* Vapor-Liquid Deposition Strategy to Prepare

Superhydrophobic and Superoleophilic Graphene Aerogel for Oil-Water Separation. *ACS Appl. Nano Mater.* (2018). doi:10.1021/acsanm.7b00027

126. Kim, F. *et al.* Self-propagating domino-like reactions in oxidized graphite. *Adv. Funct. Mater.* (2010). doi:10.1002/adfm.201000736

127. Gupta, V. K., Singh, P. & Rahman, N. Adsorption behavior of Hg(II), Pb(II), and Cd(II) from aqueous solution on Duolite C-433: A synthetic resin. *J. Colloid Interface Sci.* (2004). doi:10.1016/j.jcis.2004.02.046

128. Wahab, H. *et al.* Signatures of different carbon bonds in graphene oxide from soft x-ray reflectometry. *X-Ray Spectrometry* **44**, 468–473 (2015).

129. Gao, W. Graphite Oxide. in *Springer Handbook of Nanomaterials* 571–603 (2013). doi:10.1007/978-3-642-20595-8

130. Kabel, K. I., Farag, A. A., Elnaggar, E. M. & Al-Gamal, A. G. Improvement of graphene oxide characteristics depending on base washing. *J. Superhard Mater.* **37**, 327–334 (2015).

131. Jiang, B. *et al.* In situ growth of TiO2 in interlayers of expanded graphite for the fabrication of TiO2-graphene with enhanced photocatalytic activity. *Chem. - A Eur. J.* (2011). doi:10.1002/chem.201100250

132. Chen, Z., Cao, L., Shan, F. & Fang, G. Preparation and characteristics of microencapsulated stearic acid as composite thermal energy storage material in buildings. *Energy Build.* **62**, 469–474 (2013).

133. Pourhashem, S., Vaezi, M. R., Rashidi, A. & Bagherzadeh, M. R. Distinctive roles of silane coupling agents on the corrosion inhibition performance of graphene oxide in epoxy coatings. *Prog. Org. Coatings* **111**, 47–56 (2017).

134. Sun, W. *et al.* Inhibiting the corrosion-promotion activity of graphene. *Chem. Mater.* **27**, 2367–2373 (2015).

135. Yagub, M. T., Sen, T. K., Afroze, S. & Ang, H. M. Dye and its removal

from aqueous solution by adsorption: A review. *Advances in Colloid and Interface Science* (2014). doi:10.1016/j.cis.2014.04.002

136. Huang, T. *et al.* Efficient removal of methylene blue from aqueous solutions using magnetic graphene oxide modified zeolite. *J. Colloid Interface Sci.* **543**, 43–51 (2019).

APPENDICES

A. TGA Thermograms

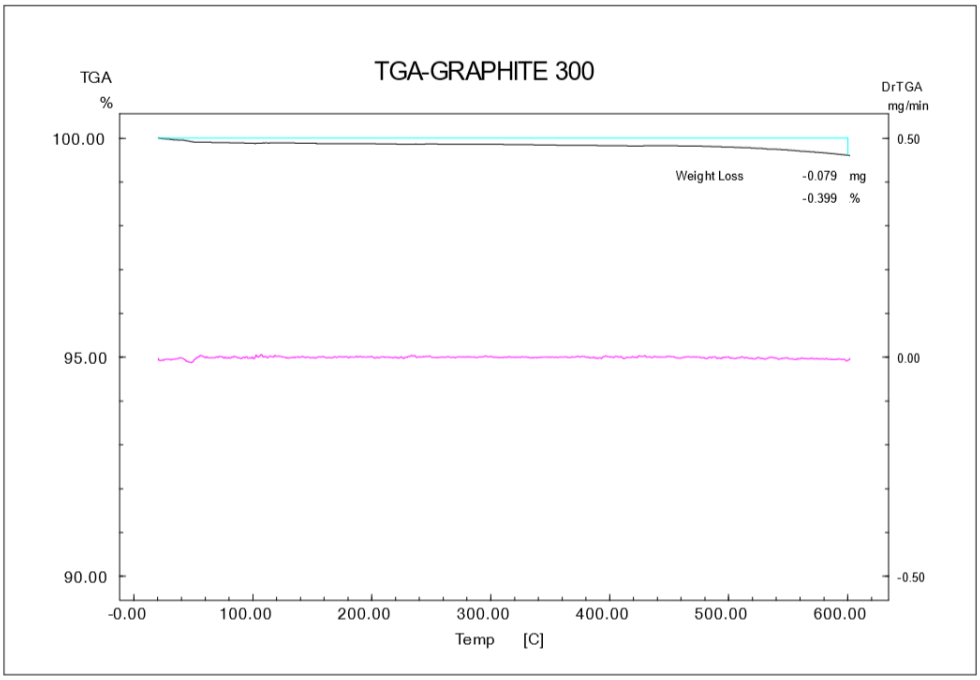

Figure A. 1 TGA thermogram of graphite

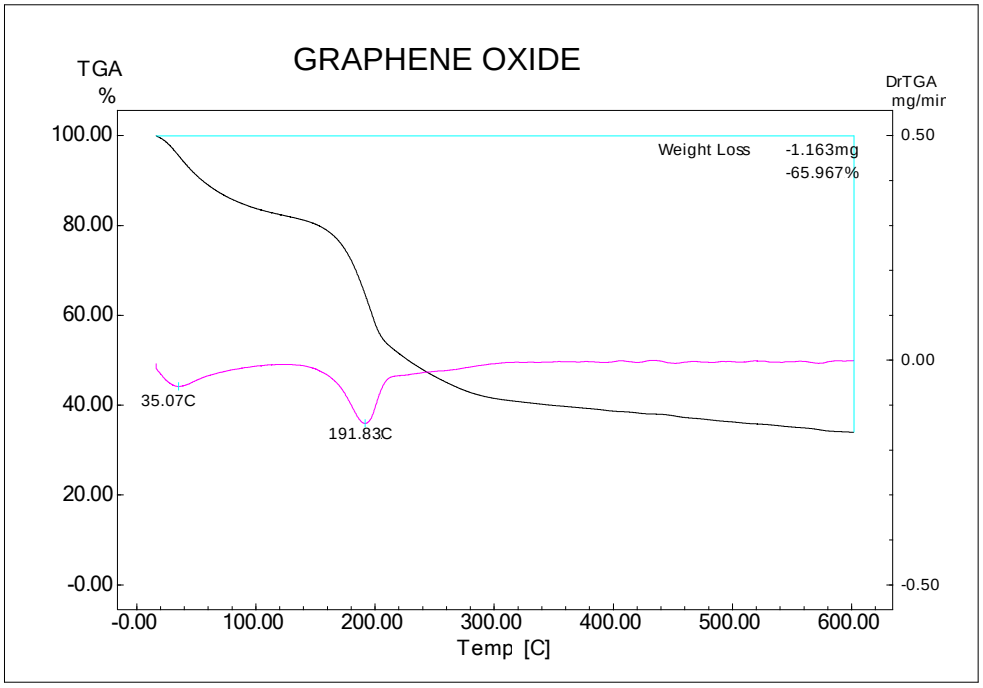

Figure A. 2 TGA thermogram of GO

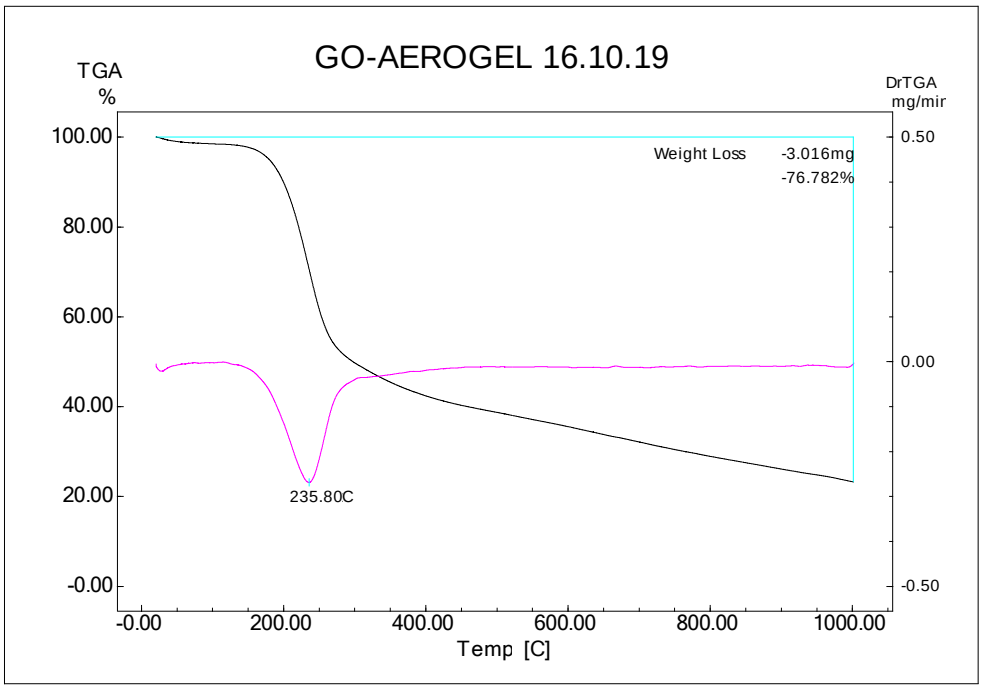

Figure A. 3 TGA thermogram of rGO aerogel

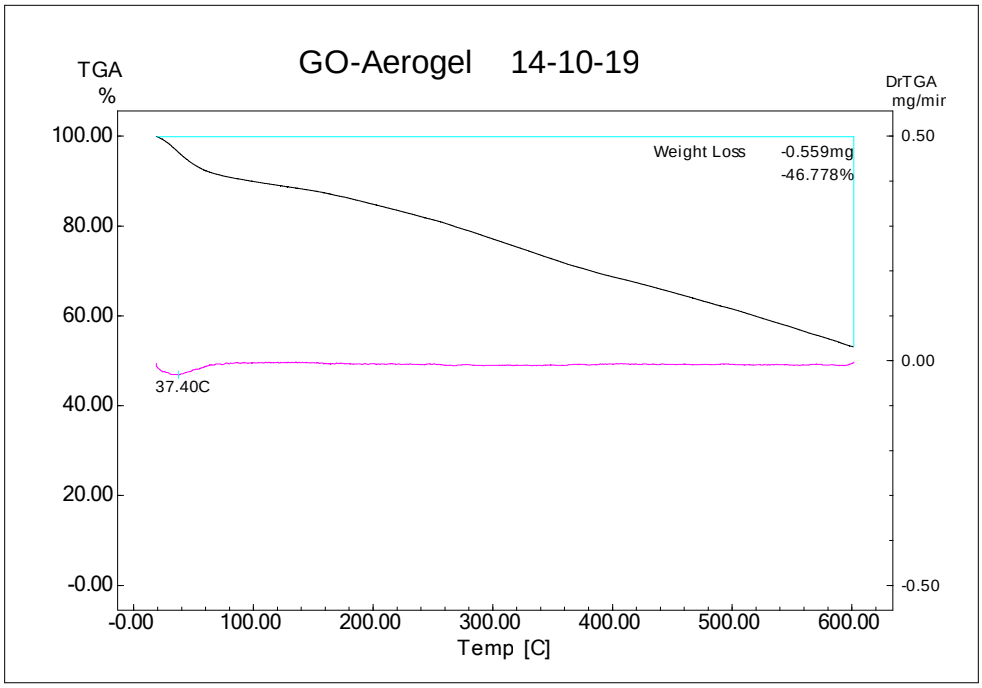

Figure A. 4. TGA thermogram of rGO/SA aerogel

B. Dye Adsorption Experiment Results

Table B. 1 Kinetic study experimental results for MB adsorption

Adsorbate/Adsorbant	MB/GOA	Adsorbate/Adsorbant	MO/GOA
t (h)	**C_t (ppm)**	**t (h)**	**C_t (ppm)**
2	96.1414	2	97.8313
3	95.4185	3	96.4224
6	90.4480	6	93.4137
12	78.2102	12	90.0518
16	67.1647	16	80.2134
24	47.2341	24	72.9317
30	43.5063	30	62.2134
36	26.5157	36	56.8675
48	20.9909	48	56.3154
60	16.1858	60	56.3320
72	13.9951	72	51.5127
84	9.7108	96	57.1213
96	5.2408		
108	5.4845		

Table B. 2 Isotherm study experimental results for MO adsorption

Adsorbate/Adsorbant	Temperature (K)	Adsorbate/Adsorbant	Temperature (K)
MO/GOA	298	MO/AGO	298
C_0 (ppm)	**C_e (ppm)**	**C_0 (ppm)**	**C_e (ppm)**
10	0.8630	10	0
20	2.8259	20	1.4742
30	4.1963	30	2.5467
40	6.1074	40	4.2147
50	18.5259	50	8.5548
70	28.3164	70	18.1765
100	51.5127	100	41.5548

Table B. 3 Isotherm study experimental results for MB adsorption

Adsorbate/ Adsorbant	Temperature (K)	Adsorbate/ Adsorbant	Temperature (K)	Adsorbate/ Adsorbant	Temperature (K)
MB/GOA	298	MB/GOA	311	MB/GOA	323
C_0 (ppm)	**C_e (ppm)**	**C_0 (ppm)**	**C_e (ppm)**	**C_0 (ppm)**	**C_e (ppm)**
40	0.2511	100	0.3061	100	0
50	2.6026	200	9.4150	200	4.6007
100	5.7013	250	14.2591	250	5.7764
150	10.6598	300	18.5825	300	8.5322
200	24.6131	325	22.5182	350	10.8218
250	35.8692	350	30.1015	400	15.7937
280	40.5432	400	43.9026	450	24.2970
300	49.4994				
320	55.5461				
350	72.5492				
400	95.4108				

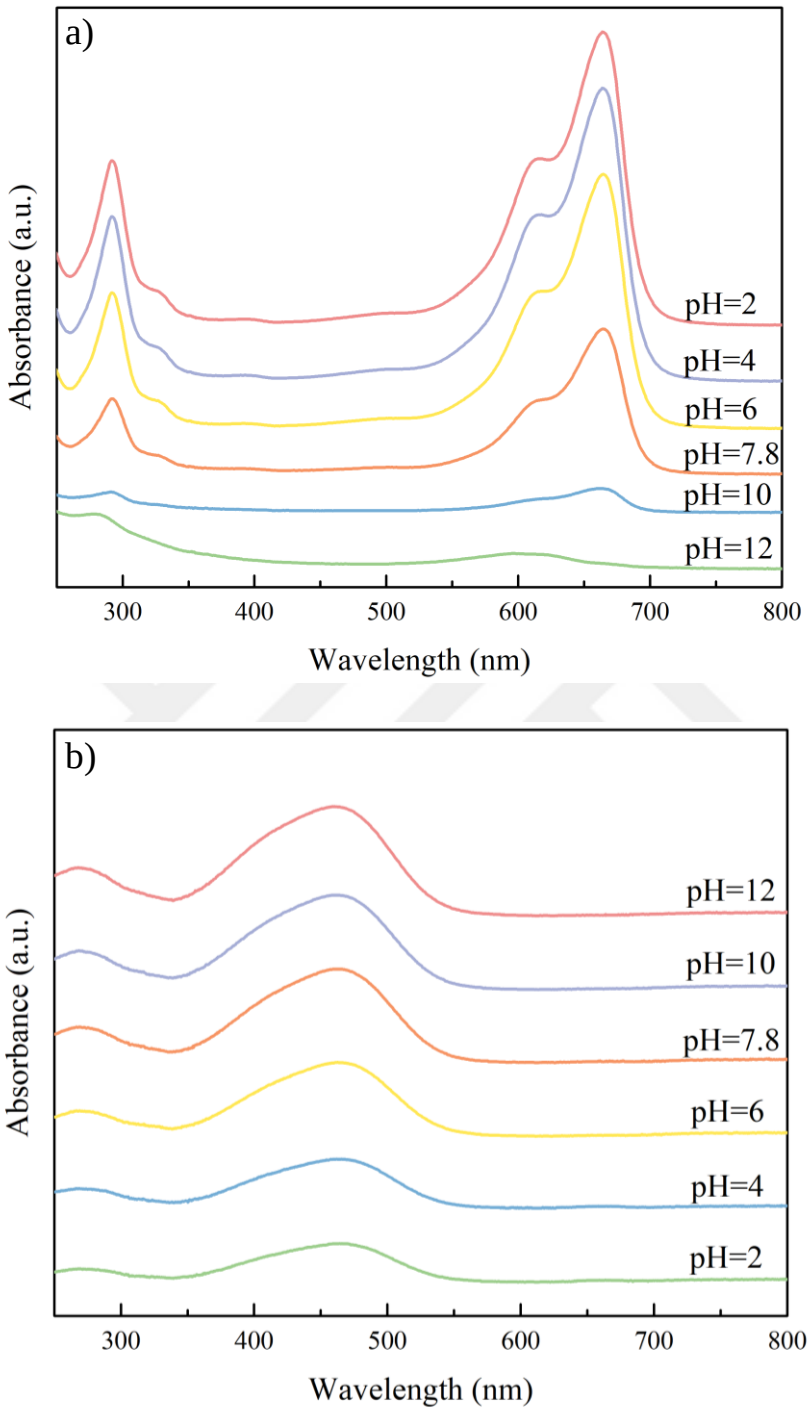

Figure B. 1 UV-Vis spectra of the MB (a) and MO (b) solutions after being adsorbed by GO aerogel

C. Standard Calibration Curve

Calibration curves for MB and MO were obtained for dye concentrations between 1 and 10 ppm. Calibration curves are given in **Figure C. 1**. Fitting results of the plots are given in **Table C. 1**.

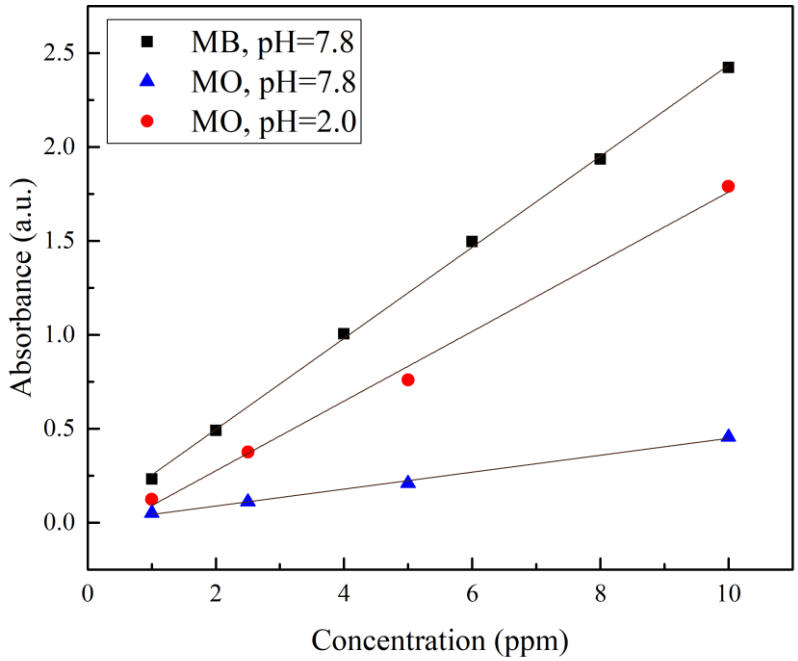

Figure C. 1 Calibration curve for MB and MO

Table C. 1 Calibration curve fitting parameters for MB and MO

	Slope	Intercept	R^2
MB, pH=7.8	0.2424	0.0118	0.9993
MO, pH=7.8	0.0451	-0.0010	0.9968
MO, pH=2.0	0.1854	-0.0942	0.9955

D. Preliminary Absorption Experiments

Optimization studies were conducted to investigate the effect of GO concentration, the temperature during gel formation and thermal reduction of the prepared aerogels at 150 °C on their absorption capacities. Results were given in **Figure D. 1**.

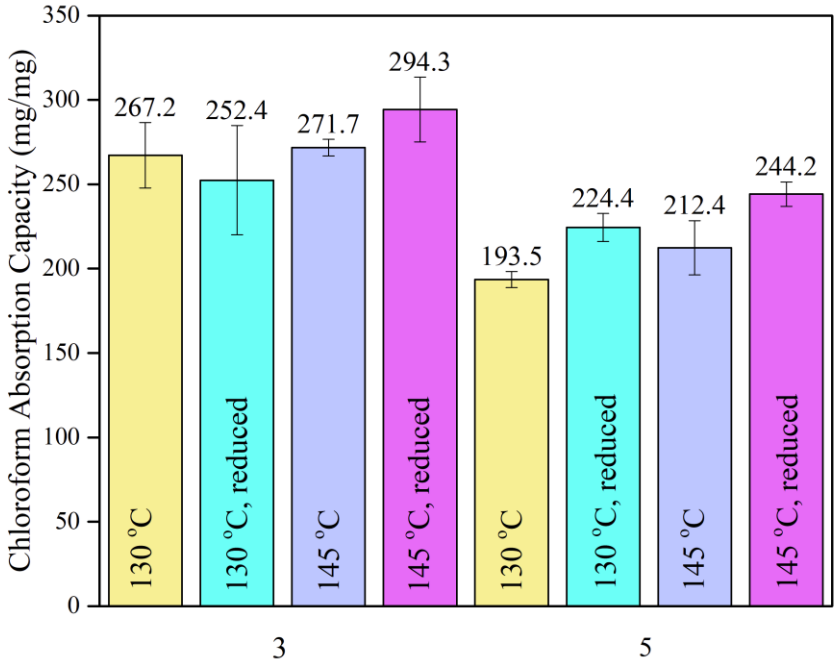

Figure D. 1 Effect of gel formation temperature and thermal reduction on chloroform absorption capacities of GO-based aerogels